Passive Tracking and System Interfaces for Interventional MRI

Inauguraldissertation

zur Erlangung der Würde eines Doktors der Philosophie
vorgelegt der
Philosophisch-Naturwissenschaftlichen Fakultät
der Universität Basel

von
Sunil Patil
aus Mumbai, Indien

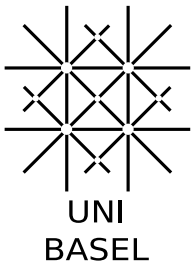

Basel, 2009

Genehmigt von der Philosophisch-Naturwissenschaftlichen Fakultät

auf Antrag von:

Prof. Dr. Klaus Scheffler
Referent

Prof. Dr. Mark Ladd
Korreferent

Basel, den 23.06.2009

Prof. Dr. Eberhard Parlow
Dekan

Abstract

One of the major pre-requisite of MR-guided interventions is the visualization and localization of interventional devices relative to the vascular system and surrounding tissues. A number of approaches have been proposed for device visualization in an MR environment that are categorized into active, passive and semi-active techniques. In spite of considerable growth of these techniques, there is a scope to investigate and develop new pulse sequences and system interfaces for these techniques to make clinically feasible. In this thesis fast and novel passive tracking approaches to efficiently visualize and track the interventional guidewire tip using positive contrast are provided and highly miniaturized active micro-coils with built-in pre-amplifier are introduced.

In passive tracking techniques, the paramagnetic markers are utilized having susceptibility differences with respect to surrounding water protons. When this marker is placed in a uniform main magnetic field B_0, it cause significant field inhomogeneities leading to dual effect of local frequency shifts and local gradient induction in marker's immediate surrounding.

The first method introduced in this thesis exploit the local frequency shifts induced by paramagnetic marker to create positive contrast. The binomial spatial-spectral (SPSP) excitation pulse that selectively excites the spectral component of the off-resonant tissues in the close proximity of the marker material and within the selected spatial region is incorporated into a temporally efficient steady state free precession (SSFP)-echo sequence. In this work, the principle of off-resonance excitation of tissues using SPSP pulse is explained theoretically. The in-vitro experiments demonstrate the proper localization and feasibility of paramagnetic marker detection mounted on the interventional guidewire tip. The analysis of the signal and localization characteristics of the SPSP pulse is done theoretically and verified experimentally.

The next novel positive contrast method for passive localization and visualization of paramagnetic susceptibility markers is based on an echo-dephased SSFP sequence. Gradients dephase any signal by $\pm\pi$ at the centered echo-time (TE=TR/2) and induce a total dephasing of $\pm 2\pi$ per pixel within TR. This ensures that background tissues do not contribute to signal formation and thus appear dark. However, within the close vicinity of the

paramagnetic marker, local gradient fields compensate for the intrinsic dephasing to form an echo. Conceptual issues of gradient compensation and its visualization characteristics are analyzed. The flow phantom experiments concluded that reliable tracking of the interventional guidewire is feasible using echo-dephased SSFP. Finally utilization of echo-dephased SSFP for positive contrast visualization of SPIO-labeled islet cells is demonstrated both in vitro and in vivo.

A novel and fast approach for passive real-time tracking of interventional devices using paramagnetic markers termed Projection Reconstruction Imaging with Echo-Dephasing (PRIDE) is also presented in this thesis. PRIDE is based on the acquisition of echo-dephased projections along all three physical axes. Dephasing is preferably set to 4π within each projection ensuring that background tissues do not contribute to signal formation and thus appear heavily suppressed. However, within the close vicinity of the paramagnetic marker, local gradient fields compensate for the intrinsic dephasing to form an echo. Successful localization of the paramagnetic marker with PRIDE is demonstrated in-vitro and in-vivo in the presence of different types of off-resonance (air/tissue interfaces, main magnetic field inhomogeneities, etc). In order to utilize the PRIDE sequence for vascular interventional applications, it was interleaved with balanced steady-state free precession (bSSFP) to provide positional updates to the imaged slice using a dedicated real-time feedback link. Active slice positioning with PRIDE is demonstrated in vitro requiring approximately 20 ms for the positional update to the imaging sequence comparable to existing active tracking methods.

The active tracking method of device visualization utilizes locally sensitive transmit/receive coils for localization and visualization of its tip. The localization of the coil is achieved in few milliseconds through acquisition of one dimensional (1D) projections along all three spatial directions (X, Y and Z). However, the dimensions of these coils are bulky in nature thereby increasing the size of normal interventional devices (for e.g. catheter). In order to overcome this disadvantage in the last part of this thesis, highly miniaturized micro coils with built-in amplifier are introduced and experimentally tested.

Acknowledgment

During the persuit of my PhD degree, I have been graciously affected by so many people in my life. I would like to take this opportunity to express my deepest gratitude towards them.

The first person I would like to thank is my research supervisor Prof. Klaus Scheffler for giving me an opportunity to pursue doctoral work under his guidance. I also would like to thank him for giving me means, tools and freedom to pursue my research directions. He showed utmost desire to establish collaborations to forward the research work. Its been steep but smooth learning curve to work under his able leadership.

Its been a sheer joy and a privilege to share office with Oliver Bieri and see him working so closely. I definitely look up to him as one of the finest, dedicated and intelligent researcher I have ever come across. It was from him that I learned so much about physical principles of SSFP.

Many many thanks to my dearest friend, Francesco Santini. We started the journey of PhD on the same day and bonded well since then. We share a great camaraderie not only at work place but also outside of the lab. My gratitude extends to his wonderful family as well, who always made me feel at home whenever I visited them.

I owe a great deal of gratitude to Markus Klarhöfer. His altruistic nature coupled with kindness means that he is been always there for me to help. He is THE MRI guy with keenness to learn all aspects MRI from anyone who might know. Its been great to work with him.

Oliver Weber has been good friend, office-mate and a mentor for me. He is one of the kindest and gentlest person I have come across. Over the years, I have started admiring his professional style of working and his vast knowledge in the field. He is been great source of advice and encouragement. Oliver, thanks for everything.

I express my kind gratitude to Permi Jhooti for helping me during my initial stages of work and offering me valuable tips throughout my work.

I also acknowledge the support of Christian Boller for helping me to settle in Switzerland, for offering many tips on sequence programming as well as basics of MR-physics.

The work on interventional project always requires skilled technicians help. Special thanks to Tanja Haas for her help with setting up the flow

phantom, handling different devices, offering tips on setting up protocols etc.

A lively and charming environment in our group has been wonderfully set, thanks to Claudia's warm nature, quiet yet smiling Monika, cool and calm Christoph, Henk-Joost with his side-splitting remarks. Thanks to all of you for having such a wonderful time together.

I would also like to thank my academic collaborators outside of my group. I thank Harald H. Quick from Essen for helping me to try out my sequences on a pig model. My special thanks also go to Michael Bock and Reiner Umathum from Heidelberg for helping me with pig studies, having fruitful discussions ranging from sequences to coils. I would also like to acknowledge Jens Anders and Giovanni Boero from Lausanne for helping me with coil work. Special thanks also to Daniel Jirak from Institute of Clinical and Experimental Medicine in Prague. His expertise in islet labeling coupled with his generous and warm nature has been immensely helpful to get the some of the results presented in this thesis.

Being landed in a country like Switzerland, it was natural to look for Indian friends to feel at home. Abiraj, to whom I consider as my elder brother aptly filled that place. I would also like to thank Prasad, Navratna and all members of Humlog; Basel Indian community for giving so many good memories to cherish through organization of events.

Although personally the journey of PhD was started three and half years ago, I had started sowing the seeds right after my Bachelors degree. Undoubtedly that was the toughest experience I had in my life so far. My heartfelt thanks to a friend and mentor Shrikant Masurekar, who supported and encouraged me during my initial struggling days. My close and dear friends who are been always there with me through thick and thin are: Amit, Nikhil, Abhishek, Hrishikesh, Manish, Smita, Mrudula and Manohar. Your love and unwavering support means a lot to me.

I would not have been successful in this endeavor without the blessings of my parents. The amount of affection that my mom, dad and my young sisters; Anandi and Sadhana is been showering on me is immeasurable. Their rock solid support is been largely responsible for strengthening my ambitions. I dedicate this thesis to them.

Sunil Patil

Publications Arising From This Thesis

Papers in international Journals

- **S. Patil**, O.Bieri, P. Jhooti, K. Scheffler, "An Automatic Slice Positioning for Passive Real-Time Tracking of Interventional Devices Using Projection Reconstruction Imaging with Echo-Dephasing (PRIDE)", Magn. Reson. in Med., In Press, 2009.
- **S. Patil**, O. Bieri, and K. Scheffler, "Echo-dephased steady state free precession", Magma (New York, N.Y.), May 2009. PMID: 19449047
- F. Santini, **S. Patil**, S. Meckel, K. Scheffler, SG. Wetzel, "Double Reference Cross-Correlation Algorithm for Separation of the Arteries and Veins from 3D MRA Time Series", J. Magn. Reson. Imaging, 28(4):646-54, 2008.
- O. Bieri, **S. Patil**, H. Quick, and K. Scheffler, "Morphing steady-state free precession", Magn Reson Med, vol. 58, p. 1242-8, Dec. 2007.
- F. Santini, T. Schubert, **S. Patil**, S. Meckel, S.G. Wetzel, K. Scheffler, "Automatic reference selection for artery/vein separation from time-resolved 3D contrast-enhanced MRA datasets", Journal of Magnetic Resonance Imaging, under review.
- **S. Patil**, D. Jirak, M. Hajek, K. Scheffler, "Positive Contrast Visualization of the SPIO-labled Pancreatic Islets using Echo-dephased Steady State Free Precession", Mangetic Resonance in Medicine, in preparation.

Conference Contributions

- **S. Patil**, R. Umathum, M. Bock, J. Anders, G. Boero, K. Scheffler, "Highly miniaturized micro coil for tracking of the interventional devices", Proceedings of the 17th Scientific meeting of ISMRM, Hawaii, pp. 2009.

- **S. Patil**, O. Bieri, P. Jhooti, K. Scheffler, "Automatic slice positioning of the interventional device using passive paramagnetic markers", Proceedings of the 17th Scientific meeting of ISMRM, Hawaii, pp. 2009.

- **S. Patil**, O. Sabrowski, F. Santini, O. Bieri, K. Scheffler, "Positive contrast visualization of SPIO labeled cells using Echo dephased SSFP", ESMRMB 2008 Congress, Valencia, Spain, 2-4 October: EPOS Gao Posters/Info-RESO. Magma:775;21 Suppl 1:235-489, 2008.

- **S. Patil**, R. Umathum, M. Bock, J. Anders, G. Boero, K. Scheffler, "Highly miniaturised micro coil for tracking of the interventional devices", Proceedings of the 7th Interventional MRI Symposium (Oral Presentation), 2008.

- **S. Patil**, O. Bieri, P. Jhooti, K. Scheffler, "Automatic slice positioning of the interventional device using passive paramagnetic markers", Proceedings of the 7th Interventional MRI Symposium, 2008.

- P. Jhooti, S. Blanco, **S. Patil**, K. Scheffler, "MRI scanner control using foot controllers during MR-guided interventions: when one pair of hands just isn't enough", Proceedings of the 7th Interventional MRI Symposium, 2008.

- **S. Patil**, O. Bieri, P. Jhooti, D. Bilecen, K. Scheffler, "Passive guide wire visualization in an interventional MRI using dephased SSFP", Proceedings of the 19th International Conference on Magnetic Resonance Angiography (Oral Presenation), 2007.

- O. Bieri, **S. Patil**, K. Scheffler, "Morphing-SSFP: A new method for fast detection of strong magnetic field inhomogeneities and its application for tracking ferromagnetic devices", Proceedings of 15th joint annual meeting ISMRM-ESMRMB, Berlin,Germany, pp. 294, 2007.

- **S. Patil**, C. Boller, D. Bilecen, K. Scheffler, "Visualization of the paramagnetic markers in interventional MRI using spatial-spectral pulses", Proceedings of 15th joint annual meeting ISMRM-ESMRMB, Berlin,Germany, pp. 1122, 2007.

- **S. Patil**, O. Bieri, D. Bilecen, K. Scheffler, "An Echo-dephased SPGR approach to generate positive contrast due to paramagnetic marker: an interventional MRI application", Proceedings of 15th joint annual meeting ISMRM-ESMRMB, Berlin,Germany, pp. 1119, 2007.

- F Santini, **S. Patil**, S. Meckel, K. Scheffler, S. Wetzel, "Artery/vein separation and fistula detection in MR angiography through double-reference correlation analysis", Proceedings of the 31st Congress of ESNR (Oral Presentation), Geneva, Switzerland, 2006.

- F. Santini, **S. Patil**, S. Meckel, S. Wetzel, K. Scheffler, "Double-reference correlation algorithm for artery and vein separation in contrast enhanced MR angiography", Proceedings of the 23rd annual scientific meeting of ESMRMB, Warsaw, Poland, pp. 47-48, 2006.

- **S. Patil**, D. Bilecen, K. Scheffler, "Efficient Marker Detection Using Variable Dephasing Gradient Double Echo Sequence-an Interventional MRI Application", Proceedings of the 23rd annual scientific meeting of ESMRMB (Oral Presentation), Warsaw, Poland, pp. 173-174, 2006.

Contents

Chapter 1

Introduction to MR device Tracking

1.1 Introduction

Adequate visualization of the vascular structure and surrounding anatomy as well as the devices inside the body is required to perform endovascular interventions. Currently X-ray fluoroscopy and digital subtraction angiography (DSA) are used to visualize endovascular devices and contrast media in the vessel lumen (see Fig. 1.1). This modality provides sufficient temporal resolution and a spatial resolution of the order of 0.1 mm, enough to resolve any vessel that can possibly be operated. Thus, this modality has proven to be extremely successful with millions of patients annually diagnosed and treated worldwide. X-ray fluoroscopy, however, provides poor soft-tissue contrast and little functional information. The (iodinated) contrast agents used under X-ray fluoroscopy cause adverse reactions in a significant number of patients. Both medical personnel and patients are exposed to ionizing radiation [1].

Historically, MRI has not been considered as an alternative imaging modality for endovascular procedures, primarily due to its relatively long image acquisition times and the closed nature of the magnets. However, a number of properties of MRI distinguish itself from other clinical modalities (for e.g. X-ray, PET) such as its lack of ionizing radiation, three-dimensional imaging, arbitrary scan plane positioning, excellent soft-tissue and bone contrast, its capability to acquire both anatomic and physiologic information and the exploitation of the many functional parameters of MRI such as perfusion, flow, diffusion, thermal imaging, and the blood oxygenation level-dependent (BOLD) effect. These broad variety of available techniques make MRI an attractive imaging method for diagnostic and therapeutic procedures. Due to the continued development of MR hardware for faster image acquisition and reconstruction, along with developments such as steady state free precession (SSFP) and parallel imaging techniques, real-time MR imaging is now a clinical reality[2, 3]. With the trend toward shorter and more open magnet designs, endovascular MR-guided interventions have evolved from a research tool to a preclinical method over the last decade with a few applications that have entered the clinical arena [4].

In clinical practice, however, one of MRI's drawbacks is the difficulty in localization and high-contrast visualization of interventional devices (for e.g., guidewires, catheters, and needles). In addition, fast localization and automatic adjustment of scan plane position is highly desirable. As a result, considerable efforts are being undertaken towards achieving these objectives. In the following, general overview of the strategies that are exploited to localize and/or visualize them is described in detail. Much of this overview has been inspired from existing literature [5–8]. Current methodologies for MR-guided interventions can be broadly classified into active, semi-active and passive tracking.

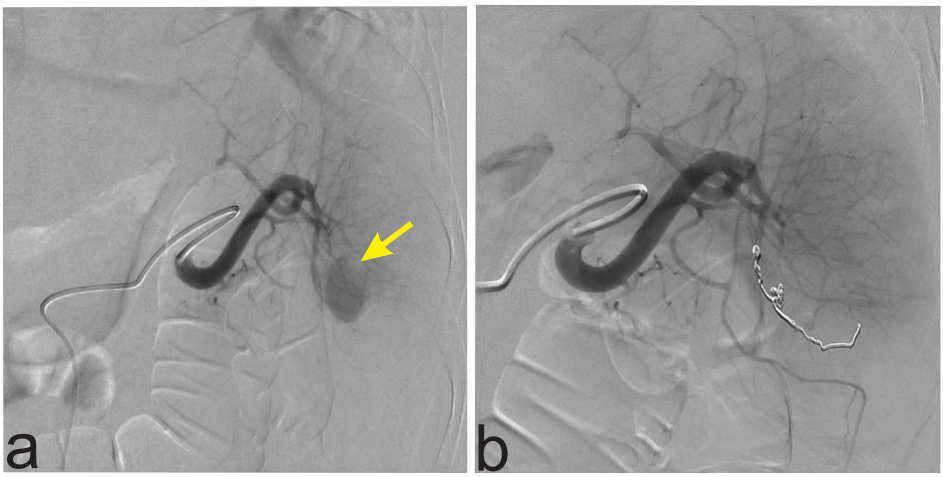

Figure 1.1: An examination of a traumatic spleen injury with a bleeding from an internal spleen artery. a) After selective placement of an arterial catheter in the spleen artery, the bleeding origin is seen in the inferior pole (yellow arrow). b) After super selective placement of an embolisation coil in a inferior spleen artery the bleeding is stopped and no extra-vascular contrast accumulation is observed.

1.2 Active Tracking

The first catheter-mounted coil was proposed to improve signal-to-noise ratio of ^{31}P spectroscopy of the canine heart [9]. Active tracking utilizes locally sensitive transmit/receive coils for either localization [10, 11] or visualization [12] (see Fig. 1.2) or is based on the visualization of current related local field inhomogeneities produced in a small loop [13]. Localization of the coil is achieved in few milliseconds through acquisition of one dimensional (1D) projections along all three spatial directions (X, Y and Z). Since the sensitivity of the micro-coils is confined to small region, projections obtained show a peak corresponding to its position. In order to avoid off-resonance effects due to field inhomogeneities, hadamard-encoded four projections are acquired [11]. The positional information is then used to actively align the position of the imaging slice. With this method, the instrument tip position is detected within 20 ms [14–17]. In addition, velocity of the device has been used to automatically adjust the imaging parameters [18]. It has also been demonstrated that position of the micro-coil can be detected between the acquisition of two real-time images (for e.g. using balanced SSFP (bSSFP), TrueFISP) and the information can be used to reposition the imaging slice [19, 20].

In order to overcome the disadvantage of using one micro-coil and thereby detecting only the tip of the instrument, approaches are proposed to visualize either the curvature of the coil or the entire length of the coil [12, 21, 22].

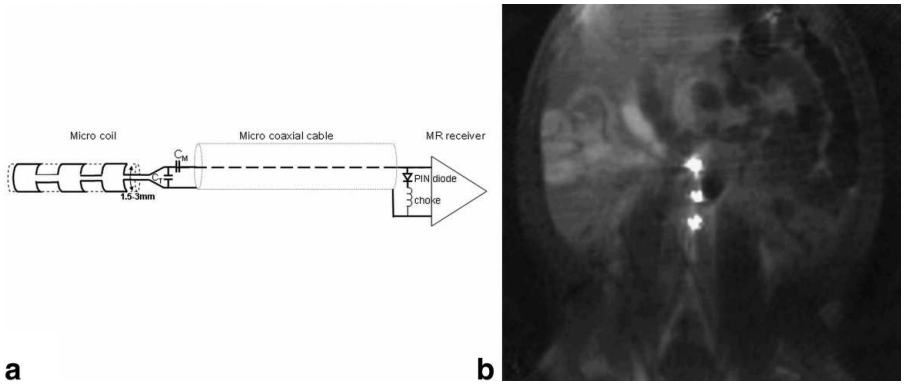

Figure 1.2: Three Marker tracking coil. a) Schematic drawing of three-element capacitively coupled tracking coil. Circuit is tuned to Larmor frequency of MR-scanner and matched to 50 Ω at the tip of catheter using capacitors C_T and C_M. Active detuning via positive-intrinsic-negative (PIN) diode and choke is accomplished remotely. 50 Ω microcoaxial cable connects tracking coil to MRI receiver. b) Image from a tracking experiment. The three-marker tracking coil is guided in the abdominal aorta of a pig. Adapted from Wacker et. al.,[18]

Another advantage of utilizing micro-coils is the possibility to use the MR signal not only for device tracking but also for vessel wall imaging or functional studies [23–25].

However, potential radiofrequency (RF) heating issues due to standing waves along the conducting cables still represent one of the major and most prominent potential safety hazards with active tracking [26] (Fig. 1.3). The standing waves lead to storage of electrical energy, which may be transmitted into the human body. With nitinol guidewires temperatures of up to 74^0C has been reported [26]. Some approaches have been suggested to reduce the heating risks, see for example Ref. [27], but widespread use of active tracking in humans is still limited due to design challenges.

1.3 Semi-active Tracking

Semi-active devices utilize self-resonant RF circuits and have no direct electrical connection to the scanner. Such devices incorporate miniature RF coils tuned to Larmor frequency of the scanner and encapsulates a small container filled with a solution having short T_1 [28, 29]. As a result, using a fast imaging sequence with low flip angles generates a positive contrast for the sample within the coil due to local gain of the B_1 field [30, 31], in combination with the relatively low signal from the background (see Fig. 1.4). Since inductively coupled coils do not utlize extended long conduct-

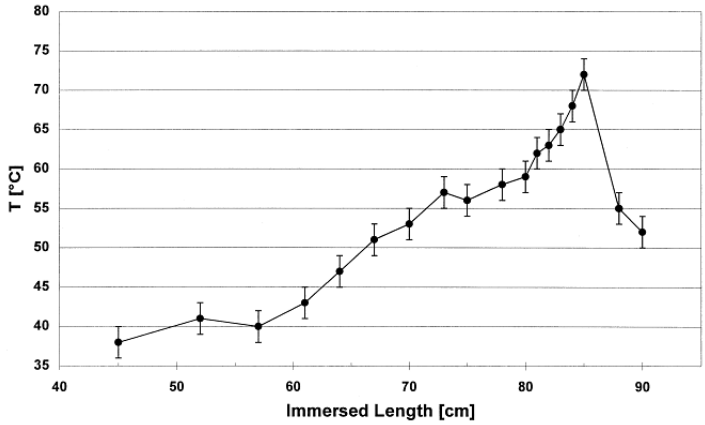

Figure 1.3: RF Heating. Graph showing the temperature of the distal guidewire tip after 30 seconds of scanning. The temperature was measured for various immersed lengths of the guidewire. Before each measurement, the guidewire tip was allowed to cool down to 26^0C. Each measurement was performed three times. Adapted from Konings et. al., [26]

ing structures, heating of the coils due to E-field coupling is avoided if the wavelength of the electric field in tissue is longer than the coil dimension. However, semi-active devices might still lead to severely increased local specific absorption rate (SAR) values due to their resonant coupling to the B-field of the RF. In addition, semi-active devices require a mechanical connection (for e.g. laser fiber) between the instrument and the scanner which greatly hampers the handling of such interventional devices.

1.4 Passive Tracking

In passive tracking, the interventional device is made to be visible on the MR image itself and does not require any additional harware or image post-processing and hence the name. To this end, two types of appoaches are proposed in the literature: one using contrast agents (such as 4-6 vol % Gd-DTPA) that increases the MR signal [33, 34] and the other one utilizes small paramagnetic materials that is placed on to the interventional device [35–37]. Contrary to active tracking, passive techniques do not suffer from RF heating problems. Moreover, unlike semi-active devices passive devices do not require any mechanical scanner connection. This inherent safety feature of the passive tracking devices is the major reason why it is fast becoming clinical reality [4, 38] as compared to active or semi-active devices.

The passive tracking methods utilizing contrast agents fills the interventional device (for e.g. catheter) with a T_1-shortening agents (See Fig. 1.5). By utilizing strong T_1-weighted sequence, tracking of the device can

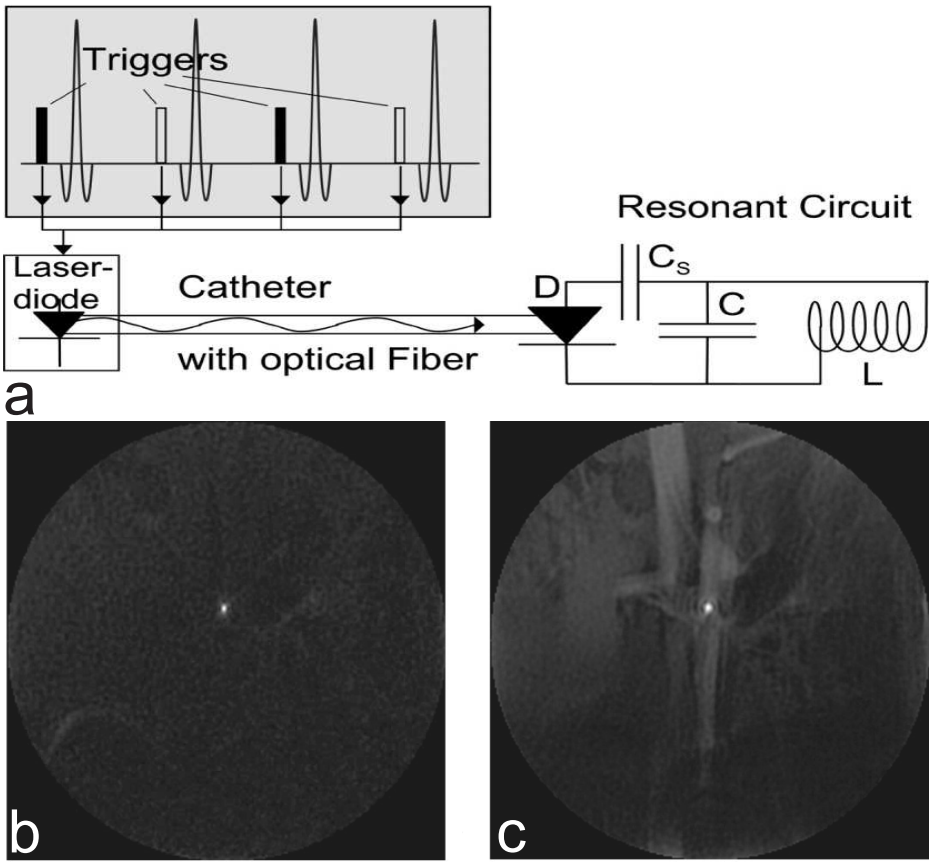

Figure 1.4: Semi-active tracking. a) The MR sequence controls the detuning of the resonant circuit by means of software triggers, which are programmable in the MR scan software. Corresponding hardware triggers on the scanner interface are used to switch a laser diode, which illuminates the photodiode D at the catheter tip via an optical fiber. b,c) Real-time frames acquired with flip angles of 5^0, 20^0 respectively, demonstrate that the contrast of the resonant marker with respect to the background can be adjusted interactively by varying the flip angle. Adapted from Weiss et. al., [32]

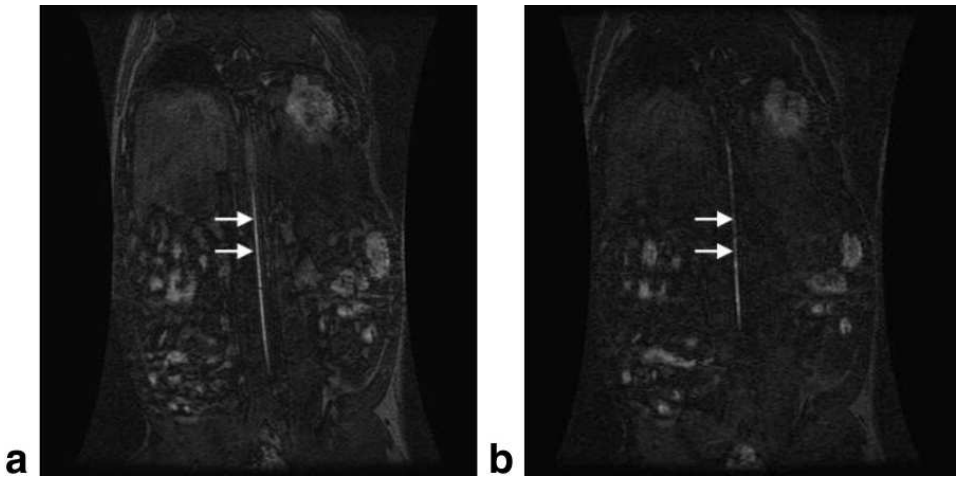

Figure 1.5: Coronal MIP images of a 6-French catheter filled with a) 4% Gd-DTPA and b) a 4-French catheter coated with T_1-shortened agent in a canine aorta. Adapted from Unal et. al., [34]

be achieved with positive contrast [33, 39]. The obvious difficulty of this approach is that the insertion of guidewire is not possible since the catheter lumen is filled with contrast agent. Hence, another variation of this approach is the development of a T_1-shortened coating for the devices [34]. In spite of this positive development, handling of the agent-filled or coated instruments remains problematic.

The alternative approach of passive tracking utilizes paramagnetic materials such as dysprosium oxide [37] or stainless steel materials [40] and was first introduced by Rubin et al [35] for interventional device visualization. The paramagnetic markers or materials cause significant field inhomogeneities when placed in a uniform main magnetic field B_0, due to its local susceptibility differences with respect to surrounding tissues [41]. From MRI point of view, this so called field inhomogeneity has a dual effect of local frequency shifts and local gradient perturbations. This source of field inhomogeneity has been exploited as a form of image contrast for passive visualization and tracking of the interventional devices as well as super-paramagnetic iron oxide (SPIO)-labeled cells. The early reports of passive tracking have been demonstrated in a human volunteer [42]. Since then many studies have been published in pigs [43, 44] as well as been successful in patients [4, 45]. The development of MR-compatible guidewires either made up of PEEK material [40, 44, 46] or glass-fiber reinforced plastic materials [47] also incorporates MR-visible paramangetic markers.

Traditionally the visualization of these paramagnetic materials is based on increase in T_2^* decay that they cause entailing a negative contrast (signal loss) with respect to background in a resultant image (Fig.1.6). Gradient-

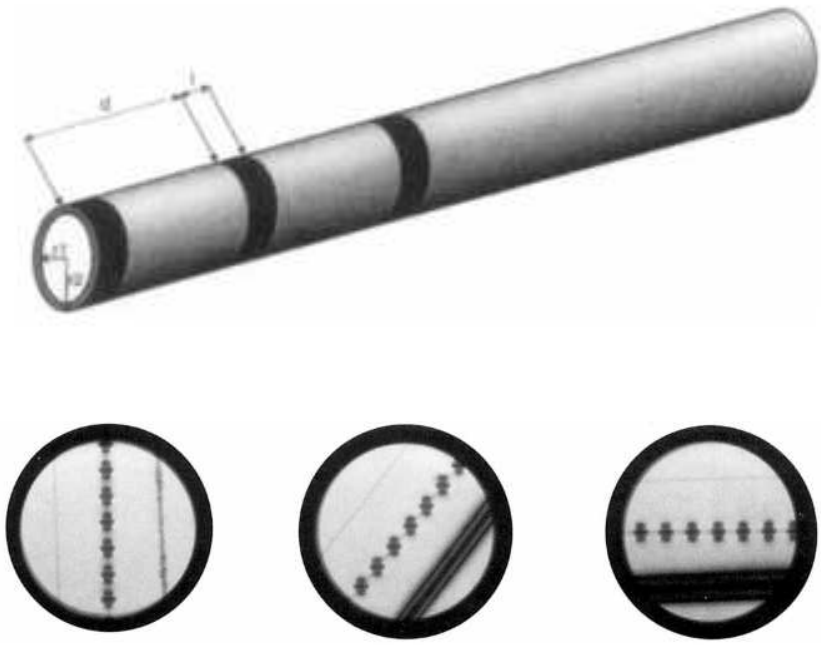

Figure 1.6: Passive Tracking. Upper panel shows schematic drawing of a polyethylene catheter with a equally spaced paramagnetic rings made up of Dysprosium oxide. The lower panel shows gradient-echo images of a catheter immersed in a water bath and oriented (from left to right) parallel, oblique and perpendicular to B_0. Adapted from Bakker et. al. [37]

echo sequences are the current de-facto standard to visualize these T_2^*-based effects [35–37], since the magnetic field inhomogeneities have strong impact on signal properties of these type of sequences [48]. Unfortunately, due to confounding background signals it is often difficult to distinguish signal loss due to paramagnetic materials from other unwanted inhomogeneities such as, air/tissue interfaces etc.

Therefore, MRI techniques that generate positive contrast that are localized within the immediate surroundings of the paramagnetic materials while suppressing the background signals have been proposed. One simple approach is to acquire base-line anatomical image and then subtract this image from subsequent images containing susceptibility-based artifact due to presence of paramangetic marker [49, 50]. Clearly this approach is susceptible to motion. The concurrent state-of-the-art positive contrast techniques can be broadly classified into three categories based upon their method of identifying paramagnetic materials: those using local frequency shifts in the on-resonance frequency [40, 51, 52], those exploiting the local

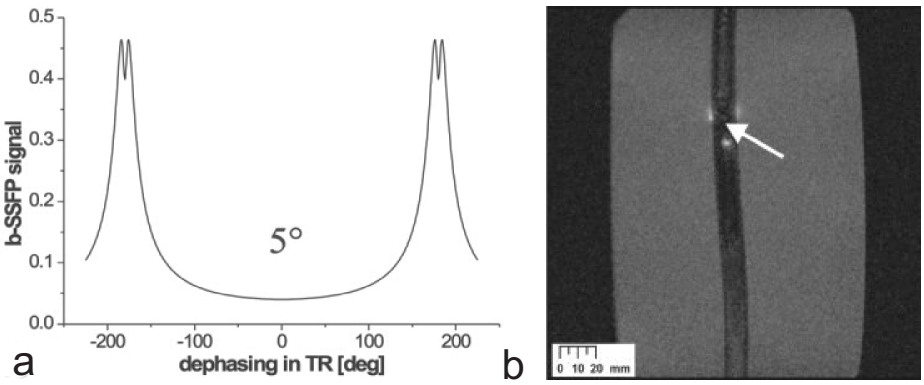

Figure 1.7: Passive tracking exploiting local frequency shifts. a) Signal amplitude of bSSFP sequences vs. dephasing during each TR period. Signal bands for $\alpha = 5^0$. b) Induced artifact at tip of guidewire in bSSFP acquisition with flip angle $\alpha = 5^0$. The guidewire was inserted into a flow phantom. Adapted from Mekle et. al; [40]

gradient compensation by the imaging gradients [53] and those mapping the susceptibility-induced gradients as a post-processing step [54, 55].

The methods that exploit local frequency shifts to create positive contrast techniques are either based on temporally inefficient spin-echo type of sequences incorporating specially designed RF pulses [52] or are susceptible to main magnetic field inhomogeneities [51]. This makes them unsuitable for passive tracking of interventional devices, where fast detection of marker is desirable. Alternatively, Mekle et.al proposed a fast passive tracking approach based on special properties of bSSFP sequence at low flip angles giving rise to positive contrast within the close vicinity of the marker due to off-resonance effect [40] (See Fig. 1.7).

The positive contrast imaging methods that exploit local gradient compensation effect are based on deliberate modification of slice select gradients that dephases background signals whereas marker-related local gradients compensate for the dephasing gradients to produce locally a positive contrast [56] and is commonly known as "White Marker Phenomenon" (See Fig. 1.8).

1.4.1 Morphing SSFP

[1] Recently yet another novel passive tracking concept, termed morphing SSFP that tackles the issue of background signal suppression was introduced [57]. Morphing SSFP generates positive contrast from the fusion of two pe-

[1] **This section is partially based upon:**
O. Bieri, **S. Patil**, H. Quick, and K. Scheffler, "Morphing steady-state free precession", Magn Reson Med, vol. 58, p. 1242-8, Dec. 2007

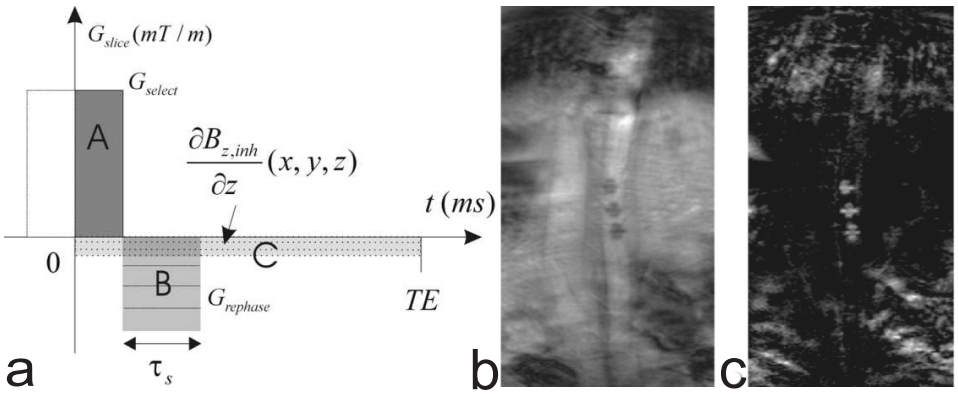

Figure 1.8: a) Schematic depiction of the concept of signal conservation for gradient areas in the slice selection direction. In general, after excitation at t = 0 msec, the slice selection gradient G_{select} dephases (area A) the spins. To rephase the excited spins, normally the full area B compensates for the slice selection area. Reducing area B creates a gradient imbalance, effectively resulting in a signal decrease. However, in spatial regions with a negative local gradient due to the dipole field (area C), the gradient balance is restored and signal remains conserved, whereas other regions will experience signal loss. b) In vivo imaging of three paramagnetic markers, mounted on a 5-F catheter, located in the abdominal aorta of a living pig, as visualized with conventional gradient echo sequence and c) dephased positive contrast gradient echo imaging. Adapted from Seppenwoolde et. al; [53]

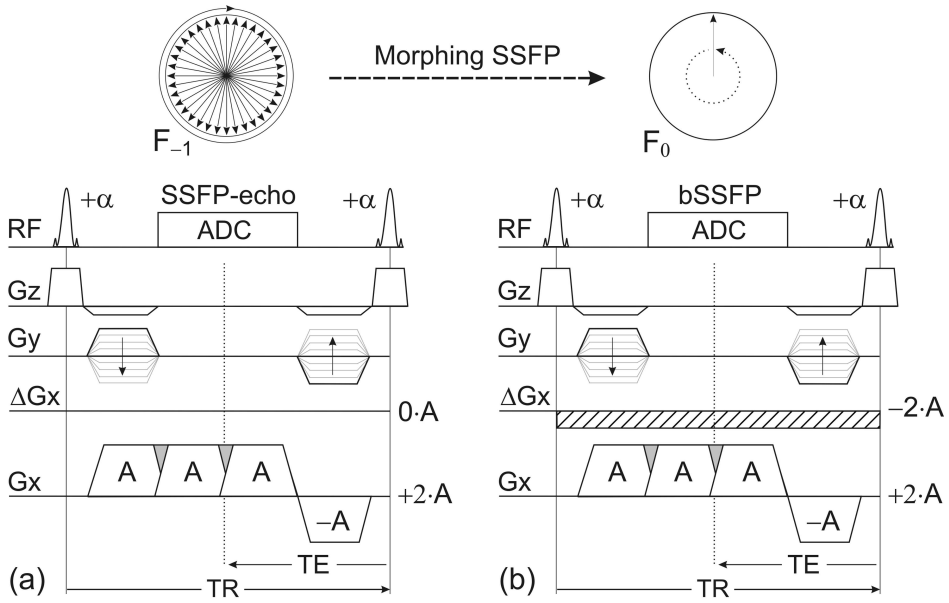

Figure 1.9: Conceptual illustration of morphing SSFP. (a) SSFP-echo sequence dephases spins by 2π/voxel within any TR (area: 2A). Local magnetic field distortions from paramagnetic marker materials are indicated by ΔG_x. (b) In close proximity to the marker, $\Delta G_x >> 0$, and local gradient compensation may form a balanced SSFP type of echo. Thus, within the same image unbalanced SSFP may change, i.e. morph, to bSSFP.

culiarities, namely (i) local gradient compensation in unbalanced SSFP and (ii) low flip angle properties of balanced and unbalanced SSFP. The local field gradients in morphing SSFP compete with the sequence-related generic in-plane or through-plane dephasing gradient of an SSFP-echo (PSIF, T_2-FFE, CE-FAST) to induce a transition to bSSFP, and hence the name. This transition intrinsically generates a positive contrast. The background suppression in morphing SSFP is based on prominent intrinsic signal differences between bSSFP and SSFP-echo; in particular their flip angle and off-resonance behavior. SSFP-echo is insensitive to the amount of off-resonance related precession within each TR period, whereas bSSFP sequences exhibit strong signal modulations that also depend on the flip angle α. For small α (2-5^0), narrow signal maxima are surrounded by large regions of near zero signal. It can be shown that the signal maxima are almost independent of the flip angle used. This property of bSSFP is well known and was already described by Carr [58] in the late 1950s. The conceptual illustration of morphing SSFP concept is shown in Fig.1.9.

An overview of the experimental setup is shown in Fig. 1.10a. The displayed coronal image (in plane with the perturber) was acquired based

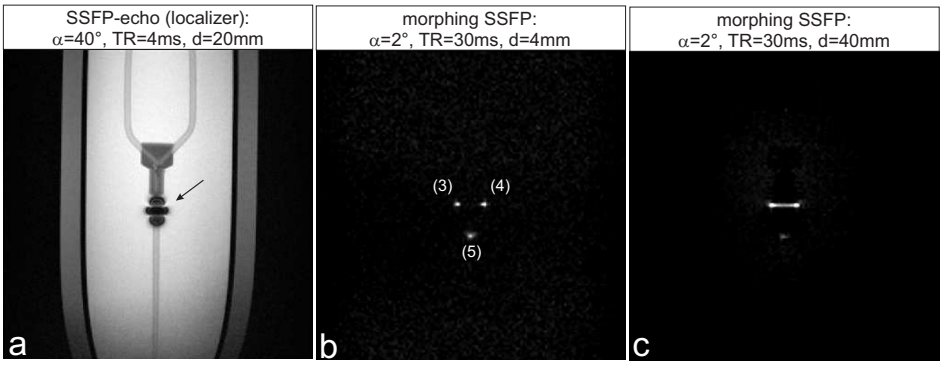

Figure 1.10: Phantom studies. (a) Coronal SSFP-echo image of the experimental setup. The susceptibility related image artifact (signal void, black arrow) from the inserted paramagnetic material is clearly visible within the phantom. b,c: Although, generally, any SSFP-echo signal is reduced to the noise due to a decrease in the flip angle to its very low limit, strong signals emanate near the marker material. Here, local gradient compensation morphs SSFP-echo to bSSFP and hyperintense signals ((3), (4), (5)) are formed for properly adjusted local frequencies.

on a standard SSFP-echo imaging protocol with short TR and moderate flip angle (TR=4ms, $\alpha = 40^0$). Signal loss from an increased susceptibility-related transverse relaxation is clearly visible and identifies the location of the paramagnetic material. Since peak signal intensities in bSSFP show almost no dependence on the flip angle, background signals from SSFP-echo fade for low flip angles (see Fig. 1.10a). In contrast to Fig. 1.10a, the signal from the background in Figs. 1.10b and 1.10c is close to the noise level ($S_{BG} = 60$ au, $S_{noise} = 45$ au, au: arbitrary units) as a result of the low flip angle ($\alpha = 2^0$) and long TR (30ms). However, well-defined regions near the paramagnetic material feature a considerable jump in signal intensity (Fig. 1.10b, $S_{object} = 340$ au) and thus appear hyperintense. In these focal spots, not only local gradients compensate for the sequence related dephasing to form a bSSFP echo, but peak signal intensities indicate properly adjusted frequencies, i.e. frequency matching.

The demonstration of morphing SSFP concept was done in vivo as well. The guidewire was placed in the infrarenal aorta of a pig. The final position of the marker material is shown in Fig. 1.11a. In complete analogy to the phantom experiments (Fig. 1.10), morphing SSFP produces hyperintense signals (Fig. 1.11b) only in the close vicinity to the perturber, irrespective of any background complexity (susceptibility changes from tissue air-tissue boundaries, field inhomogeneities, and so on). A superposition of the morphing SSFP image (Fig. 1.11b) on a standard (localizer) bSSFP image (Fig. 1.11a) is shown in Fig. 1.11c. The overlay reveals no shift of hyperintense

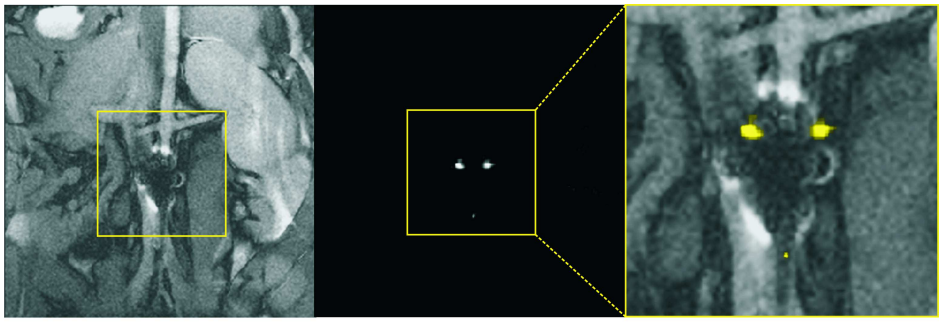

Figure 1.11: In vivo experiments. (a) Real-time bSSFP sample image displaying the final placement of guidewire (marker material) into the renal artery of the pig (localizer image). (b) Corresponding morphing SSFP image ($\alpha = 7^0$, TR=30ms, 5mm slice thickness). As in the phantom experiments (Fig. 1.10), hyperintensities manifest as point-like structures on a uniformly suppressed background, even in the presence of complex tissue interfaces. (c) Overlay of morphing SSFP (yellow) on the localizer image (for the area indicated by the yellow rectangle) ensures proper localization and detection of the marker material.

pixels from morphing SSFP with respect to the susceptibility artifact and thus ensures proper detection and localization of marker materials.

1.5 Aim of this Thesis

There is a long history of positive contrast sequences to be applicable for passive tracking of interventional devices. In spite of this there is a growing need to further investigate the novel and fast positive contrast sequences and demonstrate its performance to reduce background sensitivity. For example, the methods that are based on post-processing steps are computationally cumbersome to consider for interventional device tracking applications and hence can not be utlized. As pointed out earlier, the methods that are based on exploitation of local frequency shifts are unsuitable for passive tracking of interventional devices, where fast detection of marker is desirable. In addition, poor shimming, large field-of-views (FOV), or susceptibility boundaries, however, may hamper a reliable tracking with low flip angle bSSFP variant, since these field inhomogeneities would induce image artifacts similar to those from marker materials. To overcome these disadvantages, in this thesis binomial spatial-spectral excitation pulse (SPSP pulse) exploiting local frequency shift effect is incorporated into a temporally efficient SSFP-echo sequence to generate positive contrast due to paramagnetic materials.

One of the major prerequisite for successful passive tracking is the feasi-

bility of image acquisitions with extended slab thickness (40-50 mm) to guarantee that the marker material always lies within the plane being imaged. However, application of dephasing gradients using extended slice thickness as suggested by "White Marker Phenomenon" [53] may also enhance other unwanted background signals, e.g. from air/tissue interfaces and thereby hampering proper marker localization and visualization. The previously proposed method; morphing SSFP [57] requires long TR and hence may prove to be temporally inefficient for interventional applications. To overcome these advantages, in this thesis we develop the idea of gradient compensation in SSFP to locally induce high signal intensities. In the close vicinity of paramagnetic materials, strong local gradient fields may compensate for any sequence-related gradients to locally induce signal transitions from an echo-dephased to an echo-rephased type of SSFP (mainly bSSFP) sequence.

Although positive contrast imaging enhances the conspicuity of the marker as compared to the background, it results in a loss of anatomical structure. Thus, passive tracking or localization of the guidewire can be achieved using a baseline subtraction method or a positive contrast image overlaid on either anatomical reference images or a vascular roadmap (i.e., an angiogram). However, relatively long image acquisition times, leads to an undesired increased sensitivity to motion and/or flow with such overlay techniques. In the third part of this thesis a novel projection-based passive tracking technique is proposed, termed Projection Reconstruction Imaging with Echo-DEphasing (PRIDE). PRIDE is based on an acquisition of projections using dephasing gradients along all three spatial (X, Y and Z) dimensions. Using PRIDE, 3D position of the interventional device tip containing paramagnetic marker is localized, which in turn is used to automatically adjust the scan plane of the imaging slice.

The dimensions of the coils proposed for active tracking approaches are bulky in nature thereby increasing the size of normal interventional devices (for e.g. catheter). In addition, the sensitivity of the coil and hence, the spatial resolution is directly proportional to coil dimensions. As compared to x-ray fluoroscopy that offers a device localization resolution in the range of the order of 0.1 mm, the current device dimensions limit the resolution in MRI. Hence the final aim of this thesis is to introduce and experimentally test the highly miniaturized planar micro coils with built-in amplifier.

1.6 Outline of the Thesis

The main content of the thesis is divided into several different parts. In the first part, two novel positive contrast imaging approaches to visualize paramagnetic marker materials are described. Next, real-time tracking of interventional devices is examined in detail and the results are presented. Finally, highly miniaturized micro-coils are experimentally tested that could

be used to visualize interventional catheters.

This thesis is organized as follows:

Chapter 2: Spatial-spectral SSFP

In this chapter, firstly the principle of off-resonance excitation of tissues using SPSP pulse is explained theoretically. The in-vitro experiments demonstrate the proper localization and feasibility of paramagnetic marker detection mounted on the interventional guidewire tip. The signal and localization characteristics of the SPSP pulse are analyzed theoretically and verified experimentally.

Chapter 3: Echo-dephased SSFP

In the close vicinity of paramagnetic materials, strong local gradient fields may compensate for any sequence-related gradients to locally induce signal transitions from an echo-dephased to an echo-rephased type of SSFP (mainly balanced SSFP (bSSFP)) sequence. Generically resembling an unbalanced SSFP, in echo-dephased SSFP echoes are preferably dephased by $\pm\pi$ prior to readout. This not only ensures excellent cancellation of any background signals but also generic dephasing from unbalanced SSFP greatly reduces unwanted background signal enhancements. It will be demonstrated that due to the higher in-plane resolution as compared to slice resolution, local gradient compensation in echo-dephased SSFP is likely to take place only within the close vicinity of the paramagnetic marker material. The conceptual issues of gradient compensation and its signal properties are analyzed and discussed. To demonstrate the feasibility of proper marker visualization and localization using echo-dephased SSFP, reliable tracking of MR compatible interventional guidewire having paramagnetic material on it is demonstrated in a simple flow phantom. The utility of the echo-dephased SSFP is also shown for positive contrast visualization of human pancreatic islets labeled with superparamagnetic iron oxide (SPIO) contrast agent in vitro. Finally in vivo experiments in a rat model demonstrates the robust and reliable visualization of transplanted SPIO-labeled pancreatic islets in a rat chamber.

Chapter 4: Projection Reconstruction Imaging with Echo-Dephasing (PRIDE)

In this chapter a novel projection-based passive tracking technique is proposed, termed Projection Reconstruction Imaging with Echo-DEphasing (PRIDE). PRIDE is based on an acquisition of projections using dephasing gradients along all three spatial (X, Y and Z) dimensions. Using PRIDE, 3D position of the interventional device tip containing paramagnetic marker is localized, which in turn is used to automatically adjust the scan plane of the

imaging slice. We first describe the concept of local gradient field compensation used in PRIDE, followed by in-vitro experiments demonstrating the feasibility of appropriate marker detection in the presence of off-resonance related degradations caused by unwanted inhomogeneities (air/tissue interfaces etc). Then we describe the ASP mechanism incorporating PRIDE as a tracking sequence to provide positional information of the paramagnetic marker to bSSFP sequence serving as an imaging sequence. The demonstration and discussion of ASP mechanism on the clinical scanner is done by means of phantom results. Finally, in vivo experiments in a swine model are presented that corroborate the in-vitro results for robust and reliable detection of marker using PRIDE.

Chapter 5: Highly Miniaturized Micro-coil

The aim of this chapter is to demonstrate the feasibility of these miniaturized micro-coils to utilize them as the tracking coil on a clinical scanner with an aid of phantom experiments. In the first part of this chapter, we describe the experimental arrangements and MR sequence parameters. Next, the results obtained by means of spectroscopic, imaging and 1D projection are presented. Perspectives from the results conclude the chapter.

Chapter 6: Summary and Future Outlook

This chapter summarizes the contributions presented in the previous chapters and provides possible future research directions.

References

[1] R. Geise and R. Morin, "Radiation measurement in interventional radiology.," in *Interventional Radiology* (W. Castaneda-Zuniga, ed.), pp. 1–8, Baltimore: Williams and Wilkins, third ed., 1997.

[2] V. K. Raman, P. V. Karmarkar, M. A. Guttman, A. J. Dick, D. C. Peters, C. Ozturk, B. S. S. Pessanha, R. B. Thompson, A. N. Raval, R. DeSilva, R. J. Aviles, E. Atalar, E. R. McVeigh, and R. J. Lederman, "Real-time magnetic resonance-guided endovascular repair of experimental abdominal aortic aneurysm in swine," *Journal of the American College of Cardiology*, vol. 45, p. 2069–2077, June 2005. PMID: 15963411.

[3] F. K. Wacker, C. M. Hillenbrand, J. L. Duerk, and J. S. Lewin, "MR-guided endovascular interventions: device visualization, tracking, navigation, clinical applications, and safety aspects," *Magnetic Resonance Imaging Clinics of North America*, vol. 13, p. 431–439, Aug. 2005. PMID: 16084411.

[4] R. Razavi, D. Hill, S. Keevil, M. Miquel, V. Muthurangu, S. Hegde, K. Rhode, M. Barnett, J. van Vaals, D. Hawkes, and E. Baker, "Cardiac catheterisation guided by MRI in children and adults with congenital heart disease," *Lancet*, vol. 362, p. 1877–82, Dec. 2003.

[5] M. E. Ladd, H. H. Quick, and J. F. Debatin, "Interventional MRA and intravascular imaging," *Journal of Magnetic Resonance Imaging: JMRI*, vol. 12, pp. 534–546, Oct. 2000. PMID: 11042634.

[6] J. L. Duerk, E. Y. Wong, and J. S. Lewin, "A brief review of hardware for catheter tracking in magnetic resonance imaging," *Magma (New York, N.Y.)*, vol. 13, no. 3, pp. 199–208, 2002. PMID: 11755097.

[7] L. W. Bartels and C. J. G. Bakker, "Endovascular interventional magnetic resonance imaging," *Physics in Medicine and Biology*, vol. 48, pp. R37–64, July 2003. PMID: 12894968.

[8] M. Bock and F. K. Wacker, "MR-guided intravascular interventions: techniques and applications," *Journal of Magnetic Resonance Imaging: JMRI*, vol. 27, pp. 326–338, Feb. 2008. PMID: 18219686.

[9] H. L. Kantor, R. W. Briggs, and R. S. Balaban, "In vivo 31P nuclear magnetic resonance measurements in canine heart using a catheter-coil," *Circulation Research*, vol. 55, p. 261–266, Aug. 1984. PMID: 6744535.

[10] J. L. Ackerman, M. C. Offut, R. B. Buxton, and T. J. Brady, "Rapid 3D tracking of small RF coils.," in *Proceedings of the SMRM*, (Montreal), p. 1131, 1986.

[11] C. Dumoulin, S. Souza, and R. Darrow, "Real-time position monitoring of invasive devices using magnetic resonance," *Magn Reson Med*, vol. 29, p. 411–5, Mar. 1993.

[12] O. Ocali and E. Atalar, "Intravascular magnetic resonance imaging using a loopless catheter antenna," *Magn Reson Med*, vol. 37, no. 1, p. 112–8, 1997.

[13] A. Glowinski, G. Adam, A. Bucker, J. Neuerburg, J. van Vaals, and R. Gunther, "Catheter visualization using locally induced, actively controlled field inhomogeneities," *Magn Reson Med*, vol. 38, p. 253–8, Aug. 1997.

[14] C. Flask, D. Elgort, E. Wong, A. Shankaranarayanan, J. Lewin, M. Wendt, and J. L. Duerk, "A method for fast 3D tracking using tuned fiducial markers and a limited projection reconstruction FISP (LPR-FISP) sequence," *Journal of Magnetic Resonance Imaging: JMRI*, vol. 14, p. 617–627, Nov. 2001. PMID: 11747015.

[15] S. Zuehlsdorff, R. Umathum, S. Volz, P. Hallscheidt, C. Fink, W. Semmler, and M. Bock, "MR coil design for simultaneous tip tracking and curvature delineation of a catheter," *Magn Reson Med*, vol. 52, p. 214–8, July 2004.

[16] M. E. Ladd, G. G. Zimmermann, G. C. McKinnon, G. K. von Schulthess, C. L. Dumoulin, R. D. Darrow, E. Hofmann, and J. F. Debatin, "Visualization of vascular guidewires using MR tracking," *Journal of Magnetic Resonance Imaging: JMRI*, vol. 8, pp. 251–253, Feb. 1998. PMID: 9500289.

[17] M. Wendt, M. Busch, R. Wetzler, Q. Zhang, A. Melzer, F. Wacker, J. L. Duerk, and J. S. Lewin, "Shifted rotated keyhole imaging and active tip-tracking for interventional procedure guidance," *Journal of Magnetic Resonance Imaging: JMRI*, vol. 8, p. 258–261, Feb. 1998. PMID: 9500291.

[18] F. Wacker, D. Elgort, C. Hillenbrand, J. Duerk, and J. Lewin, "The catheter-driven MRI scanner: a new approach to intravascular catheter tracking and imaging-parameter adjustment for interventional MRI," *AJR Am J Roentgenol*, vol. 183, p. 391–5, Aug. 2004.

[19] J. L. Duerk, J. S. Lewin, M. Wendt, and C. Petersilge, "Remember true FISP? a high SNR, near 1-second imaging method for t2-like contrast in interventional MRI at .2 t," *Journal of Magnetic Resonance Imaging: JMRI*, vol. 8, p. 203–208, Feb. 1998. PMID: 9500281.

[20] V. Rasche, D. Holz, J. Köhler, R. Proksa, and P. Röschmann, "Catheter tracking using continuous radial MRI," *Magnetic Resonance in Medicine*, vol. 37, pp. 963–968, June 1997. PMID: 9178250.

[21] M. E. Ladd, G. G. Zimmermann, H. H. Quick, J. F. Debatin, P. Boesiger, G. K. von Schulthess, and G. C. McKinnon, "Active MR visualization of a vascular guidewire in vivo," *Journal of Magnetic Resonance Imaging: JMRI*, vol. 8, pp. 220–225, Feb. 1998. PMID: 9500284.

[22] H. H. Quick, H. Kuehl, G. Kaiser, D. Hornscheidt, K. P. Mikolajczyk, S. Aker, J. F. Debatin, and M. E. Ladd, "Interventional MRA using actively visualized catheters, TrueFISP, and real-time image fusion," *Magnetic Resonance in Medicine: Official Journal of the Society of Magnetic Resonance in Medicine / Society of Magnetic Resonance in Medicine*, vol. 49, no. 1, p. 129–137, 2003. PMID: 12509828.

[23] G. C. Hurst, J. Hua, J. L. Duerk, and A. M. Cohen, "Intravascular (catheter) NMR receiver probe: preliminary design analysis and application to canine iliofemoral imaging," *Magnetic Resonance in Medicine: Official Journal of the Society of Magnetic Resonance in Medicine /*

Society of Magnetic Resonance in Medicine, vol. 24, pp. 343–357, Apr. 1992. PMID: 1569872.

[24] H. H. Quick, M. E. Ladd, G. G. Zimmermann-Paul, P. Erhart, E. Hofmann, G. K. von Schulthess, and J. F. Debatin, "Single-loop coil concepts for intravascular magnetic resonance imaging," *Magnetic Resonance in Medicine: Official Journal of the Society of Magnetic Resonance in Medicine / Society of Magnetic Resonance in Medicine*, vol. 41, pp. 751–758, Apr. 1999. PMID: 10332851.

[25] L. V. Hofmann, R. P. Liddell, J. Eng, B. A. Wasserman, A. Arepally, D. S. Lee, and D. A. Bluemke, "Human peripheral arteries: feasibility of transvenous intravascular MR imaging of the arterial wall," *Radiology*, vol. 235, pp. 617–622, May 2005. PMID: 15858101.

[26] M. Konings, L. Bartels, H. Smits, and C. Bakker, "Heating around intravascular guidewires by resonating RF waves," *J Magn Reson Imaging*, vol. 12, p. 79–85, July 2000.

[27] M. Ladd and H. Quick, "Reduction of resonant RF heating in intravascular catheters using coaxial chokes," *Magn Reson Med*, vol. 43, p. 615–9, Apr. 2000.

[28] T. Kuehne, S. Weiss, F. Brinkert, J. Weil, S. Yilmaz, B. Schmitt, P. Ewert, P. Lange, and M. Gutberlet, "Catheter visualization with resonant markers at MR imaging-guided deployment of endovascular stents in swine," *Radiology*, vol. 233, p. 774–80, Dec. 2004.

[29] S. Hegde, M. Miquel, R. Boubertakh, D. Gilderdale, V. Muthurangu, S. Keevil, I. Young, D. Hill, and R. Razavi, "Interactive MR imaging and tracking of catheters with multiple tuned fiducial markers," *J Vasc Interv Radiol*, vol. 17, p. 1175–9, July 2006.

[30] M. Burl, G. Coutts, and I. Young, "Tuned fiducial markers to identify body locations with minimal perturbation of tissue magnetization," *Magn Reson Med*, vol. 36, p. 491–3, Sept. 1996.

[31] H. H. Quick, M. O. Zenge, H. Kuehl, G. Kaiser, S. Aker, S. Massing, S. Bosk, and M. E. Ladd, "Interventional magnetic resonance angiography with no strings attached: wireless active catheter visualization," *Magnetic Resonance in Medicine: Official Journal of the Society of Magnetic Resonance in Medicine / Society of Magnetic Resonance in Medicine*, vol. 53, pp. 446–455, Feb. 2005. PMID: 15678524.

[32] S. Weiss, T. Kuehne, F. Brinkert, G. Krombach, M. Katoh, T. Schaeffter, R. W. Guenther, and A. Buecker, "In vivo safe catheter visualization and slice tracking using an optically detunable resonant marker,"

Magnetic Resonance in Medicine: Official Journal of the Society of Magnetic Resonance in Medicine / Society of Magnetic Resonance in Medicine, vol. 52, pp. 860–868, Oct. 2004. PMID: 15389956.

[33] O. Unal, F. Korosec, R. Frayne, C. Strother, and C. Mistretta, "A rapid 2D time-resolved variable-rate k-space sampling MR technique for passive catheter tracking during endovascular procedures," *Magn Reson Med*, vol. 40, p. 356–62, Sept. 1998.

[34] O. Unal, J. Li, W. Cheng, H. Yu, and C. M. Strother, "MR-visible coatings for endovascular device visualization," *Journal of Magnetic Resonance Imaging: JMRI*, vol. 23, pp. 763–769, May 2006. PMID: 16555229.

[35] D. Rubin, A. Ratner, and S. Young, "Magnetic susceptibility effects and their application in the development of new ferromagnetic catheters for magnetic resonance imaging," *Invest Radiol*, vol. 25, p. 1325–32, Dec. 1990.

[36] V. Kochli, G. McKinnon, E. Hofmann, and G. von Schulthess, "Vascular interventions guided by ultrafast MR imaging: evaluation of different materials," *Magn Reson Med*, vol. 31, p. 309–14, Mar. 1994.

[37] C. Bakker, R. Hoogeveen, J. Weber, J. van Vaals, M. Viergever, and W. Mali, "Visualization of dedicated catheters using fast scanning techniques with potential for MR-guided vascular interventions," *Magn Reson Med*, vol. 36, p. 816–20, Dec. 1996.

[38] M. Miquel, S. Hegde, V. Muthurangu, B. Corcoran, S. Keevil, D. Hill, and R. Razavi, "Visualization and tracking of an inflatable balloon catheter using SSFP in a flow phantom and in the heart and great vessels of patients," *Magn Reson Med*, vol. 51, p. 988–95, May 2004.

[39] R. A. Omary, R. Frayne, O. Unal, T. Warner, F. R. Korosec, C. A. Mistretta, C. M. Strother, and T. M. Grist, "MR-guided angioplasty of renal artery stenosis in a pig model: a feasibility study," *Journal of Vascular and Interventional Radiology: JVIR*, vol. 11, pp. 373–381, Mar. 2000. PMID: 10735435.

[40] R. Mekle, E. Hofmann, K. Scheffler, and D. Bilecen, "A polymer-based MR-compatible guidewire: a study to explore new prospects for interventional peripheral magnetic resonance angiography (ipMRA)," *J Magn Reson Imaging*, vol. 23, p. 145–55, Feb. 2006.

[41] J. F. Schenck, "The role of magnetic susceptibility in magnetic resonance imaging: MRI magnetic compatibility of the first and second kinds," *Medical Physics*, vol. 23, pp. 815–850, June 1996. PMID: 8798169.

[42] C. J. Bakker, R. M. Hoogeveen, W. F. Hurtak, J. J. van Vaals, M. A. Viergever, and W. P. Mali, "MR-guided endovascular interventions: susceptibility-based catheter and near-real-time imaging technique," *Radiology*, vol. 202, no. 1, pp. 273–276, 1997. PMID: 8988223.

[43] L. W. Bartels, C. Bos, R. van Der Weide, H. F. Smits, C. J. Bakker, and M. A. Viergever, "Placement of an inferior vena cava filter in a pig guided by high-resolution MR fluoroscopy at 1.5 t," *Journal of Magnetic Resonance Imaging: JMRI*, vol. 12, pp. 599–605, Oct. 2000. PMID: 11042643.

[44] S. Kos, R. Huegli, E. Hofmann, H. H. Quick, H. Kuehl, S. Aker, G. M. Kaiser, P. J. Borm, A. L. Jacob, and D. Bilecen, "Feasibility of real-time magnetic resonance-guided angioplasty and stenting of renal arteries in vitro and in swine, using a new polyetheretherketone-based magnetic resonance-compatible guidewire," *Investigative Radiology*, vol. 44, pp. 234–241, Apr. 2009. PMID: 19252440.

[45] H. F. Smits, C. Bos, R. van der Weide, and C. J. Bakker, "Interventional MR: vascular applications," *European Radiology*, vol. 9, no. 8, pp. 1488–1495, 1999. PMID: 10525856.

[46] S. Kos, R. Huegli, E. Hofmann, H. Quick, H. Kuehl, S. Aker, G. Kaiser, P. Borm, A. Jacob, and D. Bilecen, "MR-compatible polyetheretherketone-based guide wire assisting MR-guided stenting of iliac and supraaortic arteries in swine: Feasibility study," *Minimally Invasive Therapy & Allied Technologies: MITAT: Official Journal of the Society for Minimally Invasive Therapy*, pp. 181–188, 2009. PMID: 19431070.

[47] S. Krueger, S. Schmitz, S. Weiss, D. Wirtz, M. Linssen, H. Schade, N. Kraemer, E. Spuentrup, G. Krombach, and A. Buecker, "An MR guidewire based on micropultruded fiber-reinforced material," *Magnetic Resonance in Medicine: Official Journal of the Society of Magnetic Resonance in Medicine / Society of Magnetic Resonance in Medicine*, vol. 60, pp. 1190–1196, Nov. 2008. PMID: 18958856.

[48] J. Reichenbach, R. Venkatesan, D. Yablonskiy, M. Thompson, S. Lai, and E. Haacke, "Theory and application of static field inhomogeneity effects in gradient-echo imaging," *J Magn Reson Imaging*, vol. 7, p. 266–79, Apr. 1997.

[49] R. van der Weide, K. J. Zuiderveld, C. J. Bakker, T. Hoogenboom, J. J. van Vaals, and M. A. Viergever, "Image guidance of endovascular interventions on a clinical MR scanner," *IEEE Transactions on Medical Imaging*, vol. 17, pp. 779–785, Oct. 1998. PMID: 9874302.

[50] J. Seppenwoolde, L. Bartels, R. van der Weide, J. Nijsen, A. van het Schip, and C. Bakker, "Fully MR-guided hepatic artery catheterization for selective drug delivery: a feasibility study in pigs," *J Magn Reson Imaging*, vol. 23, p. 123–9, Feb. 2006.

[51] M. Stuber, W. Gilson, M. Schar, D. Kedziorek, L. Hofmann, S. Shah, E. Vonken, J. Bulte, and D. Kraitchman, "Positive contrast visualization of iron oxide-labeled stem cells using inversion-recovery with ON-resonant water suppression (IRON)," *Magn Reson Med*, vol. 58, p. 1072–7, Nov. 2007.

[52] C. Cunningham, T. Arai, P. Yang, M. McConnell, J. Pauly, and S. Conolly, "Positive contrast magnetic resonance imaging of cells labeled with magnetic nanoparticles," *Magn Reson Med*, vol. 53, p. 999–1005, May 2005.

[53] J. Seppenwoolde, M. Viergever, and C. Bakker, "Passive tracking exploiting local signal conservation: the white marker phenomenon," *Magn Reson Med*, vol. 50, p. 784–90, Oct. 2003.

[54] E. Vonken, M. Schar, and M. Stuber, "Positive contrast visualization of nitinol devices using susceptibility gradient mapping," *Magn Reson Med*, vol. 60, p. 588–94, Sept. 2008.

[55] H. Dahnke, W. Liu, D. Herzka, J. Frank, and T. Schaeffter, "Susceptibility gradient mapping (SGM): a new postprocessing method for positive contrast generation applied to superparamagnetic iron oxide particle (SPIO)-labeled cells," *Magn Reson Med*, vol. 60, p. 595–603, Sept. 2008.

[56] J. Seppenwoolde, K. Vincken, and C. Bakker, "White-marker imaging-Separating magnetic susceptibility effects from partial volume effects," *Magn Reson Med*, July 2007.

[57] O. Bieri, S. Patil, H. Quick, and K. Scheffler, "Morphing steady-state free precession," *Magn Reson Med*, vol. 58, p. 1242–8, Dec. 2007.

[58] H. Y. Carr, "Steady-State free precession in nuclear magnetic resonance," *Phys. Rev.*, vol. 112, p. 1693–1701, Dec. 1958.

Chapter 2

Positive Contrast Imaging of the Paramagnetic Markers Using Spatial-Spectral Excitation Pulse

This chapter has been partially presented as:
S. Patil, C. Boller, D. Bilecen, K. Scheffler, "Visualization of the paramagnetic markers in interventional MRI using spatial-spectral pulses", Proceedings of 15th joint annual meeting ISMRM-ESMRMB, Berlin,Germany, pp. 1122, 2007.

2.1 Introduction

The paramagnetic markers or materials cause significant field inhomogeneities when placed in a uniform main magnetic field B_0, due to its local susceptibility differences with respect to surrounding tissues. In many cases, these inhomogeneities result in undesired imaging effect, known as susceptibility artifacts. Nevertheless this source of field inhomogeneity has been exploited as a form of image contrast for passive visualization and tracking of the interventional devices (catheters and guidewires) [1, 2] and for super-paramagnetic iron oxide (SPIO)-labeled cells [3]. Traditionally the visualization of these paramagnetic materials is based on increase in T_2^* decay that they cause entailing a negative contrast (signal loss) with respect to background in a resultant image. Unfortunately, due to confounding background signals it is often difficult to distinguish signal loss due to paramagnetic materials from other unwanted inhomogeneities such as, air/tissue interfaces etc.

Therefore, MRI techniques that generate positive contrast that are localized within the immediate surroundings of the paramagnetic materials have been proposed [4–6]. The state-of-the-art positive contrast techniques can be broadly classified into three categories based upon their method of identifying paramagnetic materials: those using local frequency shifts in the on-resonance frequency [6–8], those exploiting the local gradient compensation by the imaging gradients [4, 5] and those mapping the susceptibility-induced gradients as a post-processing step [9].

In one of the method that exploits local frequency shifts to create positive contrast uses specially designed RF pulses to spectrally excite the off-resonant water protons within the close vicinity of the paramagnetic marker with a reported theoretical background suppression of approximately 120 dB [8]. However, clear limitation of this technique is the use of temporally inefficient spin-echo type of sequences and requires special knowledge of RF designing. Another method, known as inversion recovery with ON-resonant water suppression (IRON) method [7] selectively saturates the background on-resonant water protons and leaving off-resonant water protons available for excitation during normal imaging experiment. In IRON method, on-resonant spectrally suppressive pulse is applied only at the start of the 2D or 3D imaging and may potentially lead to recovery of on-resonant water protons thereby decreasing background suppression.

In order to overcome these disadvantages, we propose a new off-resonance excitation-based positive contrast method for passive tracking of interventional devices, where fast detection of marker is desirable. In this work, binomial spatial-spectral excitation pulse (SPSP pulse) was incorporated into a fast SSFP-echo (reversed fast imaging with steady-state precession [PSIF], T_2-fast field echo [T_2-FFE], contrast-enhanced Fourier-acquired steady-state [CE-FAST]) type of sequence to generate positive contrast due to para-

magnetic materials on its immediate surrounding. In this chapter, firstly the local frequency shifts induced by paramagnetic marker materials are elucidated, followed by principle of off-resonance excitation of tissues using SPSP pulse is explained theoretically. Next, the in-vitro experiments demonstrate the proper localization and feasibility of paramagnetic marker detection mounted on the interventional guidewire tip. The signal and localization characteristics of the SPSP pulse are analyzed theoretically and verified experimentally.

2.2 Theory

2.2.1 Local Frequency Shifts

A small point-like paramagnetic marker material wrapped around a guide wire (for example, as shown in Fig. 2.1a) induces a field perturbation (in SI units)

$$\Delta B_z(x,y,z) = \frac{B_0 \Delta\chi V}{4\pi} \cdot \frac{x^2+y^2-2z^2}{(x^2+y^2+z^2)^{5/2}} \tag{2.1}$$

of dipolar form in the main magnetic field B_0 [4]. Here, V is the volume of the paramagnetic material, $\Delta\chi$ is the susceptibility difference between the marker material and the surrounding tissues and $\Delta\chi V$ (m^3) characterizes the local magnetic dose (LMD). Simulated ΔB_z values for a given LMD at B_0=1.5 T are shown in Fig. 2.1b using the iso-value of $\pm$500 Hz. Thus the given paramagnetic material causes the frequency shifts of $\pm$500 Hz away from the on-resonance frequency (in this case: 63.6 MHz) within its immediate surrounding tissues at approximate distances of 1 cm. In the following, spatial-spectral RF pulses (SPSP pulses) that selectively excite a shell of these off-resonant tissues at spatial location z are described.

2.2.2 Spatial-Spectral RF Pulses

The SPSP pulse consists of series of n slice selective RF subpulses with tip angles α_i (where i=1 to n) and a τ seconds delay between the two adjacent subpulses applied in conjunction with an oscillating slice select gradient [10]. Figure. 2.2a shows the SPSP pulse with $n = 4$ subpulses that are applied during the positive lobes of an oscillating slice-select gradient. Each subpulse selects the slice at location z, whereas the phase accumulation from one subpulse to the next along the train selects the spectral frequency. The spectral response of this SPSP pulse is governed by n-point Finite Impulse Response (FIR) filter, which is periodic, with a period of $1/\tau$ Hz [11, 12]. The most popularly used FIR filter for this purpose is a binomial filter. So far the SPSP pulse has been used to selectively excite the water or to selectively saturate the fat exploiting the chemical shift between the water and fat [10].

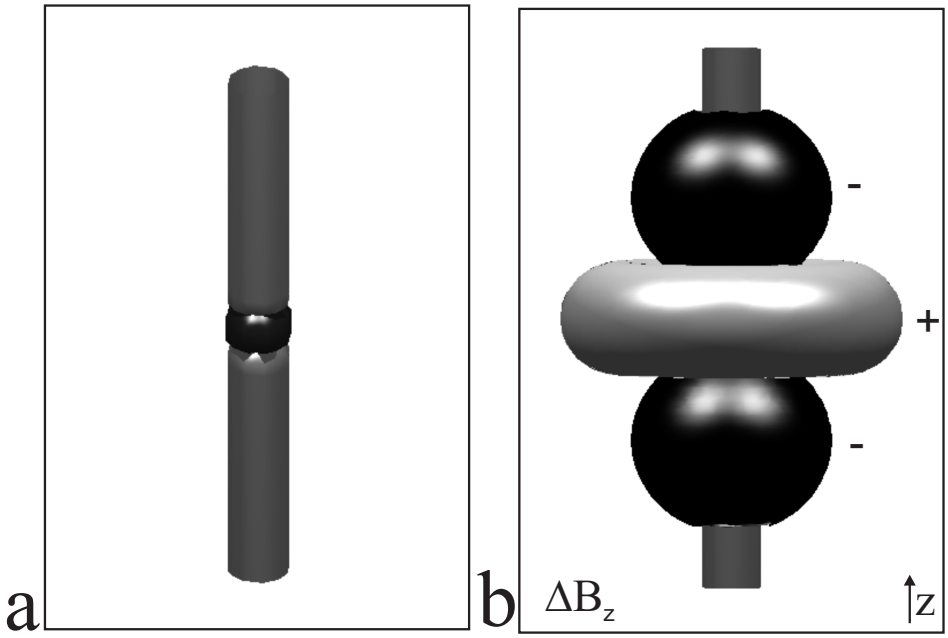

Figure 2.1: a) Simulated guidewire with paramagnetic ring (black spot) mounted on it b) The local frequency shifts within the close vicinity of the guidewire induced due to paramagnetic marker material for a given local magnetic dose at 1.5 T using the iso-value of ±500 Hz.

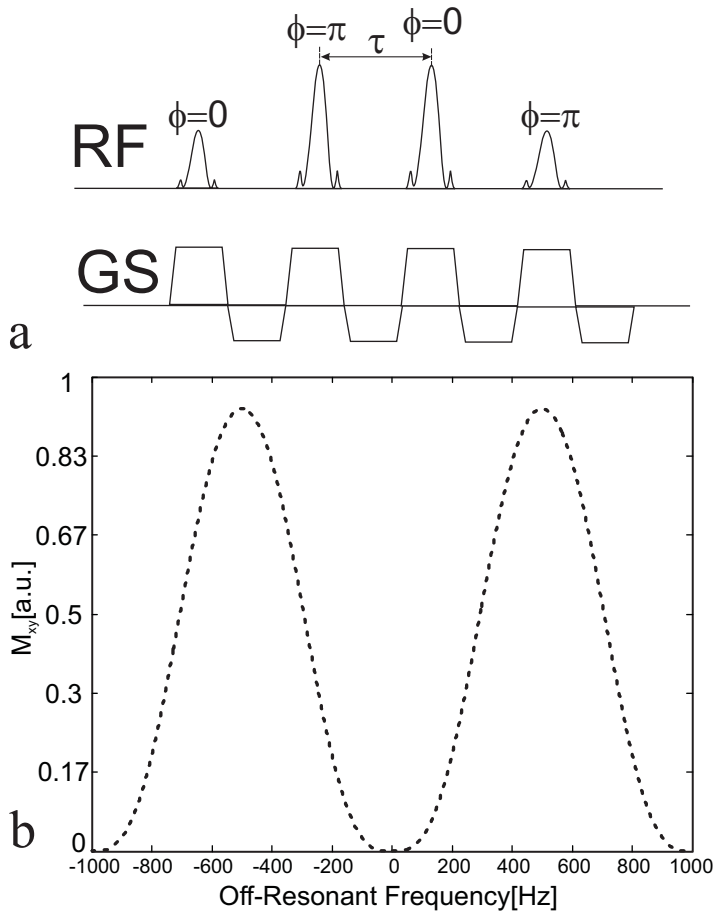

Figure 2.2: a) A spatial-spectral excitation pulse for $N = 4$ subpulses applied in conjunction with mono-polar slice select gradients. b) The spectral response of the SPSP excitation pulse shown in a, obtained by setting the center excitation frequency to water and adding a phase difference of π between two adjacent subpulses and $\tau = 1$ ms. The periodicity of spectral response ensures that both positive and negative lobes (see Fig. 1b) of the off-resonant tissues within the close vicinity of the marker are excited.

In this work, the SPSP pulse is used to selectively excite the off-resonant tissues (see Fig. 2.1b) within the immediate surrounding of the paramagnetic marker only, within the selected slice. If we want to excite these off-resonant tissues without touching water then we must ensure that: $1/\tau \geq 2B_0\gamma\Delta\chi$ with γ being gyromagnetic ratio of water protons. In the present case, the center frequency of excitation of SPSP pulse is set on water resonance and a phase of π radians is added between the two adjacent subpulses, which shifts the frequency response by $\Delta f = 500$ Hz, when the separation between two spectral lobes is 1 kHz (τ=1 ms). The simulated off-resonance frequency response of the SPSP pulse for binomial filter of order three is shown (dotted) in Fig. 2.2b. Due to periodicity of the spectral response, both positive and negative lobes (see Fig. 1b) of the off-resonant tissues are excited. It can be also noticed that, because of relatively broader bandwidth, fat with a chemical-shift difference of 3.4 ppm (approximately 217 Hz at 1.5 T) also excited. The incorporation of SPSP pulse in a SSFP type of sequence, its signal characteristics and its application for passive tracking of interventional guidewire is a part of present study and is illustrated in the following sections.

2.3 Materials And Methods

Phantom measurements and calibrations were performed on a Siemens 1.5 T Espree system (Siemens Healthcare, Erlangen, Germany) employing maximum gradient strength of 33 mT/m and a slew rate of 170 mT/(m×ms). Imaging was done using integrated spine coils and body phased array coils. All images were acquired using coronal orientation with readout applied along the main magnetic field. A matrix of 128×128 covering an FOV of 300 mm was used with slice thickness of 40 mm. The maximum available bandwidth/pixel for a given TR was utilized. No averages were taken for any of the images displayed. Numerical simulations, data analysis and visualization were done using Matlab 2006a (The MathWorks, Inc.).

2.3.1 In Vitro Experiments

An MR-compatible guidewire made up of Polyetherethertone synthetic polymer core with a diameter of 0.7 mm and compatible with $0.035''$ catheter was used. The paramagnetic material made up of stainless steel alloy was wrapped around the guidewire near its tip with approximate dimensions 1mm in height and diameter. Frequency measurements yield an LMD of $\Delta\chi V = 1 \times 10^{-11}\ m^3$ (in SI units). The guidewire was inserted into a custom-built phantom with 16 mm diameter tubes to model the blood flow, positioning and tracking of the guidewire in large vessels. The tubes were immersed in a gadolinium (Gd)-doped water and were surrounded by a 2%

agarose gel (v/v) doped with 0.5 mM copper sulphate ($CuSO_4$) concentration to closely resemble the relaxation times of muscle tissues for which T_1=900 ms and T_2=50 ms. A 7F introducer sheath was attached to the tubes to facilitate the introduction and manipulation of the guidewire within the tubes.

2.3.2 Imaging Experiments

The excitation scheme of standard SSFP-echo type of sequence was modified to incorporate the SPSP excitation pulse ($n = 4$) shown in Fig. 2.3. To obtain a positive contrast image the center frequency of excitation of SPSP pulse was set 500 Hz (Δf) away from the water resonance. The values of n and Δf were chosen empirically for the current paramagnetic marker. It can be perceived that either SSFP-echo or SSFP-FID might be equally suited as a template for SPSP pulse. However, empirically SSFP-echo was found to be better than SSFP-FID in terms of contrast-to-noise (CNR) ratio performance. In addition, selective adiabatic short tau inversion recovery (STIR) pre-pulse [13, 14] was applied to achieve efficient fat suppression. In order to reduce the inversion time (TI) between inversion recovery pulse and the image acquisition, centric reordering scheme was employed.

2.3.3 Signal Characteristics of the SPSP pulse

For SPSP pulse, a change in the off-resonance excitation frequency (Δf) as well as the number of RF sub-pulses in it expected to have an effect on localization characteristics as well as positive contrast generation. Hence, in order to analyze the positive contrast properties of the SPSP pulse, Δf was varied from 200 Hz to 900 Hz away from the water resonance and number of RF sub-pulses within the composite SPSP pulse was varied from 2 to 10. A theoretical simulation was performed to calculate the normalized bandwidth of FIR filter for varying number of filter taps from 2 to 10.

2.4 Results

In this section, we describe the results obtained using flow phantom and MR-compatible interventional guidewire (See Materials and Methods). Next, we provide description of the off-resonant frequency dependent localization characteristics of the SPSP pulse. This is followed by analysis of volume of positive contrast signal as a function of RF pulse count within the SPSP pulse.

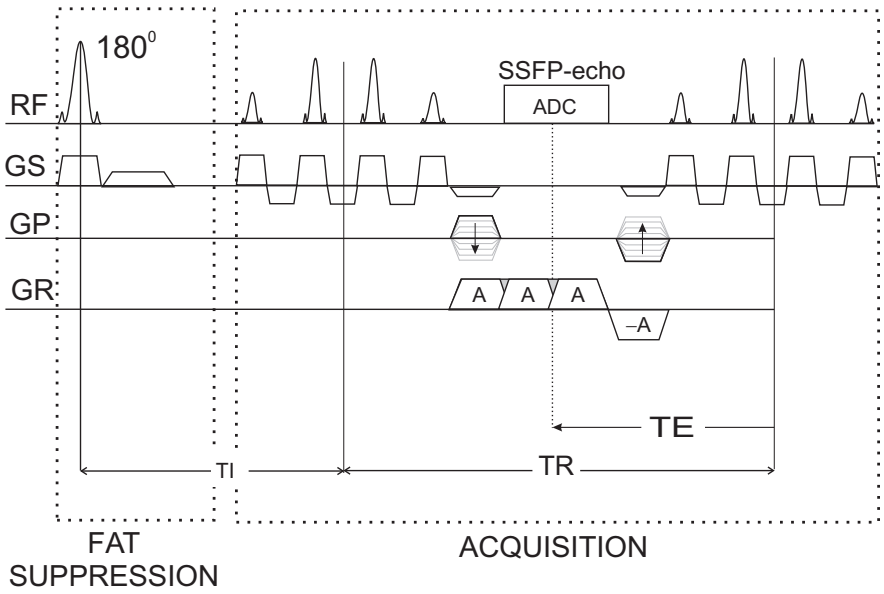

Figure 2.3: Pulse Sequence diagram of the SPSP SSFP-echo sequence. The excitation scheme of the standard SSFP-echo sequence was modified to incorporate SPSP composite pulse ($n = 4$). To obtain a positive contrast image the center frequency of excitation of SPSP pulse was set 500 Hz (Δf) away from the water resonance. To suppress concomitant fat signal selective adiabatic short tau inversion recovery pulse (180^0) was applied before the actual positive contrast image acquisition. TI was kept to minimum by employing centric reordering scheme

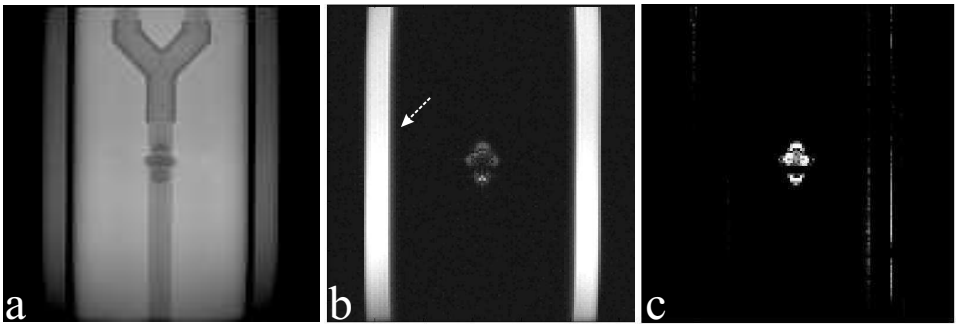

Figure 2.4: In-vitro Phantom Images. a) An Experimental phantom image in the coronal direction using SSFP-echo sequence showing the flow tubes and signal void (white arrow) resembling dipolar form due to local magnetic field perturbations induced by paramagnetic marker material wrapped around guidewire. (The imaging parameters were α=70^0, TR=4.14 ms, slice thickness=40 mm, matrix 128×128) b) By using SPSP pulse in the SSFP-echo sequence to selectively excite only off-resonant protons within the immediate surrounding of paramagnetic marker a positive contrast is obtained. Similar imaging parameters as that of localizer image were used except TR was increased to 7.74 ms, due to SPSP pulse. However, concomitant fat excitation contaminates the background signal suppression (dotted white arrow) c) By additionally playing out STIR pulse, excellent fat suppression is obtained while retaining positive contrast within the close vicinity of the marker.

2.4.1 In-Vitro Imaging

The results of proof-of-principle experiments in a flow phantom are depicted in Fig. 2.4a. The SSFP-echo coronal image using moderately short TR and flip angle (TR= 4 ms and $\alpha = 70^0$, slice thickness=40 mm, matrix 128×128)) shows the flow tubes and hypo-intense signal (white arrow) due to local frequency shifts induced by the paramagnetic marker within its immediate vicinity thereby identifying the tip of the guidewire. In contrast, using the SPSP pulse in SSFP-echo sequence that selectively excites off-resonant tissues within close vicinity of the paramagnetic marker, four hyper-intense lobes are observed in Fig. 2.4b surrounding the paramagnetic marker and thus localizing the guidewire tip. Similar imaging parameters as that of localizer image were used except TR was increased to 7.74 ms, due to SPSP pulse. Although background signal is heavily suppressed, concomitant fat signal appears bright near the edges of the phantom (see, dotted white arrow). As shown in Fig. 2.4c, by additionally playing out STIR pre-pulse, the concomitant fat signal is completely suppressed whereas the positive signal in the area of paramagnetic tip is preserved. Thereby further enhancing the CNR ratio of the hyper-intense region with respect to background.

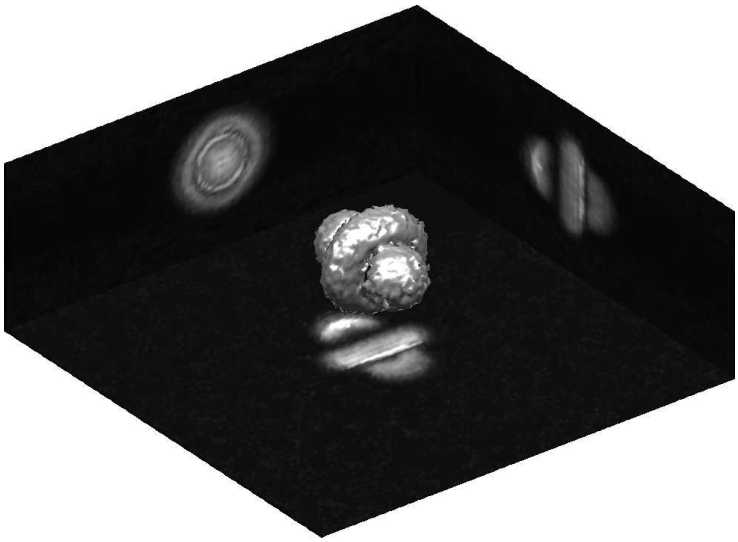

Figure 2.5: The 3D hyper-surface rendering of the hyper-intense signal obtained from a 3D dataset using off-resonant SPSP pulse and covering a slab thickness of 60 mm. The other imaging parameters were α=70^0, TR= 8.18 ms, slice thickness= 1 mm. Mean signal intensity projections are also shown along three directions and are consistent with the 2D measurements.

Figure 2.5 shows the rendered hyper-surface from hyper-intense signal intensities generated from a 3D dataset obtained using series of coronal images with SPSP pulse at Δf = 500 Hz. The other imaging parameters were: slab thickness=60 mm, α=70^0, TR= 8.18 ms, slice thickness= 1 mm. The rendered hyper-surface forms a shell of excited off-resonant protons exhibiting dipole-like structure. Mean signal intensity projections are also shown along three directions and are consistent with the 2D measurements (see Fig. 2.4b and Fig. 2.4c).

2.4.2 Off-resonant Excitation Frequency Dependence

The dependence of off-resonant excitation frequency (Δf) on the localization characteristics of the positive contrast region is demonstrated in Fig. 2.6. The distance (d) between the two of the hyper-intense lobes was plotted against the Δf varying from 200 to 900 Hz. The calculation of d is shown on the adjacent image insets. A linear fit of the data yielded a slope of 0.34.

2.4.3 RF Pulse Count Dependence

In Figure 2.7 simulated normalized bandwidth of the binomial filter with increasing number of filter taps, which are equivalent to number of RF pulses

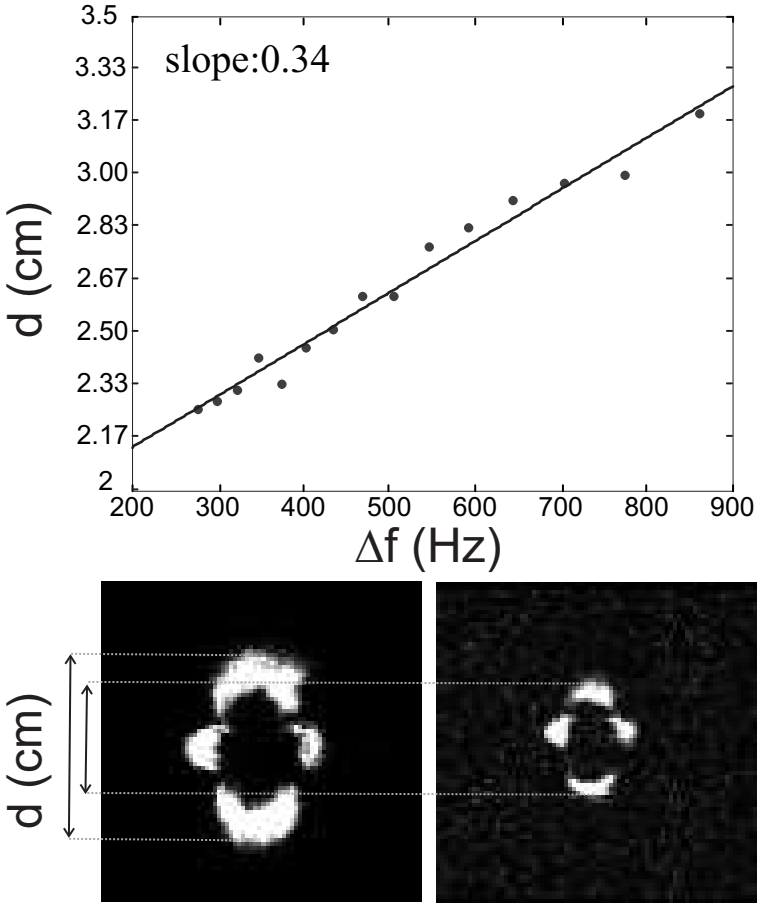

Figure 2.6: Localization characteristics of the SPSP pulse. a) Plot of the distance (d) between the two hyper-intense blobs insets against the off-resonance excitation frequency varying in the range [200-900]. Calculation of the d is shown in the adjacent image insets. The slope of the fitted line was 0.34 close to theoretical prediction of 0.33.

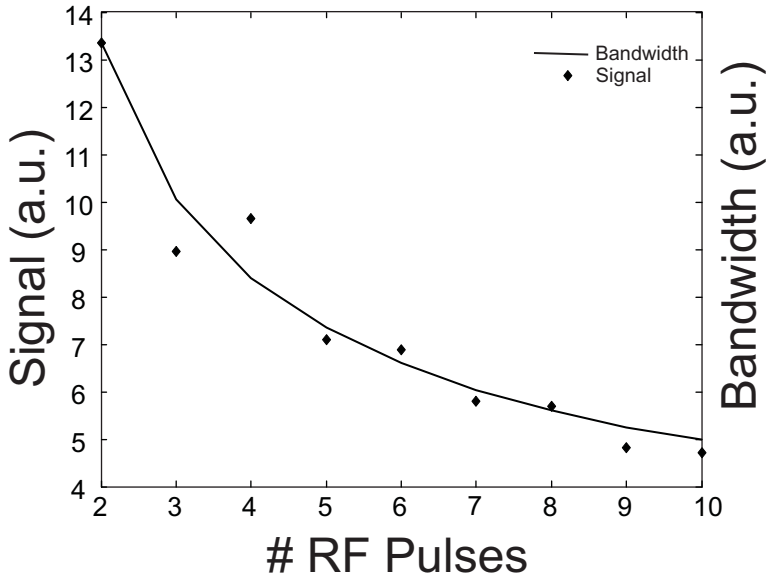

Figure 2.7: Simulated normalized bandwidth of the binomial filter with increasing number of filter taps, which are equivalent to number of RF pulses in SPSP pulse is plotted. Volume of the positive contrast signal is also plotted against the number of RF pulses and correlates well with the variation in bandwidth.

in SPSP pulse is plotted and is shown as a line. In addition, the volume of the generated positive contrast signal was plotted (diamond heads) against the number of RF pulses. It can be clearly seen that both plot correlates well with each other.

2.5 Discussion

In this work, positive contrast imaging of the interventional guidewire with paramagnetic marker mounted on it using SPSP off-resonant excitation pulse was demonstrated successfully in a flow phantom. The SPSP pulse selectively excites the spatially dependent spectral components surrounding the paramagnetic marker without touching the water protons in the background. It can also be noted that due to periodicity of the spectral response of the SPSP pulse (see Fig. 2.2b, both positive and negative lobes of the local frequency shifts appears with positive contrast (see Fig. 2.4a and b) consistent with theoretical predictions. However, spectral component of fatty tissues also fall within the excitation bandwidth of SPSP pulse and appear with positive contrast as well thereby contaminating the background suppression. Thus the additional STIR pre-pulse exploiting T_1 effect of the fat was needed to efficiently suppress unwanted signal arising from fatty tissues.

The SPSP excitation pulse excites a shell of off-resonant protons forming a dipole-like structure, which is evident from rendered hyper-surface in Fig. 2.5 and is consistent with theoretical simulations shown in Fig 2.1b.

From Eq. 2.1 we can infer that the local frequency offsets (ΔB_z) are spatially dependent and are directly proportional to its distance from the paramagnetic marker i.e., $\Delta B_z \propto r^{-3}$ (Eq. 2.1, distance r). Therefore the localization of positive contrast region using SPSP RF pulses can also be expected to scale with off-resonant excitation frequency ($\Delta f \propto r^{-3}$). To this end, the slope of the line plotting these power functions should be equal to their power value i.e., 0.33. Measurements shown in Fig. 2.6 yield a slope value of 0.34 and correlate well with the theoretical predictions. The proximity of the positive contrast region to the marker may thus be controlled by using Δf to a lower value for this paramagnetic marker. This may however, lead to excitation of nearby on-resonant water protons (see Fig. 2.2b) thereby contaminating efficient background suppression. Hence, a good compromise for Δf dependent on size of marker material needs to be obtained.

It is well-known that the bandwidth of n-point FIR scales with the increase in filter taps (number of filter points), although not necessarily in a linear manner [11]. Since SPSP composite pulse also consists of series of RF pulses, its spectral response is governed by number of RF pulses containing in it. Thus the volume of the positive contrast region (region of excited off-resonance frequencies) is also expected to scale with the number of RF pulses used in SPSP pulse. This is clearly evident from Fig. 2.7 in which theoretical predictions (normalized bandwidth) and experimentally measured values (volume of positive contrast) are in good agreement with each other. The effectiveness of the background suppression and thus the CNR of the positive contrast could effectively be controlled by increasing the number of RF pulses. However, this may also lead to increase in TR and thereby losing the signal as SSFP-echo signal decreases with increase in TR.

Based on similar findings of others [7, 8], further potential application of SPSP pulse includes the positive contrast visualization and tracking of SPIO-labeled cells.

The other sources of B_0 inhomogeneities such as air-tissue interfaces may also inevitably lead to positive contrast thereby causing unnecessary background signal contamination. However, by using volumetric shimming this contamination can be minimized as indicated previously [7]. Due to composite SPSP pulse TR of SSFP-echo sequence increases considerably thereby partially losing the temporal efficiency. In spite of this, by using additional means of acceleration techniques such as parallel imaging, passive tracking of interventional guidewire can be done at sufficient temporal and spatial resolution. Another considerable limitation of the proposed method is additional use of STIR pre-pulse. Yet another way of suppressing the signal

from fatty tissues is based on its chemical shift effect [15]. However, this approach may irreversibly compete with the proposed SPSP pulse approach and may hamper the positive contrast enhancement. Although the positive contrast generation using SPSP pulse for paramagnetic marker was successfully demonstrated in a flow phantom, its performance in in-vivo studies still needs to be explored.

2.6 Conclusion

In this work, a new concept of positive contrast imaging within the close vicinity of the paramagnetic marker was presented and its use to visualize interventional guidewire tip was demonstrated. The SPSP pulse, which is both spatially as well as spectrally selective, was used to excite off-resonant tissues within the immediate surrounding of the paramagnetic marker to generate positive contrast. By additionally playing out STIR pre-pulse efficient fat suppression was achieved, whilst retaining the positive contrast. The proximity of the positive contrast to the marker tip was dependent on off-resonance excitation frequency of the SPSP pulse, whereas volume of the positive contrast was dependent on the number of RF sub-pulses within the SPSP pulse.

References

[1] D. Rubin, A. Ratner, and S. Young, "Magnetic susceptibility effects and their application in the development of new ferromagnetic catheters for magnetic resonance imaging," *Invest Radiol*, vol. 25, p. 1325–32, Dec. 1990.

[2] C. Bakker, R. Hoogeveen, J. Weber, J. van Vaals, M. Viergever, and W. Mali, "Visualization of dedicated catheters using fast scanning techniques with potential for MR-guided vascular interventions," *Magn Reson Med*, vol. 36, p. 816–20, Dec. 1996.

[3] M. H. M. Dias and P. C. Lauterbur, "Ferromagnetic particles as contrast agents for magnetic resonance imaging of liver and spleen," *Magnetic Resonance in Medicine: Official Journal of the Society of Magnetic Resonance in Medicine / Society of Magnetic Resonance in Medicine*, vol. 3, pp. 328–330, Apr. 1986. PMID: 3713497.

[4] J. Seppenwoolde, M. Viergever, and C. Bakker, "Passive tracking exploiting local signal conservation: the white marker phenomenon," *Magn Reson Med*, vol. 50, p. 784–90, Oct. 2003.

[5] O. Bieri, S. Patil, H. Quick, and K. Scheffler, "Morphing steady-state free precession," *Magn Reson Med*, vol. 58, p. 1242–8, Dec. 2007.

[6] R. Mekle, E. Hofmann, K. Scheffler, and D. Bilecen, "A polymer-based MR-compatible guidewire: a study to explore new prospects for interventional peripheral magnetic resonance angiography (ipMRA)," *J Magn Reson Imaging*, vol. 23, p. 145–55, Feb. 2006.

[7] M. Stuber, W. Gilson, M. Schar, D. Kedziorek, L. Hofmann, S. Shah, E. Vonken, J. Bulte, and D. Kraitchman, "Positive contrast visualization of iron oxide-labeled stem cells using inversion-recovery with ON-resonant water suppression (IRON)," *Magn Reson Med*, vol. 58, p. 1072–7, Nov. 2007.

[8] C. Cunningham, T. Arai, P. Yang, M. McConnell, J. Pauly, and S. Conolly, "Positive contrast magnetic resonance imaging of cells labeled with magnetic nanoparticles," *Magn Reson Med*, vol. 53, p. 999–1005, May 2005.

[9] E. Vonken, M. Schar, and M. Stuber, "Positive contrast visualization of nitinol devices using susceptibility gradient mapping," *Magn Reson Med*, vol. 60, p. 588–94, Sept. 2008.

[10] Y. Zur, "Design of improved spectral-spatial pulses for routine clinical use," *Magn Reson Med*, vol. 43, p. 410–20, Mar. 2000.

[11] J. Proakis and D. Manolakis, *Digital Signal Processing (4th Edition)*. Prentice Hall, Mar. 2006.

[12] A. Oppenheim, R. Schafer, and J. Buck, *Discrete-Time Signal Processing (2nd Edition)*. Prentice Hall, Feb. 1999.

[13] G. Bydder, R. Steiner, L. Blumgart, S. Khenia, and I. Young, "MR imaging of the liver using short TI inversion recovery sequences," *J Comput Assist Tomogr*, vol. 9, p. 1084–9, Dec. 1985.

[14] G. Bydder and I. Young, "MR imaging: clinical use of the inversion recovery sequence," *J Comput Assist Tomogr*, vol. 9, p. 659–75, Aug. 1985.

[15] A. Haase, J. Frahm, W. Hänicke, and D. Matthaei, "1H NMR chemical shift selective (CHESS) imaging," *Physics in Medicine and Biology*, vol. 30, p. 341–344, Apr. 1985. PMID: 4001160.

Chapter 3

Echo-dephased Steady State Free Precession

Major part of this chapter has been published as:
S. Patil, O. Bieri, and K. Scheffler, "Echo-dephased steady state free precession", Magma (New York, N.Y.), May 2009. PMID: 19449047

3.1 Introduction

Magnetic field inhomogeneities, for example as generated by susceptibility differences, have a strong impact on signal properties of gradient-echo sequences [1]. It is well known that strong field inhomogeneities appear as black voids (signal loss) in a typical GRE image entailing a negative contrast with respect to background signal. On the other hand, positive contrast from local susceptibility changes was first proposed by Frahm et al [2] using local gradient compensation. Positive contrast, also known as white marker imaging has found application in interventional MRI for passive depiction and tracking of the interventional devices [3] or to visualize magnetically labeled cells [4]. Generally a gradient in slice direction is used to dephase background signals, whereas marker-related local gradients compensate for the dephasing to produce locally a positive contrast. One of the major prerequisites for successful passive tracking is the feasibility of image acquisitions with extended slab thickness (40–50 mm) to guarantee that the marker material always lies within the plane being imaged. However, application of dephasing gradients using extended slice thickness may also enhance other unwanted background signals, e.g. from air/tissue interfaces and thereby hampering proper marker localization and visualization. Sequence developments that further reduce background sensitivity are thus desirable and only recently a promising concept for the generation of positive contrast from local susceptibilities was proposed which is based on morphing of steady-state free precession (SSFP) [5].

In this chapter, we further develop the idea of gradient compensation in SSFP to locally induce high signal intensities. In the close vicinity of paramagnetic materials, strong local gradient fields may compensate for any sequence-related gradients to locally induce signal transitions from an echo-dephased to an echo-rephased type of SSFP (mainly balanced SSFP (bSSFP)) sequence. Generically resembling an unbalanced SSFP, in echo-dephased SSFP echoes are preferably dephased by $\pm\pi$ prior to readout. This not only ensures excellent cancellation of any background signals but also generic dephasing from unbalanced SSFP greatly reduces unwanted background signal enhancements. It will be demonstrated that due to the higher in-plane resolution as compared to slice resolution, local gradient compensation in echo-dephased SSFP is likely to take place only within the close vicinity of the paramagnetic marker material. Conceptual issues of gradient compensation and its signal properties are analyzed and discussed. To demonstrate the feasibility of proper marker visualization and localization using echo-dephased SSFP, reliable tracking of MR compatible interventional guidewire having paramagnetic material on it is demonstrated in a simple flow phantom. The utility of the echo-dephased SSFP is also shown for positive contrast visualization of human pancreatic islets labeled with superparamagnetic iron oxide (SPIO) contrast agent in vitro. Finally in

vivo experiments in a rat model demonstrates the robust and reliable visualization of transplanted SPIO-labeled pancreatic islets in a rat chamber.

3.2 Materials and Methods

In order to illustrate the conceptual issues of echo-dephased SSFP, numerical simulations, data analysis and visualization were done using Matlab 2006a (The MathWorks, Inc.). Flow phantom measurements and calibrations were performed on a Siemens 1.5 T Espree system (Siemens Healthcare, Erlangen, Germany), whereas the human islet cell visualization in a phantom and in vivo rat studies were done on a Siemens 3 T Trio system. Unless otherwise stated, images were acquired in the coronal direction with readout and dephasing gradients applied along the main magnetic field. A matrix of 256×256 covering a FOV of 200 mm was used with a slice thickness of 40 mm. The maximum available bandwidth/pixel for a given TR was utilized.

3.2.1 Local Gradient Field Effect

A small paramagnetic material (for example, stainless steel) induces spatially dependent local gradient perturbations (ΔG) derived from the partial derivatives of the field offsets (ΔB_z) according to [3]

$$\begin{aligned} \Delta G_z &= -3cz\tfrac{-3x^2-3y^2+2z^2}{(x^2+y^2+z^2)^{7/2}}; \\ \Delta G_x &= -3cx\tfrac{x^2+y^2-4z^2}{(x^2+y^2+z^2)^{7/2}} \end{aligned} \tag{3.1}$$

with $c = \frac{B_0 \cdot \Delta\chi \cdot V}{4\pi}$, B_0 is the main magnetic field, $\Delta\chi$ is the susceptibility difference between the marker material and the surrounding tissues and $\Delta\chi V$ (m^3) characterizes the local magnetic dose (LMD) [6]. The ΔG_y shows similar spatial dependence as that of ΔG_x due to radial symmetry of the ΔB_z.

Depending upon the direction of the slice orientation one of these field perturbations may compensate for imaging related dephasing gradients. For example, if the slice orientation is along coronal direction, ΔG_z may act as a compensating gradient for any gradient applied along the main magnetic field. In the following, we will further develop the idea of compensation of echo-dephasing gradients in SSFP.

3.2.2 Echo-dephased SSFP

Generally within any repetition time the phase evolution ϕ_G of an isochromat at position $r(x, y, z)$ in the presence of a gradient G is given by [7]

$$\phi_G = \gamma \int_0^{TR} G(t) \cdot r dt, \tag{3.2}$$

For SSFP, the dispersion of phase evolution ϕ_G within one voxel is constant and is equal to either 2π (SSFP-FID or SSFP-ECHO [8]) or zero (bSSFP). In echo-dephased SSFP (shown in Fig. 3.1a) the net phase dispersion ϕ_G, is preferably set equal to 4π/voxel. This is achieved by modifying balanced gradient pattern of the bSSFP sequence along the readout direction. The pre-phasing gradient present before the readout as well as rephasing gradient present after the readout gradient have the same polarity as that of readout gradient. Thus there is no refocusing of the readout gradient. This global behavior of the echo-dephased SSFP ensures that none of the transversal states from background tissues contribute to the echo formation.

In the presence of the local gradients, ΔG, due to the marker at position $r_0(x_0, y_0, z_0)$ the amount of dephasing modifies to

$$\begin{aligned} \phi_G \rightarrow \phi_G &= \gamma \int_0^{TR} [G(t) \cdot r + \Delta G \cdot (r - r_0)] dt \\ &= \gamma \int_0^{TR} G(t) \cdot r \cdot dt + \gamma \cdot TR \cdot \Delta G \cdot (r - r_0). \end{aligned} \tag{3.3}$$

As a result, different fractional compensation leads to different signal properties of echo-dephased SSFP (Fig. 3.1b): At certain distance (indicated as (1) in Fig. 3.1b), ΔG fully compensates the sequence related intrinsic dephasing ($|\phi_G| = 0$) to form a bSSFP type of echo similar to the morphing SSFP concept [5]. With increasing distances, gradient compensation further decreases to yield a dephasing of $|\phi_G| = 2\pi$ /voxel (at some specific position (2) in Fig. 3.1b). Here, the echo is a summation of different dephasing paths within the voxel. ΔG tends to zero for $r >> r_0$, leading to $|\phi_G| = 4\pi$ /voxel as shown in Fig. 3.1a and indicated as position (3) in Fig. 3.1b. Thus in this region no compensation of the sequence-related dephasing takes place. For a uniform distribution of different dephasing angles p(ϕ_G) and in the presence of various off-resonances ϕ_0 the steady-state signal $S(t = TE)$ is given by [7]:

$$S(TE) \propto \int p(\phi_G) \cdot M_+(\phi_G + \phi_0) \cdot e^{-TE/T_2} \cdot e^{i \cdot (\phi + \phi_0) \cdot TE/TR} d\phi \tag{3.4}$$

Here $M_+(\phi)$ is the transverse magnetization after the excitation pulse and is given by,

$$M_+(\phi) := M_y + iM_x = M_0 \cdot \sin(\alpha) \cdot \frac{(1 - E_1)(1 - E_2 e^{-i\phi})}{C \cdot \cos(\phi) + D}, \tag{3.5}$$

$$\text{where} E_{1,2} := e^{-TR/T_{1,2}}$$

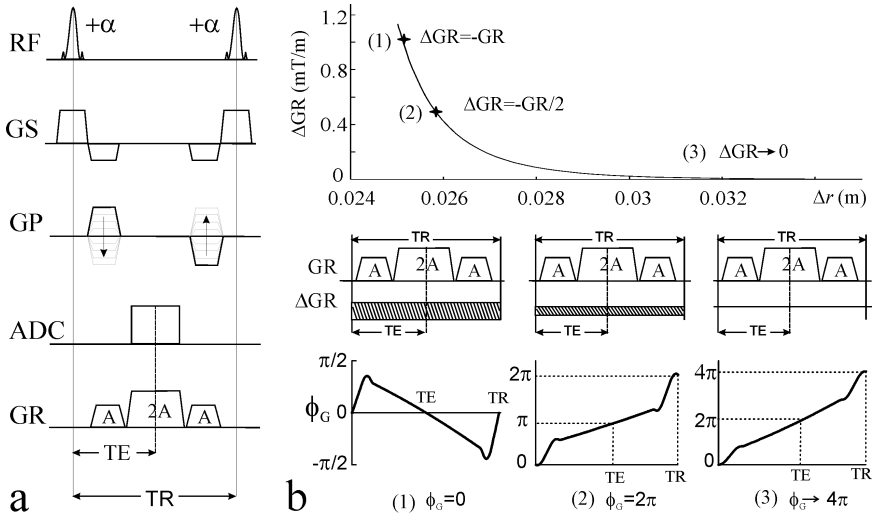

Figure 3.1: The working principle of echo-dephased SSFP. a) Sequence diagram. Echo-dephased SSFP dephases spins by 4π/voxel along the readout direction (total area: 4A). This ensures complete suppression of the background. b) The signal behavior at TE=TR in the presence of local gradient fields (ΔG), e.g. as induced by the paramagnetic ring marker. At certain spatial locations (1, 2, 3), ΔG may fully, partially or not compensate the sequence-related dephasing gradient to form different types of SSFP echo: At (1): balanced SSFP (ΔG may fully compensate an amount equal to G), at (2): averaged balanced SSFP (at location further away from marker, ΔG may compensate an amount equal to G/2) and at (3): echo-dephased SSFP (with further increase in the distance away from the marker, the sequence may exhibit global behavior shown in Fig. 3.1a).

and

$$\begin{aligned} C: &= E_2(E_1-1)(1+\cos(\alpha)), \\ D: &= (1-E_1\cos(\alpha)) - (E_1-\cos(\alpha))E_2^2 \end{aligned} \tag{3.6}$$

In order to guide the development of echo-dephased SSFP, simulations of $S(TE)$ using Eq. 3.4 were performed at different TE values resembling the well-known SSFP sequences namely SSFP-FID ($TE = 0$), bSSFP ($TE = TR/2$) and SSFP-ECHO ($TE = TR$) as a function of fractional gradient compensation (ϕ_G) varying in the range of $[-4\pi : 4\pi]$ and off-resonance (ϕ_0 varying from -540 Hz to 540 Hz. The other imaging parameters used for simulations were: TR=3 ms, $T_1 = 300$ ms and $T_2 = 100$ ms. To further demonstrate the signal characteristics of the echo-dephased SSFP dependencies of the steady state signal on different TRs and relaxation times were evaluated. This was achieved by plotting the difference between the steady-state signal, $S(TE)$ obtained at two different TRs ($TR = 3$ ms and 20 ms) and at two different sets of relaxation times ($T_1 = 1200$ ms, $T_2 = 400$ ms and $T_1 = 300$ ms, $T_2 = 100$ ms). In all simulations, the near optimal flip angles ($\alpha_{opt} \approx cos^{-1}[\frac{\epsilon-1}{\epsilon+1}], \epsilon = T_1/T_2$; see (10,11)) were used.

To visualize the effect of local gradient fields (see Eq. 3.1) surrounding the paramagnetic marker during typical 2-dimensional (2D) magnitude image acquisition, numerical simulations were carried out for a coronal slice. The paramagnetic marker of radius 1 mm was assumed to be placed at the center. The signal intensity calculations for bSSFP ($|\phi_G| = 0$/voxel) and echo-dephased SSFP ($|\phi_G| = 4\pi$ /voxel) were carried out over the FOV of 40 mm and slice thickness 40 mm using Eq. 3.4 in the presence of ΔG. The readout was placed along the main magnetic field. The other imaging parameters were: TE/TR=2.5/5.0 ms and T_1/T_2= 300/200 ms.

3.2.3 Guidewire and Phantom

An MR-compatible guidewire made up of Polyetherethertone synthetic polymer core with a diameter of 0.7 mm and compatible with $0.035''$ catheter was used [9]. The paramagnetic material made up of stainless steel alloy was wrapped around the guidewire near its tip with approximate dimensions 1 mm in height and diameter. Frequency measurements yield a LMD of $\Delta\chi V = 1 \times 10^{-11}\ m^3$ (in SI units). The guidewire was inserted into a custom-built phantom with 11 mm diameter tubes to model the blood flow, positioning and tracking of the guidewire in large vessels. The tubes were immersed in a gadolinium (Gd)-doped water and were surrounded by a 2% agarose gel (v/v) doped with 0.5 mM copper sulphate ($CuSO_4$) concentration to closely resemble the relaxation times of muscle tissues for which T_1=900 ms and T_2=50 ms. A 7F introducer sheath was attached to the tubes to facilitate the introduction and manipulation of the guidewire within the tubes.

3.2.4 Passive Tracking Experiments

The passive tracking experiments followed a standard procedure: First, a roadmap of the flow phantom was obtained resembling the vasculature structure of human leg (see Fig. 3.6). Second, positive contrast images from echo-dephased SSFP are merged with the roadmap in near real time in the following manner: In a first step, both roadmap and echo-dephased SSFP images were converted into binary masks by thresholding. In a second step, the two masks were multiplied to confine the marker position within the roadmap, which was finally merged with the original roadmap image. The tubes of the phantom were connected to a pump (14-166; Cobe Laboratories Inc., Lakewood, CO, USA) and the flow was set to 4mL/sec. The circulating water was doped with 0.5mL Gd-DOTA (Dotarem; Guerbet, Roissy CDG Cedex, France) having a T_1 relaxation time similar to blood (1270 ms).

The 2D roadmap was generated based on an inversion-recovery SSFP-FID sequence, as described in [9] using FOV = 30 cm, TR/TE=4.21/2.11 ms, $\alpha = 40^0$ and bandwidth/pixel=720 Hz. Echo-dephased SSFP images were acquired with essentially the same FOV having TR/TE=3.5/1.75 ms, bandwidth/pixel=590 Hz and partial Fourier factor of 5/8. Parallel imaging technique, GRAPPA with an acceleration factor of 3 and 12 reference lines were also utilized, yielding a total image acquisition time for positional marker update of around 250 ms.

3.2.5 Pancreatic Islet Cell Transplantation

Human pancreas were removed from brain-dead donors. Donors were selected according to the results of a multivariate analysis of factors that influence the success of islet isolation. To isolate the islets, the ducts were perfused in a controlled fashion with a cold enzyme. The islets were then separated by gentle mechanical dissociation and purified with the use of continuous gradients of Ficoll–diatrizoic acid (Seromed-Biochrom). Isolated islets were incubated in CMRL-1066 medium (Sigma, USA) (37^0C, 5% atmospheric CO_2) with the liver-specific magnetic resonance contrast agent Resovist®(5µl of contrast agent/ml of the media, Schering, Czech Republic) for 24-48 hours. Resovist®is a commercially available SPIO contrast agent based on carbodextran-coated iron-oxide nanoparticles. This contrast agent has been widely studied experimentally and is also approved for human use. After removal from the tissue culture medium, the islets were centrifuged and washed two times in HBSS (Sigma, USA) solution. A total of approximately 2000 islets were embedded in a 4% gelatin (Sigma, USA)

Rat pancreatic islets were isolated from adult male Lewis rats. Four rats were used as islet donors for one recipient. Isolated islets were incubated in CMRL-1066 medium (Sigma, USA) (37^0C, 5% atmospheric CO_2) with the liver-specific magnetic resonance contrast agent Resovist®(Schering, Czech

Republic) for 1 or 2 days. After labeling the islets were washed three times in HBSS to remove any external iron. The islets were injected into the plastic chamber which was implanted in the rat subcutaneously. All rat protocols were approved by the Ethical Committee of the Institute for Clinical and Experimental Medicine and the Committee for Animal Care of the 2^{nd} Faculty of Medicine of Charles University and the experiments were carried out in accordance with the European Communities Council Directive of 24 November 1986 (86/609/EEC) [10].

Both phantom and rat imaging was done using 3D protocols covering entire phantom and rat. Imaging was done using integrated body coil and spine coil. For both bSSFP imaging and echo-dephased SSFP imaging following imaging parameters were selected. TE/TR 2.37/4.73 ms; slice thickness 2.5 mm; flip angle 55^0; matrix 128×108; FOV 194×230; bandwidth per pixel 400 Hz; NA 12.

3.3 Results

This section begins with the description and elaboration of the results of the numerical simulations of $S(TE)$ using Eq. 3.4 and 2D imaging of the bSSFP and echo-dephased SSFP. Next we describe the phantom experiments to demonstrate the proof of principles of echo-dephased SSFP. This is followed by detailed description and analysis of the spatial accuracy and localization characteristics of the echo-dephased SSFP. The results of the passive tracking experiments in a flow phantom are described next. The results of the visualization of the SPIO-labeled human islets in a phantom using Echo-dephased SSFP is followed. Finally demonstration of the positive contrast visualization of SPIO-labeled pancreatic islet rats in vivo concludes the section.

3.3.1 Signal Characteristics of echo-dephased SSFP

In Fig. 3.2a echo amplitudes at different TEs ($TE = 0$, $TR/2$ and TR) as a function of fractional compensation (ϕ_G) and off-resonance frequency (ϕ_0) are displayed. It can be seen that in the region of around $-2\pi \leq \phi_G \leq 2\pi$ that is when local gradient fields compensate the sequence related dephasing gradients (partially or fully; see cases (1) and (2) in Fig. 3.1b), the signal amplitude is conserved ($M_{xy} > 0.25$) at off-resonant frequencies ($\phi_0 \sim \pm$ 250Hz, ±500Hz). As the fractional gradient compensation ϕ_G makes a transition from $\phi_G \approx 2\pi$ towards $\phi_G \rightarrow 4$ (no compensation; see case (3) in Fig. 3.1b), the signal intensity drops considerably ($M_{xy} < 0.15$). As a result, the difference between the signal intensities of these two regions and thereby contrast, increases dramatically for off-resonant frequencies when dephasing of 4π/voxel is set in a SSFP sequence. The comparison of the contrast to noise ratio (CNR) of the signal, S(TE) reveals that the CNR of

the signal S(TE=TR/2) (CNR > 100) is dramatically higher than the signal, $S(TE = 0)$ and $S(TE = TR)$ (CNR $\approx$ 2). This behavior may be attributed to complete refocusing of the magnetization at $TE = TR/2$ for phase in the range of $\pm 0.8\pi$ [11] and immunity of the signal to field inhomogeneities especially at short TRs. Thus the bSSFP type of sequence with net gradient area $|\phi_G|$ equal to 4 π/voxel is best suited for Echo-dephased SSFP. In Fig. 3.2b and Fig. 3.2c the intensity variation, ΔM_{xy} as a function of the difference between the steady-state signal obtained at two different TRs (TR=3 ms and 20 ms) and for two different sets of relaxation times (T_1/T_2=1200 ms/400 ms, and T_1/T_2=300 ms/100 ms) respectively is shown. The ΔM_{xy} obtained at $TE = 0$, decreases with an increase in TR and decrease in relaxation times, whereas at TE=TR it increases with an increase in TR and decrease in relaxation times. This is in contrast to the ΔM_{xy} obtained at $TE = TR/2$ which remains almost constant with a variation in TR as well as the ratio of relaxation times (T_1/T_2). These properties reveal that in echo-dephased SSFP sequence, if the signal is obtained at TE=TR/2, the positive contrast generation due to paramagnetic material is independent of TR as well as the ratio of the relaxation times (T_1/T_2) of the sample being imaged.

Fig. 3.3a depicts the simulated bSSFP magnitude image exhibiting the signal intensity pattern of typical susceptibility artifacts (black voids) due to paramagnetic marker. As noted earlier, the phase dispersion ϕ_G, within a voxel for bSSFP sequence is zero. However, the local gradient field induced by paramagnetic marker introduces additional dephasing within its surrounding tissues. As a result, the signal intensity drops as a function of additional dephasing. In Fig. 3.3b, simulated Echo-dephased SSFP magnitude image is shown. In Echo-dephased SSFP, the local gradient field competes with deliberately introduced sequence related dephasing gradients at specific spatial locations leading to positive signal (hyper intense blobs in Fig. 3.3b) with respect to its background. The distance between the two prominent hyper intense blobs was found to be $\pm$1cm for the simulation parameters used.

3.3.2 Phantom Experiments

The overview of the experimental flow phantom is illustrated in Fig. 3.4a. The bSSFP image showing the flow tubes and local field perturbations (see arrow in Fig. 3.4a) from the inserted paramagnetic marker material localizing the tip of the guidewire is displayed. Fig. 3.4b and 3.4c depict the sample images obtained using echo-dephased SSFP with similar sequence parameters as that of bSSFP (Fig. 3.4a) but with different slice thicknesses. For comparison, the image obtained using white marker imaging method at a slice thickness of 40 mm (Fig. 3.4d) is also shown.

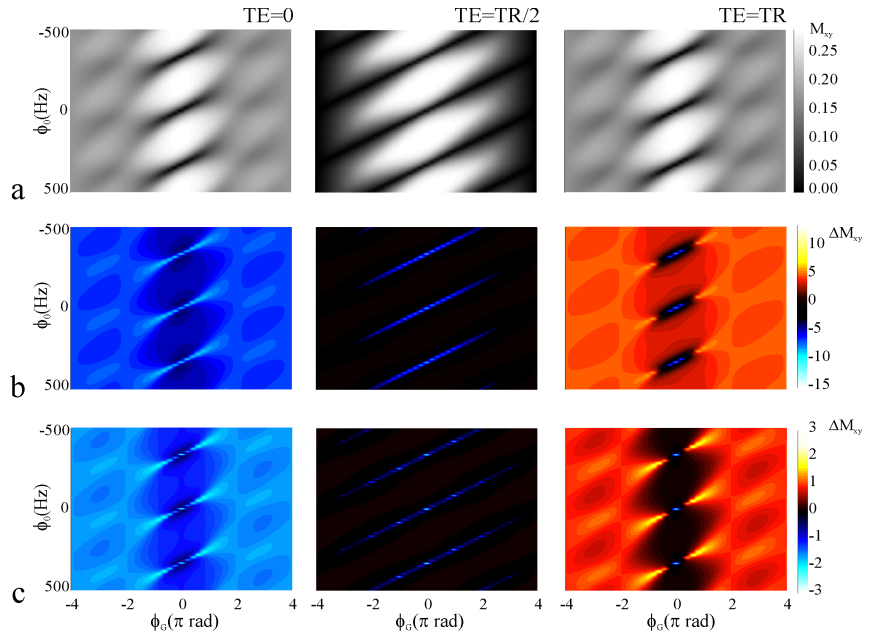

Figure 3.2: a) Signal amplitudes $S(TE)$ at various TEs ($TE = 0, TR/2, TR$) resembling the well-known SSFP sequences namely SSFP-FID, bSSFP and SSFP-ECHO respectively as a function of ϕ_G varying in the range of $[-4\pi : 4\pi]$ and off-resonance frequencies (ϕ_0) varying from -540 Hz to 540 Hz at optimal flip angle. The other imaging parameters were: TR=3 ms, $T_1 = 300$ ms and $T_2 = 100$ ms. In the region of around $-2\pi \leq \phi_G \leq 2\pi$ that is when local gradient fields compensate the sequence related dephasing gradients (partially or fully), the signal amplitude is conserved ($M_{xy} > 0.25$) at off-resonant frequencies ($\phi_0 \approx \pm 250$ Hz, ± 500 Hz). As the fractional gradient compensation ϕ_G makes a transition from $\phi_G = 2\pi$ towards $\phi_G \rightarrow 4$(no compensation), the signal intensity ($S(TE)$) drops considerably ($M_{xy} < 0.15$). b) The signal difference between $S(TE)$ at two different TRs (TR=3 ms and 20 ms) and c) at two different sets of relaxation times ($T_1/T_2 = 1200$ ms/400 ms and $T_1/T_2 = 300$ ms/100 ms). Thus, if the signal is obtained at $TE = TR/2$, the positive contrast generation due to paramagnetic material is independent of TR as well as the ratio of relaxation times (T_1/T_2) of the sample being imaged.

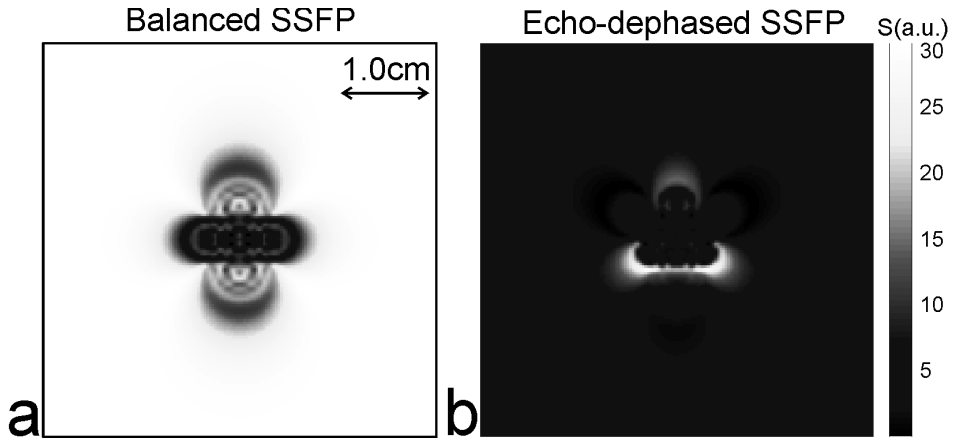

Figure 3.3: Numerical simulation of the a) balanced SSFP and b) Echo-dephased SSFP sequence for a coronal slice with readout along the main magnetic field over the FOV of 40 mm at optimal flip angle in the presence of the paramagnetic marker located at the center. The other imaging parameters were: TE/TR=2.5 ms/5 ms, T_1/T_2= 300 ms/200 ms, slice thickness 40 mm. The signal level (S) is shown in arbitrary units (a.u.).

3.3.3 Localization Characteristics of echo-dephased SSFP

To characterize the localization accuracy of echo-dephased SSFP, the distance d between the centers of the two prominent hyper-intense blobs was analyzed as a function of TR within about 4.7 ms to 100 ms.

From Eq. 3.3, phase evolution from local gradients as induced by paramagnetic marker materials are directly proportional to TR. Thus, with increasing TR, gradient compensation is located further and further away from the marker's position according to [5]

$$r(TR) = \sqrt[4]{TR} \tag{3.7}$$

In Fig. 3.5, localization accuracy of echo-dephased SSFP is analyzed. From Eq. 3.7, the distance (r) from the perturbation source, where local gradient compensation takes place, is expected to scale proportional to TR in a double logarithmic plot with a slope of 1/4. This is in good correspondence with the experimental results from hyper intensity distance analysis displayed in Fig. 3.5, yielding a slope of 0.287 close to expected value.

3.3.4 Passive Tracking

Selective frames of passive guidewire tracking from echo-dephased SSFP are shown in Fig. 3.6 at various stages of the guidewire marker positions. Here, Fig. 3.6a shows the images obtained by applying the echo-dephased SSFP

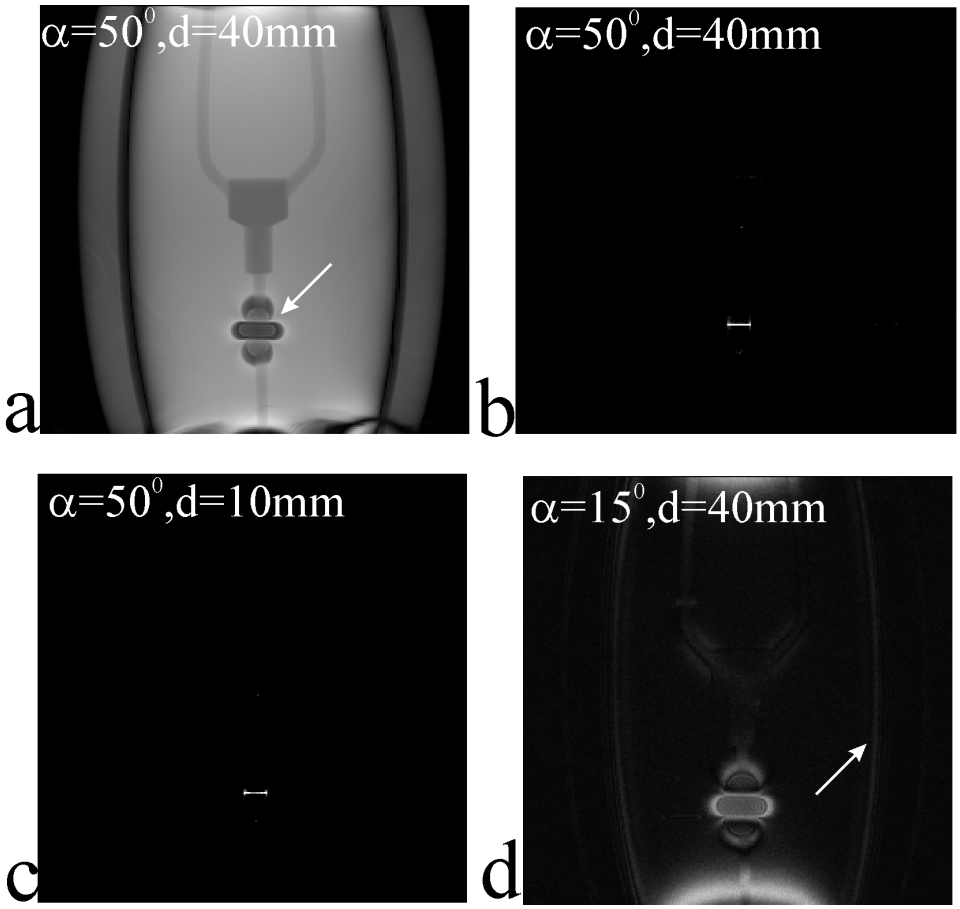

Figure 3.4: In-vitro phantom images a) An experimental phantom image in the coronal direction using bSSFP sequence showing the flow tubes and black void (see arrow) resembling dipolar form due to local field perturbations induced by paramagnetic marker material wrapped around inserted guidewire is clearly visible (The imaging parameters were: $\alpha = 50^0$, TR=4.7 ms, slice thickness=40 mm, matrix=256×256). b) An echo-dephased SSFP image obtained with the same parameters and c) with a slice thickness=10 mm. The net dephasing of 4π/voxel ensures that background is completely dephased and appears in intense black whereas within the close vicinity of the marker a hyper intense signal is formed from local gradient compensation (consistent with the theoretical predictions). d) Illustrative sample image using a white-marker imaging method with 0% slice rephasing at slice thickness=40 mm. The other imaging parameters were: $\alpha = 15^0$, TR=13 ms, TE=10 ms.

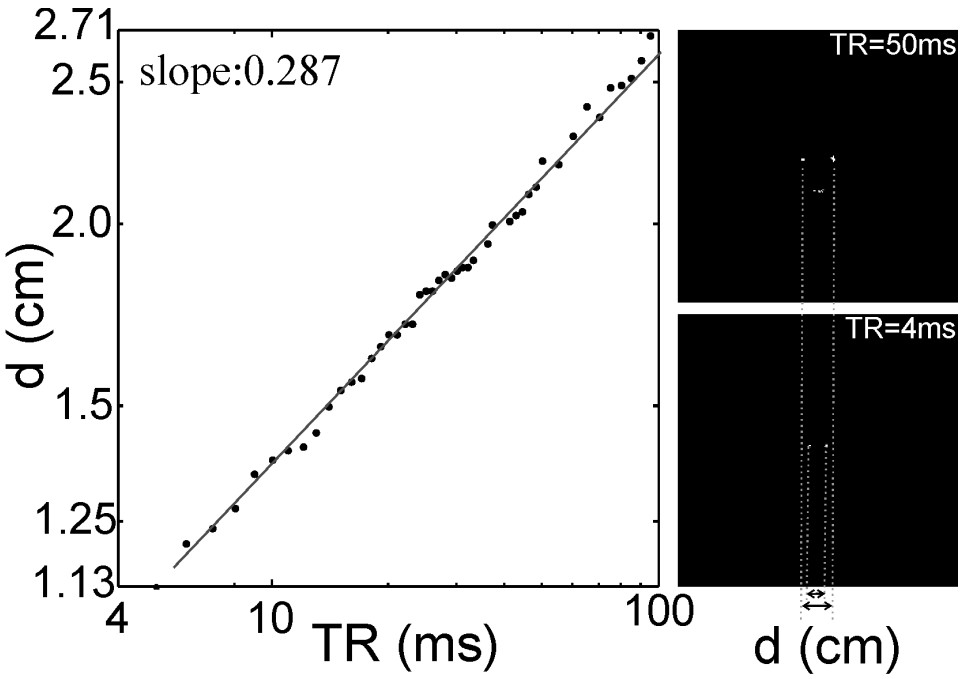

Figure 3.5: Accuracy of the marker localization using echo-dephased SSFP: Variation in distance (d) between two hyper-intense blobs with respect to TR is plotted using double logarithmic scale. The slope of the fitted line was 0.287. A minimum distance of around 1.2 cm was observed with shorter TRs (4-5 ms) indicating its proximity to the marker material. Calculation of the distance is shown on the adjacent image insets.

only. It may be interesting to note that because of the ring-like structure of the marker material its visualization is independent of its orientation with respect to main magnetic field (B_0). This is clearly evident from the middle panel of the Fig. 3.6a in which positive contrast generated by the marker material is clearly visible even though it is aligned at an acute angle with respect to main magnetic field. The corresponding fusion of the previously acquired roadmap and the echo-dephased SSFP image are shown in Fig. 3.6b. Here, the position of the marker was updated at about four frames per second. The temporal resolution could be increased up to eight frames per second by maintaining the FOV only over vessel region and reducing the in-plane resolution without significant degradation of the marker depiction.

3.3.5 Pancreatic Islet Cell Visualization

In the following, application of echo-dephased SSFP for positive contrast visualization of the SPIO-labeled isolated pancreatic islets is explored in detail. Visualization of the human pancreatic islets in a phantom using bSSFP and echo-dephased SSFP protocols is demonstrated in Fig. 3.7. The upper panel shows the selective consecutive frames (cropped) of a 3D dataset obtained using bSSFP protocol. The hypointense regions depicting localization of the pancreatic islets (yellow arrows) is clearly visible. The lower panel shows the selective consecutive frames (cropped) of a 3D dataset obtained using echo-dephased SSFP protocol and essentially using the same parameters as that of bSSFP. Distributed hyperintensities (see yellow arrows) are clearly visible within the close vicinity of the islets. Also the plastic tube which appears as black circle in bSSFP images do not appear with positive contrast indicating selective localization of the islets. However, edges of the phantom also appear as hyperintensities (yellow arrow head) due to unwanted gradient compensation in that region.

Visualization of the rat pancreatic islets subcutaneously transplanted into a chamber (in vivo) is demonstrated in Fig. 3.8. As in the phantom experiments the upper panel shows the selective consecutive frames (cropped) of a 3D dataset obtained using bSSFP protocol. Hypointense region depicting the localization of islets (see yellow arrow) in a rat chamber is visible. However, due to confounding larger hypointense region near the chamber and enhancement of other tissues visualization of islets is unclear. The lower panel shows selective consecutive frames (cropped) of a 3D dataset obtained using echo-dephased SSFP protocol and essentially using the same parameters as that of bSSFP. hyperintensite region (yellow arrow) is clearly visible within the close vicinity of the islets. A good suppression of the background is achieved that leads to excellent localization and tracking of the islets.

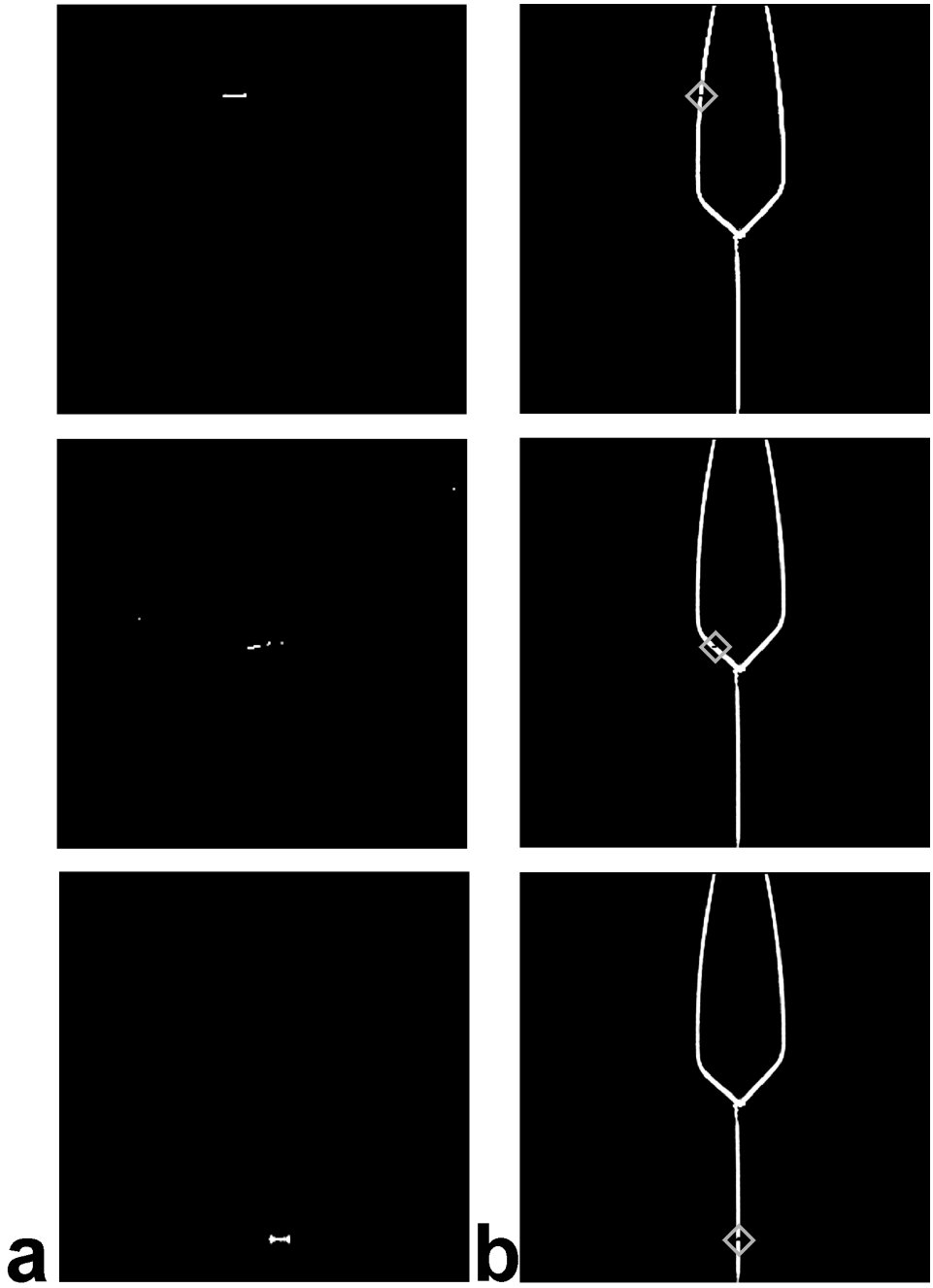

Figure 3.6: Passive tracking of the interventional guidewire using echo-dephased SSFP technique a) The positive contrast marker images obtained using echo-dephased SSFP technique at different stages of the guidewire tracking in a flow phantom. b) The overlay of the marker position (surrounded by gray diamonds) onto previously acquired 2-D roadmap. The roadmap was acquired using IR-FISP sequence.

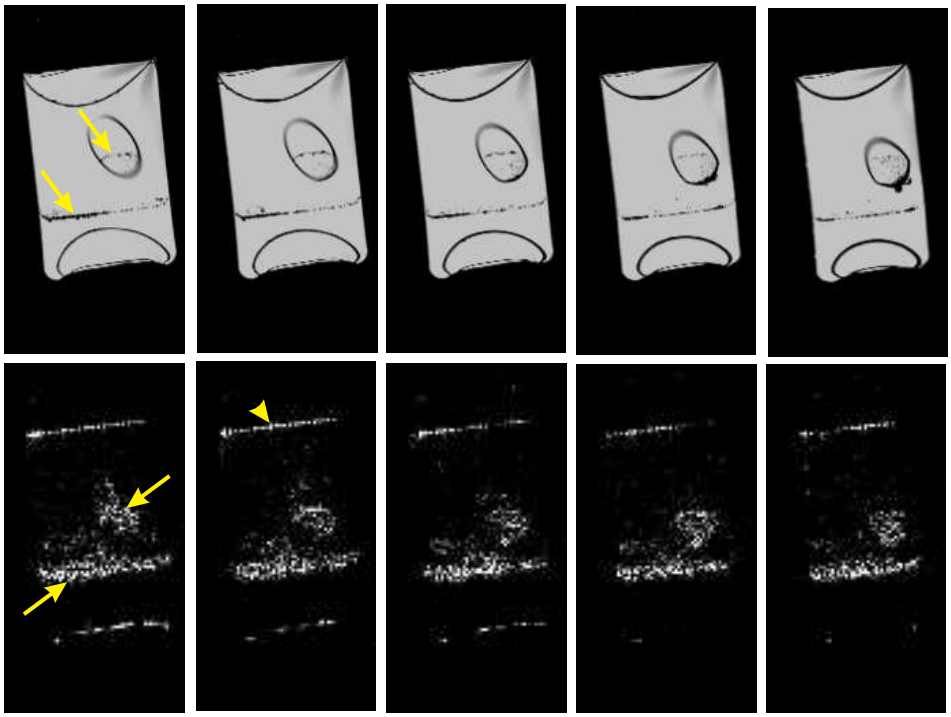

Figure 3.7: Human pancreatic islets in a phantom. The upper panel shows the selective consecutive frames of a 3D dataset obtained using bSSFP protocol. Hypointense regions depicting localization of the pancreatic islets (yellow arrows) is clearly visible. The imaging parameters were: TE/TR 2.37/4.73 ms; slice thickness 2.5 mm; flip angle 55^0; matrix 128×108; FOV 194×230. The lower panel shows the selective consecutive frames of a 3D dataset obtained using echo-dephased SSFP protocol and essentially using the same parameters as that of bSSFP. Distributed hyperintensities (yellow arrows) are clearly visible within the close vicinity of the islets. Edges of the phantom also appear as a hyperintensities (yellow arrow head)

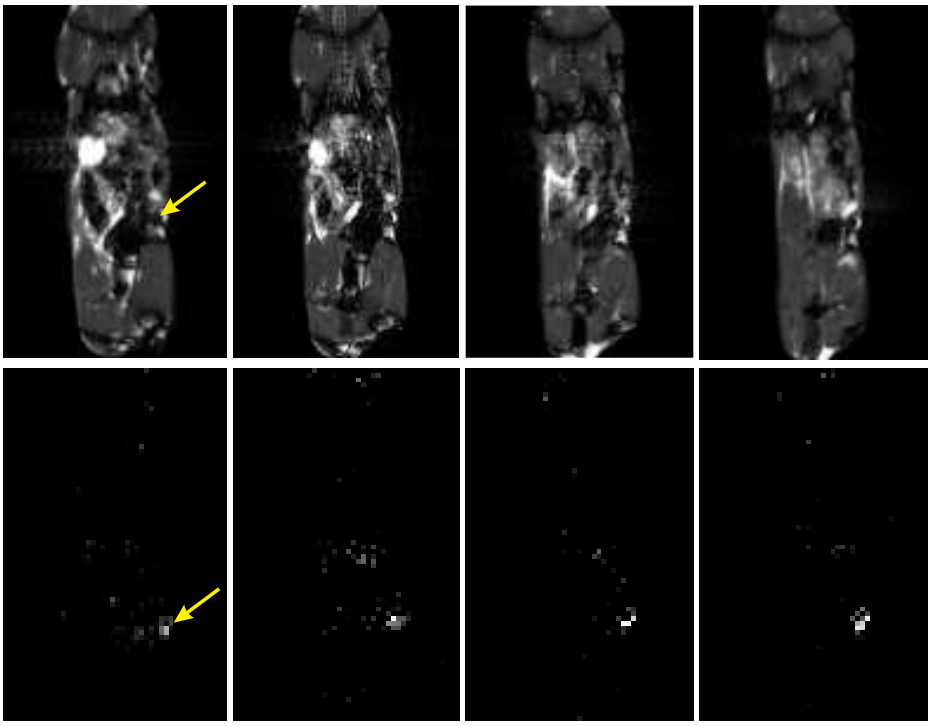

Figure 3.8: Visualization of the rat pancreatic islets subcutaneously transplanted into a chamber. The upper panel shows the selective consecutive frames of a 3D dataset obtained using bSSFP protocol. Hypointense region depicting the localization of islets (yellow arrow) in a rat chamber is visible. The imaging parameters were: Similar to phantom studies, the lower panel shows selective consecutive frames of a 3D dataset obtained using echo-dephased SSFP protocol and essentially using the same parameters as that of bSSFP. hyperintensite region (yellow arrow) is clearly visible within the close vicinity of the islets with appreciably good suppression of background.

3.4 Discussion

It was demonstrated that the dephasing by 4 π/voxel in the readout direction (from bottom to top in the images displayed; see Fig. 3.4) ensures a completely dephased background and hyper intense signals appear only in the close vicinity of the paramagnetic marker material due to local field compensation; being consistent with theoretical predictions (see Fig. 3.1b and Fig. 3.3b). Using white marker imaging method at lower slice resolutions (slice thickness=40 mm) partial volume effects due to tissue interfaces (see arrow in Fig. 3.4d), inherent main magnetic field inhomogeneities at the two extremes of the magnet appears with prominent positive contrast. This may hamper the accurate discrimination of the paramagnetic marker material from other unwanted background signal enhancements. Recently it has been shown that by applying equal and opposite dephasing gradients and performing modulus subtraction of the resultant images partial volume effects can be eliminated [12]. However, this doubles the acquisition time and in addition reduces the SNR of the resultant image.

Appropriate matching of the marker position and its localization in the image is one of the major prerequisite of MR-guided interventions. In the echo-dephased SSFP sequence, compensation of the sequence-related dephasing gradients by the local gradient fields induced due to paramagnetic marker always takes place outside of the marker. and the spatial accuracy of the positive contrast generated by echo-dephased SSFP has to be determined. Reconsidering Eq. 3.3, the phase evolution of spins ($G(x)$) is expressed as (e.g., in the x-direction):

$$\begin{aligned} \phi_G(x) &= \gamma \cdot TR \cdot (G_x \cdot x + \Delta G_x \cdot (x - x_0)) \\ &= \gamma \cdot G_x \cdot TR \cdot \left(x \cdot \left(1 + \frac{\Delta G_x}{G_x} \right) - x_0 \frac{\Delta G_x}{G_x} \right) \end{aligned} \tag{3.8}$$

Noticing that $k_x = \gamma \cdot G_x \cdot TR$, the position x will be encoded at position $x^{'}$ in the reconstructed image [13] according to

$$x' = x \cdot \left(1 + \frac{\Delta G_x}{G_x} \right) - x_0 \left(\frac{\Delta G_x}{G_x} \right) \tag{3.9}$$

Typically $G_x \sim 10$ mT/m yielding $\gamma \cdot G_x \cdot x = 420$ Hz/mm, whereas frequency offsets from paramagnetic markers are in the range of 500 Hz at 1 cm distance for a given LMD at 1.5 T. As a result when G_x fully compensate for ΔG at the iso-center, it leads to positional error of the marker in the range of 1 pixel. However, as one goes further away from the iso-center, spatial encoding falls in higher audio frequency range (i.e., when $G_x >> G_x$, see Eq. 3.9) thereby making $x \approx x'$. Thus in Echo-dephased SSFP for a complete gradient compensation scheme (for example at position (1) in Fig. 3.1b), signal contribution comes from spatially encoded off-resonance frequencies.

The hyper-intense blobs in images produced by echo-dephased SSFP are within the close vicinity of the marker; however, it should be recognized that these blobs always lie in the surrounding of the actual marker position. The distance between the exact location of the marker and any one of the hyper-intense blobs is same and the mid-point of the distance between two hyper-intense blobs should lie on the interventional device. Hence, the analysis of distance between two hyper-intense blobs as function of TR was performed (see Fig. 3.5). It can be inferred from this analysis is that in echo-dephased SSFP the distance d can be minimized for a given LMD by keeping TR as short as possible. A minimum distance of around 1.2 cm was observed at shorter TRs (4-5 ms) being consistent with theoretical predictions (see Fig. 3.3) and indicating its good proximity (0.6 cm) to the marker material. The fact that the proximity of the localization produced by echo-dephased SSFP to the physical position of the marker is directly proportional to TR for a given LMD makes this technique suitable for MR-guided interventions. This may lead to further increase in temporal resolution, which is currently one of the major obstacles of the utilization of passive tracking in practice. Also the positive signal contrast of the echo-dephased SSFP may benefit from the fact that the bSSFP sequences are less immune to main magnetic field inhomogeneities at low TRs.

In MR-guided interventions, passive tracking techniques utilizes either small paramagnetic materials [14] or contrast agents [15] for visualization of interventional devices but reliable localization and visualization of marker materials with respect to background is a major challenge. In this work, it was successfully demonstrated that the tracking of paramagnetic marker materials based on echo-dephased SSFP is feasible and achieves accurate and reliable marker localization with excellent background suppression.

Thanks to excellent background suppression due to echo-dephased SSFP method, and in contrast to other passive tracking techniques, there was no need to perform baseline subtraction [16] or additional post-processing [9]. This allowed for fast calculation of marker positions and thus led to only insignificant delays between the actual image acquisition and the corresponding update of the roadmap. Generally, any baseline subtraction method may suffer from background signal enhancement in presence of motion, whereas additional post-processing such as gradient signal maxima calculation as in (12) may be unsuitable for real time display of the images. Thus, present approach with its high contrast characteristics and better proximity to the marker material may be suitable for real time passive interventional MRI.

Another interesting application of Echo-dephased SSFP is to visualize, localize and track the SPIO-labeled cells and was demonstrated here for pancreatic islets visualization in in vitro as well as in vivo. Both phantom and rat studies clearly demonstrated that visualization of the SPIO-labeled islets with positive contrast is reliable and feasible. Although bSSFP is well suited for visualization of SPIO-labeled cells [17], it suffers from banding

artifacts especially at high field strengths ($\geq$3 T). The banding artifacts are clearly visible in both phantom (see Fig. 3.7) and rat (see Fig. 3.8) studies. On the contrary using Echo-dephased SSFP do not suffer from such artifacts even in vivo. Thus, Echo-dephased SSFP in combination with bSSFP may potentially be employed as a valuable clinical tool to localize and track the SPIO-labeled islets.

The previously proposed methods; morphing SSFP [5] and susceptibility gradient mapping (SGM) [18] also exploits the local gradient perturbations induced by the marker material in their immediate surrounding. In morphing SSFP, gradient perturbations compete with sequence-related dephasing gradients to induce a transition from SSFP-echo to balanced SSFP. In addition, background suppression, and thus positive contrast, is achieved by using the intrinsic high signal difference between bSSFP and SSFP-ECHO, especially for low flip angles in combination with long TR. In contrast in echo-dephased SSFP, echo-dephasing ensures excellent background suppression even at large flip angles with short TR. Since echo-formation is an amalgamation of SSFP-FID, SSFP-ECHO and bSSFP (see Fig. 3.1b), it shows similar sensitivity as these three SSFP sequences to flip angle variation as well as different types of off-resonances. The major advantage of echo-dephased SSFP is its short TR, providing a positive contrast region in the very close vicinity of the marker material with high temporal resolution.

The SGM method employs a localized short term Fourier transform method onto a gradient echo dataset for mapping local marker gradients along all three spatial directions (x, y and z) yielding a positive contrast image. SGM is thus based on the echo-shift in k-space, whereas echo-dephased SSFP selectively acquires shifted echoes along the readout similar to 1D SGM. However, from interventional application point-of-view, some of the current limitations of SGM method are: the positive contrast generation partially relies on TE value [19], in-phase TE is needed to avoid water-fat boundary artifacts and being post-processing method makes it computationally cumbersome.

Similar to all passive positive contrast methods, other sources of large-scale susceptibility gradients such as lung-liver interfaces may appear with positive contrast in echo-dephased SSFP as well (see Fig. 3.7). A special care must therefore be taken to avoid such "false positives". For example, in current application marker position search space was confined within the vicinity of the vascular structure. It should also be noted that, since in this method marker position is updated on the previously acquired roadmap some of the disadvantages of the passive tracking remains when motion enters the game. However, the area of application for which these methods are being developed is the interventional peripheral MR angiography (ipMRA), where there is a low risk of or limited patient motion. Hence, the presented method may find prominent application to perform these interventions.

3.5 Conclusion

A novel concept for the generation of positive contrast from local susceptibilities, termed echo-dephased SSFP was proposed. In principle, echo-dephased SSFP is an unbalanced SSFP type of sequence, in which echoes are dephased prior to readout. We have demonstrated that this echo-dephasing approach ensures excellent cancellation of any background signals. From local gradient compensation hyper-intense signals are formed and thus a positive contrast emanates within the close vicinity of paramagnetic marker materials. Hyper-intense signals are mainly of bSSFP type, which ensures sufficient signal intensity with respect to background. A reliable localization and robust marker detection was demonstrated using the proposed method. The passive guidewire tracking experiments were performed in flow phantoms suggesting suitable applicability of the echo-dephased SSFP for MR-guided interventions such as ipMRA. Finally utilization of echo-dephased SSFP for positive contrast visualization of SPIO-labeled islets was demonstrated both in vitro and in vivo.

References

[1] J. Reichenbach, R. Venkatesan, D. Yablonskiy, M. Thompson, S. Lai, and E. Haacke, "Theory and application of static field inhomogeneity effects in gradient-echo imaging," *J Magn Reson Imaging*, vol. 7, p. 266–79, Apr. 1997.

[2] J. Frahm, K. Merboldt, and W. Hanicke, "Direct FLASH MR imaging of magnetic field inhomogeneities by gradient compensation," *Magn Reson Med*, vol. 6, p. 474–80, Apr. 1988.

[3] J. Seppenwoolde, M. Viergever, and C. Bakker, "Passive tracking exploiting local signal conservation: the white marker phenomenon," *Magn Reson Med*, vol. 50, p. 784–90, Oct. 2003.

[4] V. Mani, K. Briley-Saebo, V. Itskovich, D. Samber, and Z. Fayad, "Gradient echo acquisition for superparamagnetic particles with positive contrast (GRASP): sequence characterization in membrane and glass superparamagnetic iron oxide phantoms at 1.5T and 3T," *Magn Reson Med*, vol. 55, no. 1, p. 126–35, 2006.

[5] O. Bieri, S. Patil, H. Quick, and K. Scheffler, "Morphing steady-state free precession," *Magn Reson Med*, vol. 58, p. 1242–8, Dec. 2007.

[6] D. A. Yablonskiy and E. M. Haacke, "Theory of NMR signal behavior in magnetically inhomogeneous tissues: the static dephasing regime," *Magnetic Resonance in Medicine: Official Journal of the Society of*

Magnetic Resonance in Medicine / Society of Magnetic Resonance in Medicine, vol. 32, p. 749–763, Dec. 1994. PMID: 7869897.

[7] K. Scheffler, "A pictorial description of steady-states in rapid magnetic resonance imaging," *Concepts in Magnetic Resonance*, vol. 11, no. 5, p. 291–304, 1999.

[8] M. Gyngell, "The application of steady-state free precession in rapid 2DFT NMR imaging: FAST and CE-FAST sequences," *Magn Reson Imaging*, vol. 6, p. 415–9, Aug. 1988.

[9] R. Mekle, E. Hofmann, K. Scheffler, and D. Bilecen, "A polymer-based MR-compatible guidewire: a study to explore new prospects for interventional peripheral magnetic resonance angiography (ipMRA)," *J Magn Reson Imaging*, vol. 23, p. 145–55, Feb. 2006.

[10] D. Jirák, J. Kríz, V. Herynek, B. Andersson, P. Girman, M. Burian, F. Saudek, and M. Hájek, "MRI of transplanted pancreatic islets," *Magnetic Resonance in Medicine: Official Journal of the Society of Magnetic Resonance in Medicine / Society of Magnetic Resonance in Medicine*, vol. 52, pp. 1228–1233, Dec. 2004. PMID: 15562474.

[11] K. Scheffler and J. Hennig, "Is TrueFISP a gradient-echo or a spin-echo sequence?," *Magn Reson Med*, vol. 49, p. 395–7, Feb. 2003.

[12] J. Seppenwoolde, K. Vincken, and C. Bakker, "White-marker imaging-Separating magnetic susceptibility effects from partial volume effects," *Magn Reson Med*, July 2007.

[13] B. H. EM, *Magnetic resonance imaging: physical principles and sequence design*. New York: Wiley, 1999.

[14] D. Rubin, A. Ratner, and S. Young, "Magnetic susceptibility effects and their application in the development of new ferromagnetic catheters for magnetic resonance imaging," *Invest Radiol*, vol. 25, p. 1325–32, Dec. 1990.

[15] O. Unal, F. Korosec, R. Frayne, C. Strother, and C. Mistretta, "A rapid 2D time-resolved variable-rate k-space sampling MR technique for passive catheter tracking during endovascular procedures," *Magn Reson Med*, vol. 40, p. 356–62, Sept. 1998.

[16] J. Seppenwoolde, L. Bartels, R. van der Weide, J. Nijsen, A. van het Schip, and C. Bakker, "Fully MR-guided hepatic artery catheterization for selective drug delivery: a feasibility study in pigs," *J Magn Reson Imaging*, vol. 23, p. 123–9, Feb. 2006.

[17] C. Heyn, C. V. Bowen, B. K. Rutt, and P. J. Foster, "Detection threshold of single SPIO-labeled cells with FIESTA," *Magnetic Resonance in Medicine: Official Journal of the Society of Magnetic Resonance in Medicine / Society of Magnetic Resonance in Medicine*, vol. 53, pp. 312–320, Feb. 2005. PMID: 15678551.

[18] H. Dahnke, W. Liu, D. Herzka, J. Frank, and T. Schaeffter, "Susceptibility gradient mapping (SGM): a new postprocessing method for positive contrast generation applied to superparamagnetic iron oxide particle (SPIO)-labeled cells," *Magn Reson Med*, vol. 60, p. 595–603, Sept. 2008.

[19] E. Vonken, M. Schar, and M. Stuber, "Positive contrast visualization of nitinol devices using susceptibility gradient mapping," *Magn Reson Med*, vol. 60, p. 588–94, Sept. 2008.

Chapter 4

Projection-Reconstruction Imaging with Echo-Dephasing

This chapter is based upon:
S. Patil, O.Bieri, P. Jhooti, K. Scheffler, "An Automatic Slice Positioning for Passive Real-Time Tracking of Interventional Devices Using Projection Reconstruction Imaging with Echo-Dephasing (PRIDE)", Magn. Reson. in Med., In Press, 2009.

4.1 Introduction

Although X-ray is considered as the de-facto standard for endovascular interventions, there is a growing interest in MR-guided interventions because of its excellent soft-tissue contrast, lack of ionizing radiation and multi-planar imaging capability. In clinical practice, however, one of MRI's drawbacks is the difficulty in localization and high-contrast visualization of interventional devices (for e.g., guidewires and catheters). In addition, fast localization and automatic adjustment of scan plane position is highly desirable. As a result, considerable efforts are being undertaken towards achieving these objectives.

Current methodologies for MR-guided interventions can be broadly classified into active, semi-active and passive tracking. Active tracking utilizes locally sensitive transmit/receive coils for either localization [1] or visualization [2] or is based on the visualization of currentrelated local field inhomogeneities produced in a small loop [3]. Localization of the coil is achieved in few milliseconds through acquisition of one dimensional (1D) projections along all three spatial directions (X, Y and Z). The positional information is then used to actively align the position of the imaging slice. In addition, velocity of the device has been used to automatically adjust the imaging parameters [4]. However, potential radiofrequency (RF) heating issues due to standing waves along the conducting cables still represent one of the major and most prominent potential safety hazards with active tracking [5]. The standing waves lead to storage of electrical energy, which may be transmitted into the human body. With nitinol guidewires temperatures of up to 74^0C has been reported [5]. Some approaches have been suggested to reduce the heating risks, see for example Ref. [6], but widespread use of active tracking in humans is still limited due to design challenges.

Semi-active devices utilize self-resonant RF circuits and have no direct electrical connection to the scanner. Such devices incorporate miniature RF coils tuned to Larmor frequency of the scanner and encapsulates a small container filled with a solution having short T_1 [7, 8]. As a result, using a fast imaging sequence with low flip angles generates a positive contrast for the sample within the coil due to local gain of the B_1 field [9], in combination with the relatively low signal from the background. However, semi-active devices still require a mechanical connection (for e.g. laser fiber) between the instrument and the scanner which greatly hampers the handling of such interventional devices.

Contrary to active tracking, passive techniques do not suffer from RF heating problems since either small paramagnetic materials (causing magnetic susceptibility variations [10]) or contrast agents (such as 4-6 vol % Gd-DTPA to increase the MR signal [11]) are used for visualization of interventional devices. Moreover, unlike semi-active devices passive devices do not require any mechanical scanner connection. Reliable localization and visualization of marker materials has recently been proposed using a

steady state free precession (SSFP) positive contrast technique [12]. However, image-based passive tracking is slow and hence does not provide fast coordinate updates as required for automatic slice positioning (ASP) mechanism.

The passive tracking of interventional devices, such as guidewires or catheters, during endovascular interventions using ferromagnetic materials was first introduced by Rubin et al [10] based on signal voids caused by local susceptibility variations [13, 14]. Using a positive contrast technique known as white marker technique [15], the conspicuity of the paramagnetic markers containing dysprosium oxide can be further improved. In another approach, a positive contrast was generated for an MR-compatible guidewire containing an iron particle wrapped around it from local off-resonances using low flip angle excitations in balanced SSFP (bSSFP) [16]. Although positive contrast enhances the conspicuity of the marker as compared to the background, it results in a loss of anatomical structure. Thus, passive tracking or localization of the guidewire can be achieved using a baseline subtraction method [17] or a positive contrast image [16] overlaid on either anatomical reference images or a vascular roadmap (i.e., an angiogram). However, relatively long image acquisition times, leads to an undesired increased sensitivity to motion and/or flow with such overlay techniques. In addition, extended slice thickness (40-50 mm) is required in order to guarantee that the device always lie within the plane being imaged. In spite of these disadvantages, passive tracking utilizing balloon catheters filled with CO_2 has successfully been demonstrated in patients who had undergone diagnostic cardiac catheterization [18, 19].

In order to further enhance the applicability of passive tracking techniques, the above-mentioned disadvantages need to be overcome and a real-time slice position update to the detected device location must be achieved in a comparable time to that of active tracking. In this work, a novel projection-based passive tracking technique is proposed, termed Projection Reconstruction Imaging with Echo-DEphasing (PRIDE). PRIDE is based on an acquisition of projections using dephasing gradients along all three spatial (X, Y and Z) dimensions. Using PRIDE, 3D position of the interventional device tip containing paramagnetic marker is localized, which in turn is used to automatically adjust the scan plane of the imaging slice. We first describe the concept of local gradient field compensation used in PRIDE, followed by in-vitro experiments demonstrating the feasibility of appropriate marker detection in the presence of off-resonance related degradations caused by unwanted inhomogeneities (air/tissue interfaces etc). Then we describe the ASP mechanism incorporating PRIDE as a tracking sequence to provide positional information of the paramagnetic marker to bSSFP sequence serving as an imaging sequence. The demonstration and discussion of ASP mechanism on the clinical scanner is done by means of phantom results. Finally, in vivo experiments in a swine model are presented that corroborate the

in-vitro results for robust and reliable detection of marker using PRIDE.

4.2 Materials and Methods

Phantom measurements, in vivo measurements and calibrations were performed on a Siemens 1.5 T Espree system (Siemens Healthcare, Erlangen, Germany) employing maximum gradient strength of 33 mT/m and a slew rate of 170 mT/(m×ms). Imaging was done using integrated spine coils and body phased array coils. Numerical simulations, data analysis and visualization were done using Matlab 2006a (The MathWorks, Inc.).

4.2.1 Local Gradient Fields

A small point-like paramagnetic marker material wrapped around a guide wire (for example, as shown in Fig. 4.1a) induces a field perturbation (in SI units)

$$\Delta B_z(x,y,z) = \frac{B_0 \Delta\chi V}{4\pi} * \frac{x^2+y^2-2z^2}{(x^2+y^2+z^2)^{5/2}} \tag{4.1}$$

of dipolar form in the main magnetic field B_0. Here, V is the volume of the paramagnetic material, $\Delta\chi$ is the susceptibility difference between the marker material and the surrounding tissues and $\Delta\chi V$ (m^3) characterizes the local magnetic dose (LMD) [15]. The Local gradient fields (ΔG) can be derived from partial derivatives of the field perturbation (ΔB_z, see Eq. 4.1) as,

$$\Delta G_{x,y,z} = \delta_{x,y,z}(\Delta B_z) \tag{4.2}$$

Simulated ΔG values are shown in Fig. 4.1b ($\delta_z(\Delta B_z)$) and Fig. 4.1c ($\delta_{x,y}(\Delta B_z)$). These local gradients may have additive or compensating interference with applied imaging gradients. In PRIDE, we exploit the compensating effect between local gradients and applied imaging gradients. In the following, we elucidate the idea of compensating echo-dephasing gradients in PRIDE.

4.2.2 Projection Reconstruction Imaging with Echo-Dephasing (PRIDE)

The sequence diagram of the PRIDE sequence is shown in Fig. 4.2a. Readout gradients (GR) are placed along all three physical axes (X, Y and Z). Echo-dephasing (preferably 4π) is achieved by switching on a mono-polar gradient wave-form for readout (essentially, there is no pre-phasing or refocusing of the readout gradient). Therefore, in principle, no transversal states can contribute to the echo similar to echo-dephased SSFP [20] and background signals are heavily suppressed. In the presence of marker-related

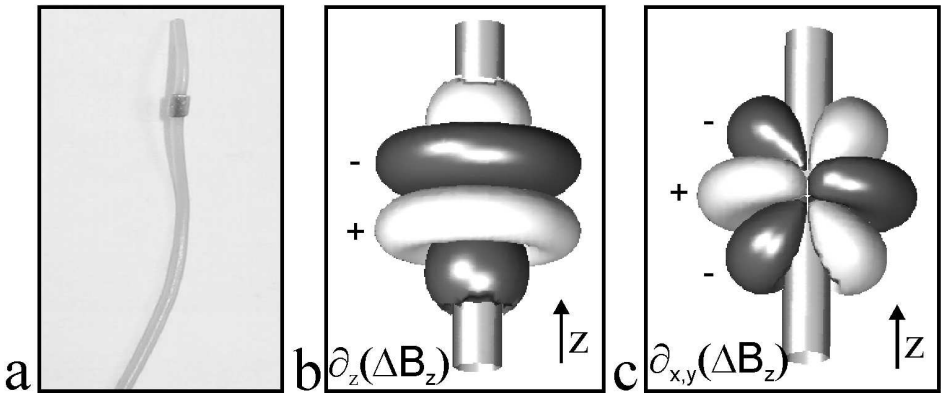

Figure 4.1: a) Prototype guidewire made up of a polyetherethertone synthetic polymer core with a diameter of 0.7 mm being compatible with $0.035''$ catheters. The paramagnetic ring (1mm stainless steel in height and diameter) mounted on the guidewire tip has an approximate local magnetic dose of $\Delta\chi V = 1 \times 10^{-11}\ m^3$. b) Simulated local field gradients (ΔG) (The iso-surface gradient strength of ΔG is about 15 mT/m) induced by the paramagnetic ring for a given local magnetic dose at 1.5 T with respect to z-direction and c) x, y directions. These local gradient fields may compensate locally for any externally applied dephasing gradient.

local field gradients (ΔG, see Fig. 4.1b and Fig. 4.1c) echo-dephasing gradients (GR) may be compensated during each projection to give rise to a normal echo. For example, at certain spatial location ΔG may fully compensate applied echo-dephased gradients and positive signal (peak in the projection) may arise from spatially encoded off-resonant frequency.

The flip angle (α) was varied for every projection to compensate for the intrinsic signal loss from dephasing to achieve similar signal strengths for all locally rephased signals. Using a simple trigonometric relationship, optimal values were found to be around $\alpha 1 = 30^0$, $\alpha 2 = 35.5^0$, and $\alpha 3 = 45.5^0$.

4.2.3 Guidewire and Phantom

An MR-compatible guidewire made up of Polyetherethertone synthetic polymer core with a diameter of 0.7 mm and compatible with $0.035''$ catheter was used [16]. The paramagnetic material made up of stainless steel alloy was wrapped around the guidewire near its tip (Fig. 4.1a) with approximate dimensions 1mm in height and diameter. The guidewire core was covered along its axis with a polyurethane jacket. The hydrophilic adhesive coating was applied to hold the marker in place and to avoid its dislodgment or displacement during the experiments. Frequency measurements yield an LMD of $\Delta\chi V = 1 \times 10^{-11}\ m^3$ (in SI units). A local gradient field (ΔG) of approximately 15 mT/m was observed at around ± 5 mm away from the

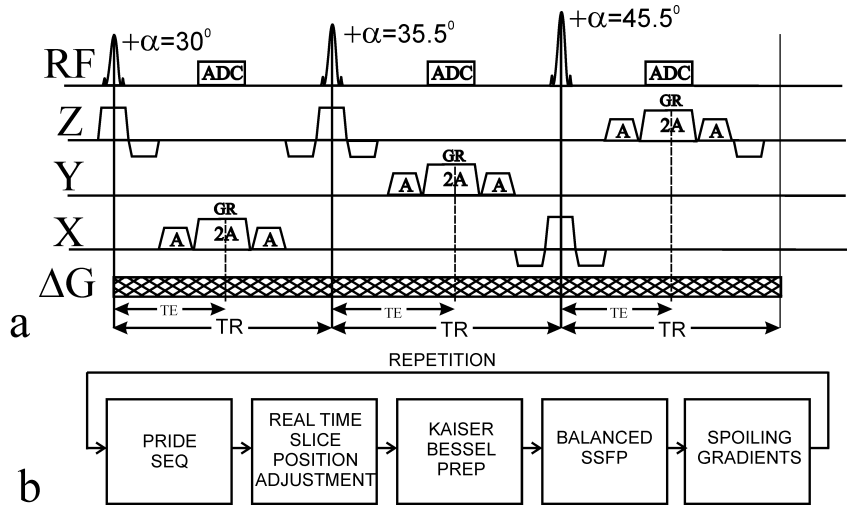

Figure 4.2: a) Schematic illustration of PRIDE. Echo-dephasing gradients are placed along three physical axes (X, Y and Z) of the magnet. The linear increase in the flip angle compensates for the intrinsic signal loss from dephasing in order to achieve similar signal strengths for all projections. Local gradient fields (ΔG, see Eq. 4.1) compete with echo-dephasing gradients (GR) to possibly form an echo. Sequence parameters used: FOV (along readout) 300 mm; base resolution 256; slice thickness 300 mm; TE/TR 3/6 ms; bandwidth/pixel=450 Hz. b) Block diagram of the automatic slice positioning system: PRIDE is followed by real time calculation of the slice position. An imaging sequence (bSSFP) is executed at the newly determined slice position after Kaiser Bessel preparation. Spoiling gradients are applied in the end to destroy any residual magnetization.

marker position along all three spatial directions using this LMD at 1.5 T (see Fig. 4.1b and Fig. 4.1c). The guidewire was inserted into a custom-built phantom with 11 mm diameter tubes to model the blood flow, positioning and tracking of the guidewire in large vessels. The tubes were immersed in a gadolinium (Gd)-doped water and were surrounded by a 2% agarose gel (v/v) doped with 0.5 mM copper sulphate ($CuSO_4$) concentration to closely resemble the relaxation times of muscle tissues for which T_1=900 ms and T_2=50 ms [21]. A 7F introducer sheath was attached to the tubes to facilitate the introduction and manipulation of the guidewire within the tubes.

4.2.4 PRIDE and Imaging Experiments

The performance of PRIDE for reliable detection of the paramagnetic marker position was first tested using the above-described flow phantom and guide wire. Projections with PRIDE were acquired at two different guidewire positions: one along the main magnetic field B_0 and the other at an acute angle (approximately 45^0) with respect to B_0. Sequence parameters used were: FOV (along readout) 300 mm; base resolution 256; slice thickness 300 mm; TE/TR 3/6 ms; flip angles=$30^0(X)$, $35.5^0(Y)$, $45.5^0(Z)$; bandwidth/pixel=450 Hz. Essentially, no phase encoding was employed. The sequence parameters were chosen heuristically.

For the subsequent bSSFP imaging, the following parameters were used: FOV 250×250 mm; matrix 128×128; slice Thickness 10 mm; TE/TR 2/4 ms; flip angle 40^0; bandwidth/pixel=500 Hz. No averages were performed.

In addition, the positional accuracy of the measured paramagnetic marker using PRIDE was verified, by placing the marker at various distances along the Z-direction from the iso-center of the magnet (with an increment of 10 mm). The absolute difference between the measured position using PRIDE and the actual position of the marker was assessed.

4.2.5 Automatic Slice Positioning

The capability of PRIDE for tracking guide wires for endovascular interventions was tested with ASP system fully operable on clinical scanners. In this work, bSSFP was used for imaging because of its suitability and wide applicability during endovascular interventions. A closed-loop block diagram of ASP is shown in Fig. 4.2b. PRIDE is followed by computation and adjustment of the slice position (explained in detail below). A Kaiser Bessel steady-state preparation [22] was followed by bSSFP imaging slice. Any remnant magnetization was spoiled at the end of the imaging block prior to PRIDE. The procedure is repeated to continuously monitor the guide wire tip.

Since PRIDE sequence is intrinsically slice selective in nature, special

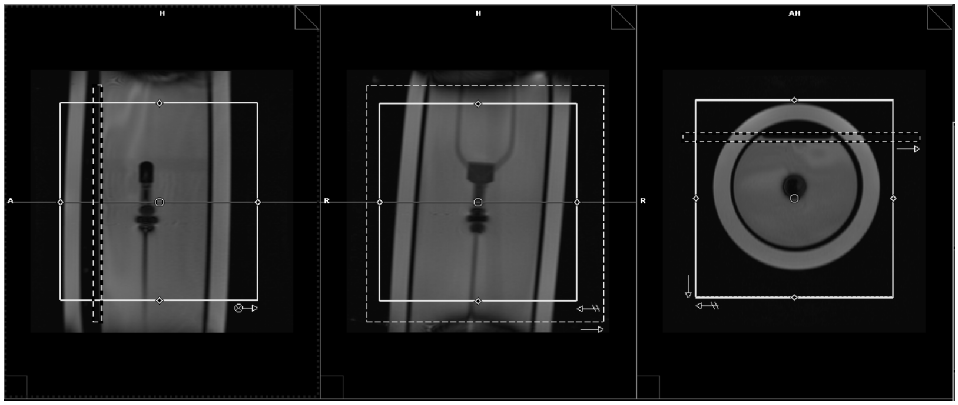

Figure 4.3: Automatic slice positioning using PRIDE includes a separate graphical slice positioning for marker detection (seen as white rectangular boxes). PRIDE related parameters can be interactively adjusted in a special dialogue card. The slice of the bSSFP sequence whose position needs to be adjusted is shown as dotted rectangular boxes.

graphical slice positioning (GSP) window was incorporated along with standard GSP used for bSSFP imaging slice. A special dialog card provides access to PRIDE related parameters (for example, TE, TR, FOV, resolution etc) independent of the imaging sequence. Fig. 4.3 shows a screenshot of the GSP system on the clinical scanner used. The rectangular white colored boxes show the GSP corresponding to PRIDE sequence, whereas dotted rectangular boxes show the normal imaging bSSFP sequence. PRIDE acquires three orthogonal projections to detect the paramagnetic marker position within the rectangular white colored boxes and the system adjusts the position of the slice shown as dotted rectangular boxes corresponding to marker position. The FOV and slice thickness for PRIDE was reduced from 300 to 200 mm.

4.2.6 Slice Position Calculation

A standard image reconstruction system (64-bit Linux system) running software framework, known as ICE (Image Calculation Environment, SIEMENS, Erlangen) in C++ was used to perform the slice position calculation. PRIDE acquires three orthogonal projections along all three spatial axes and projection data is sent to ICE. Upon reception of the projection data from PRIDE, calculation of 1D magnitude Fourier transforms was followed. Next, the absolute position of the maximum value of the 1D vector was stored. By knowing that the center of 1D vector corresponds to the imaging position of PRIDE, the absolute positions of the three maxima were converted into spatial shifts along three directions. These spatial shifts form 3D co-ordinates (imaging position) corresponding to marker position. Fast real-time feed-

back link facility (manufacturer provided) utilizing digital signal processors was used to send the calculated co-ordinates to the MPCU (Measurement and Physiological Unit), running pulse sequence. The acquisition of bSSFP imaging slice at this newly computed imaging position by MPCU and updating of the GSP is done automatically without any user intervention.

4.2.7 In Vivo Measurements

In vivo experiments were performed on a fully-anesthetized domestic pig weighing 35 kg. The experiments were conducted in accordance with all regulations set forth by their institutional and governmental agencies. The animal was placed head first in a supine position inside the scanner. A total of six elements of a phased-array spine RF coil were activated to provide signal of the posterior anatomy of the pig. A second six-element phased array RF body surface coil was placed anterior to the pig. The animal was heparinized with 5000 IU 2 h prior to the intervention and was subsequently anesthetized.

A 7 F introducer sheath was inserted into the right iliac artery via arterial cut down and the guidewire was inserted through the introduced sheath and guided through the vasculature utilizing cartesian and radial bSSFP sequences. PRIDE parameters were similar to phantom experiment except FOV (along readout) was reduced to 200 mm and constant flip angle of 50^0 was used.

4.3 Results

In this section, we first describe and elaborate upon the performance of PRIDE during the experiments conducted using flow phantom and guidewire as described in 'Materials and Methods' section. Since the localization of the guidewire tip play an important role during MR-guided interventions, the positional accuracy of the paramagnetic marker using PRIDE is described next. This is followed by flow phantom results of the ASP mechanism with PRIDE as the tracking sequence and bSSFP as the imaging sequence. Demonstration of the results of PRIDE in a swine model concludes the section.

4.3.1 In-Vitro Measurements

The experimental setup is shown in Fig. 4.4a. Two bSSFP images, one in coronal and the other in sagittal direction depict the experimental setup of the phantom as well as typical image artifacts from local susceptibilities due to the paramagnetic marker material mounted on the guidewire tip within the flow tubes. The conventional magnet axes directions (X, Y and Z) are shown on the image planes for better clearness. PRIDE projections along all

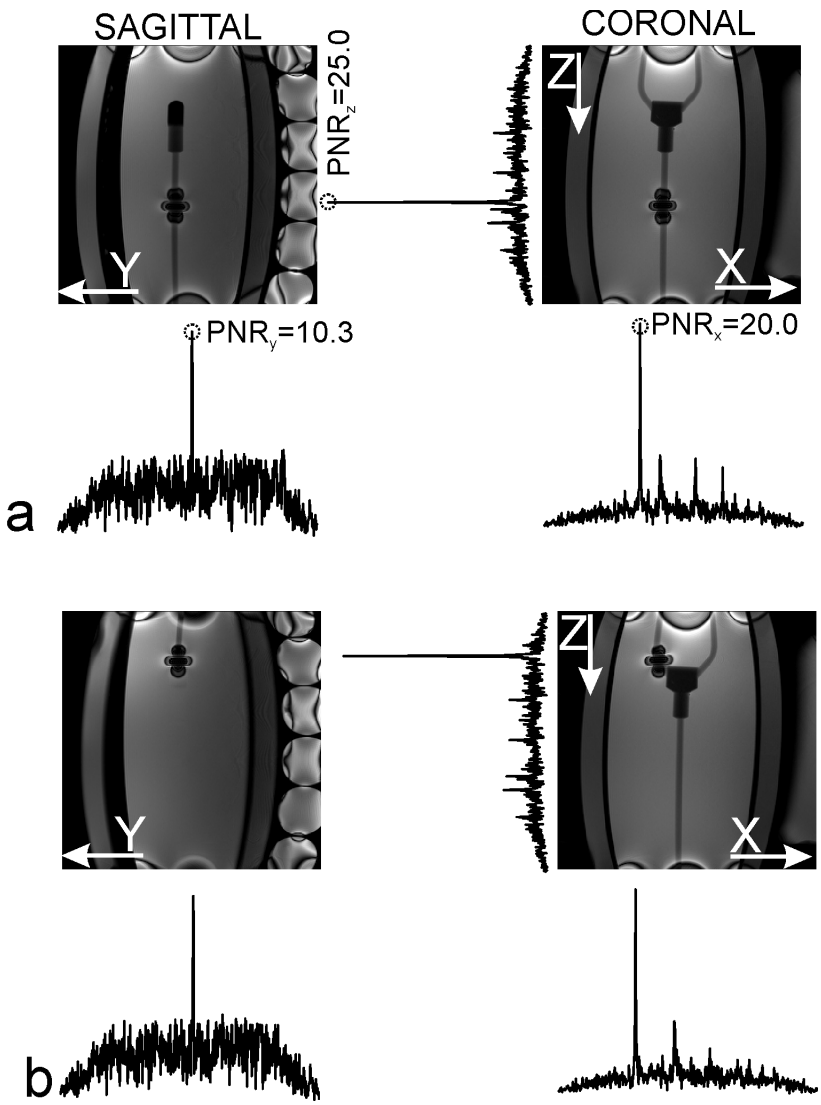

Figure 4.4: In vitro PRIDE results: a) Two bSSFP images, one in coronal and the other in sagittal direction, depict typical image artifacts due to the local susceptibility changes. PRIDE projections along all three (X, Y and Z) physical axes are shown in black. b) The tip of the guidewire was placed at an acute angle of approximately 45^0 with respect to the main magnetic field B_0. Corresponding projections are shown. Conventional magnet axes directions are shown in image planes. The detected peaks corresponding to marker position (encircled in dots) are clearly discernible. A minimum Peak-to-Noise Ratio (PNR) of approximately 10.3 was observed.

three physical axes are shown in black color in Fig. 4.4. Consistent with the theoretical predictions (see Fig. 4.2a), local gradient fields (ΔG) induced by the paramagnetic marker material compensated for the echo-dephasing gradients along the readout direction to form a local echo. All three projections show the discernible peaks (encircled in dots) lying well within the vicinity of the marker position whereas background tissues resembling blood, fat etc are reduced to the noise-level. The Peak-to-Noise (PNR) ratio (measuring peak signal level to mean background level along each direction) was calculated to be 20.0 (X), 10.3 (Y) and 25.0 (Z). The PNR along Y direction was lower as compared to X and Z direction, mainly due to stronger effects of off-resonance in Y direction for this particular phantom set-up. In spite of this, peak detection along all 3 directions using the PRIDE was excellent even in the presence of off resonance related degradations caused by other unwanted inhomogeneities. For the continuously moving guidewire, the PNR was found to exceed 10.0 along all directions (data not shown).

Fig. 4.4b again shows two bSSFP images, one in coronal and the other in sagittal direction, but with a paramagnetic marker positioned at an angle of approximately 45^0 with respect to the main magnetic field B_0 (corresponding to a positional shift of the marker along X and Z directions of the magnet). The projections (black in color) along X and Z clearly reveal peaks corresponding to the positional shift of the marker, whereas the peak in the Y projection remains almost unchanged. Thus, orientation of the marker material had a very limited impact on the position detection using PRIDE. This can be explained by the fact that the paramagnetic material is wrapped as a ring-like structure around the guidewire as has already been demonstrated in related work [14].

4.3.2 Localization Accuracy of PRIDE

Fig. 4.5 shows a plot of the absolute error difference between the actual paramagnetic marker position and its measured position using PRIDE along the Z-direction. Within the iso-center, the positional error was approximately $\pm$4-4.5 mm and reduced linearly with increasing distance from the iso-center. The systematic deviations due to gradient non-linearity are known to be approximately $\pm$5 mm at a distance of around 100 mm from the iso-center for the used gradient system. Thus, the error variation was related to the non-linearity of the gradient system [23]. As a result, with PRIDE, an absolute constant positional error of (4-4.5) mm was observed.

4.3.3 Automatic Slice Positioning

In order to provide the evidence that passive tracking using PRIDE performs better than image-based positive contrast methods and positional update of the slice corresponding to guidewire tip is feasible in real-time, results of the

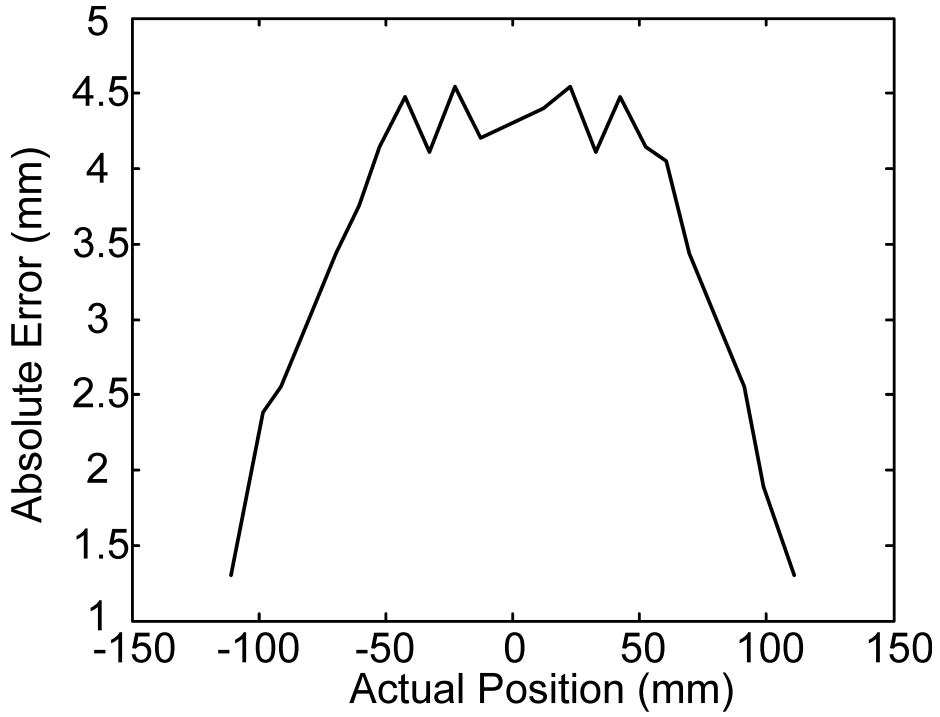

Figure 4.5: Absolute error difference between the actual paramagnetic marker position and its measured position using PRIDE along Z-direction. Around the iso-center of the magnet, positional error is approximately $\pm$4-4.5 mm and reduces linearly with increasing offsets. This is due to the non-linearity in the gradient system used. The systematic deviations due to gradient non-linearity are known to be approximately $\pm$5 mm at a distance of around 100 mm from the iso-center. Thus, using PRIDE, an absolute constant positional error of (4-4.5) mm is observed.

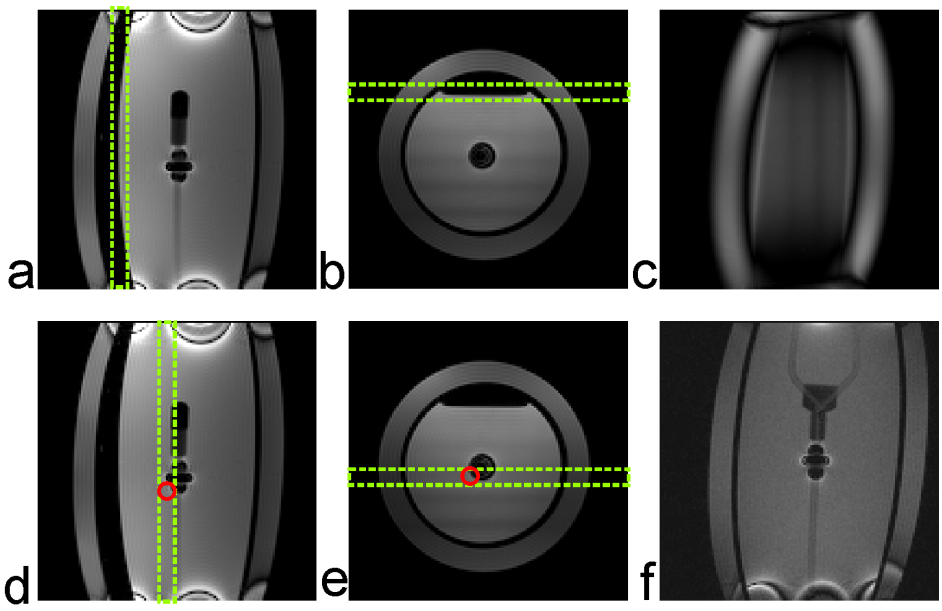

Figure 4.6: Demonstration of the automatic slice positioning mechanism: Localizer images in sagittal and transversal planes indicate slice positions before (a, b) and after (d, e) real-time feedback with corresponding coronal images acquired before (c) and after real-time feedback (f). Red circles indicate detected slice position. Slice positioning is slightly shifted from the marker's center-of-mass by a few millimeters, since local gradient compensation takes place outside of the marker position.

ASP mechanism are demonstrated using flow phantoms. Localizer images in sagittal and transversal planes indicate slice positions before (Fig. 4.6a, Fig. 4.6b) and after (Fig. 4.6d, Fig. 4.6e) real-time feedback with corresponding coronal images acquired before (Fig. 4.6c) and after real-time feedback (Fig. 4.6f). Red circles indicate the detected slice position, which is well within the proximity of the marker position. This clearly demonstrates that a positional update to the paramagnetic marker material was possible from simple projections, contrary to positive contrast techniques in which whole k-space data needs to be acquired. The total time needed to calculate the co-ordinates of the slice position and corresponding real-time feedback to MPCU was approximately 2-3 ms. Thus, the total time required to determine the slice position using PRIDE was approximately 20 ms (50 frames/s), comparable to active tracking systems (24 ms [23]) and significantly less than for positive contrast techniques.

4.3.4 In Vivo Validation

As described in 'Materials and Methods' section, the guidewire tip containing a paramagnetic material was placed in the infrarenal aorta of a pig. The final positioning of the marker can be seen in Real-time bSSFP coronal image shown in Fig. 4.7. The signal void due to susceptibility difference between the marker material and surrounding tissues is clearly seen (white arrow). Projections along X and Z directions using PRIDE are also shown in black color. Similar to the in-vitro experiments, both projections show discernible peaks (encircled as dotted areas) lying well within the vicinity of the marker indicating areas of local gradient compensation. In spite of other inhomogeneities (such as air-tissue interfaces etc.), optimal peak detection was observed along both directions. The PNR along X was found to be 3.1 and along Z to be around 8.9.

4.4 Discussion

The phantom results successfully demonstrate that fast detection and localization of passive paramagnetic marker (either stationary or moving) using PRIDE, employing echo-dephasing of 4π along three spatial axes (X, Y and Z), is feasible and may successfully be used for vascular interventional MRI applications.

Since local gradients and thus compensation of echo-dephasing from paramagnetic material is located in the close proximity of the marker, the detected peak position along every projection lies outside of the marker material. Thus, the positional accuracy achieved using PRIDE was also investigated. For vascular interventional MRI applications a small positional absolute error of (4-4.5) mm observed using PRIDE can be easily tolerated and if needed can be corrected for.

As mentioned previously, slice position is slightly shifted from the marker's center-of-mass by only a few millimeters. This shift may not pose a big problem for in-plane co-ordinates since a large FOV ensures the marker material being within the imaging plane. In order to guarantee that the marker is found within the imaging plane along the slice-select direction, one may either use a thick slab or a manual shift in the position. Thus, the observed offset between the marker material and the detected peak position may not hamper accurate guidewire tip tracking even under real-time conditions. Although the results shown here are obtained with a frame rate of approximately 2 frames/s, higher rates can be easily achieved by utilizing parallel imaging or other acceleration techniques without affecting the tracking performance of the PRIDE.

In most cases of ASP mechanism, PRIDE detected the marker position reliably for a motionless as well as moving guidewire. In few cases, PRIDE sometimes detected positions corresponding to other unwanted inho-

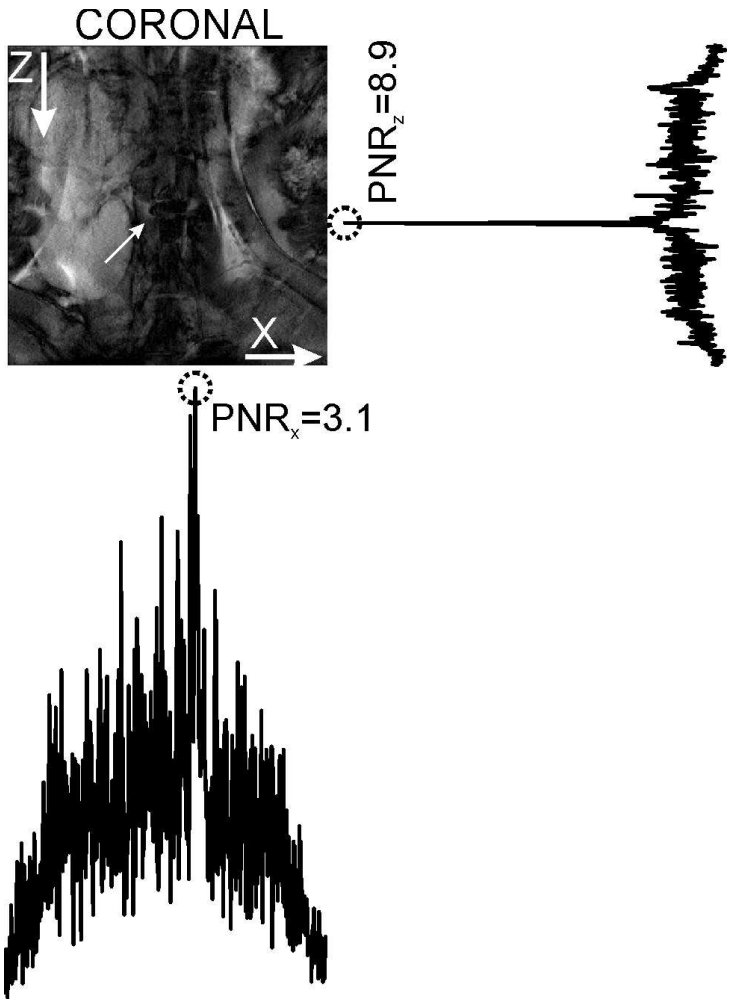

Figure 4.7: In vivo PRIDE results: Real-time bSSFP coronal image displaying the placement of the guidewire tip (small white arrow) identified by susceptibility artifact. The PRIDE projections along X and Z directions having peaks (encircled) within the close vicinity of the marker position are clearly seen.

mogeneities such as air-plastic boundary of the phantom since such boundaries create a gradually increasing gradient, which in turn gets compensated by echo-dephased gradients of PRIDE. The ASP mechanism using PRIDE interleaved with bSSFP for imaging was successfully demonstrated on a flow phantom, nevertheless its performance during the manipulation of guidewire along the tortuous vessels as well as under severe motion condition needs to be verified in-vivo.

Although the observed PNR is significantly lower during in vivo experiments as compared to phantom experiments, marker position can still be reliably detected due to excellent overall suppression of the background, especially for projections along the main magnetic field B_0. Along X, the PNR was lower as compared to the Z direction, most likely due to stronger field inhomogeneity effects. During MR-interventions, the main vessels (femoral artery, abdominal aorta) usually lie in the XZ plane; hence PRIDE may be successfully employed to track interventional devices.

The gradients induced by marker material strongly depend upon the LMD of the paramagnetic material (See Eq. 4.2) used. From Eq. 4.2, the LMD needed for compensation of imaging gradient and thus to form an echo is a complex function of field strength, gradient system and the distance from paramagnetic material. One may use a material with a strong susceptibility difference and/or bigger size to induce stronger gradients. By using stronger echo-dephased gradients in PRIDE, one can expect increased PNR. However, this would increase the artifact size and thereby hamper visualization of the underlying anatomical structures. Thus, from in vitro as well as in vivo experiments, it can be seen that the properties of the background (mainly gradients induced by unwanted inhomogeneities) play a role in defining the minimum size of the marker that can be detected.

Based on local gradient induction by paramagnetic marker material, PRIDE actively positions the slice at the device tip location. However, anatomy around the marker material is hindered due to signal loss in the imaged slice. Thus, some of the disadvantages of passive tracking remain when one uses PRIDE. Other unwanted inhomogeneities, such as air-tissue interfaces, may also compensate echo-dephasing in PRIDE giving rise to false peak detection. This may lead to acquisition of imaging slice at erroneous position. In order to reduce such false positives, intelligent post processing may be introduced such as that provided in [23] or by restricting peak detection within the close vicinity of the vessel anatomy (for example; from previously acquired angiograms). Recently, a similar tracking approach has been presented [24] that is based solely on an off-resonance tissue excitation and may lead to confounding results in the presence of fat tissues. Moreover, the artifact size within the image is approximately 10 cm in length as compared to 1.5-2 cm (in both lateral and vertical directions) in the current implementation.

In summary, we have demonstrated that PRIDE reliably detects the posi-

tion of paramagnetic marker materials wrapped around the MR-compatible guidewire along all three (X, Y and Z) spatial directions in vitro and along two (X and Z) vital spatial directions in vivo. PRIDE has been successfully incorporated into the ASP mechanism to feedback the actual position of the interventional device in real-time on a clinical scanner, thereby making it competitive with the active tracking approach.

4.5 Conclusion

We have presented a framework for passive real-time tracking of interventional guidewires using PRIDE. With PRIDE, 3D localization of the paramagnetic marker is achieved by the acquisition of echo-dephased projections along all three physical axes. Dephasing along each projection can be compensated, by local gradients induced by paramagnetic markers to give rise to peaks signal formation within the close vicinity of the marker. Background signals from tissues such as blood or fat, remain completely dephased. PRIDE shows excellent robustness against off-resonances (for e.g., main magnetic field inhomogeneities, air/tissue interfaces etc.) as evident from both in vitro as well as in vivo results. In addition, an ASP mechanism was developed by interleaving PRIDE with an imaging sequence to provide a positional update of the slice using a dedicated real-time feedback link. In vitro results suggest the feasibility of such a framework on a clinical scanner.

References

[1] C. Dumoulin, S. Souza, and R. Darrow, "Real-time position monitoring of invasive devices using magnetic resonance," *Magn Reson Med*, vol. 29, p. 411–5, Mar. 1993.

[2] O. Ocali and E. Atalar, "Intravascular magnetic resonance imaging using a loopless catheter antenna," *Magn Reson Med*, vol. 37, no. 1, p. 112–8, 1997.

[3] A. Glowinski, G. Adam, A. Bucker, J. Neuerburg, J. van Vaals, and R. Gunther, "Catheter visualization using locally induced, actively controlled field inhomogeneities," *Magn Reson Med*, vol. 38, p. 253–8, Aug. 1997.

[4] F. Wacker, D. Elgort, C. Hillenbrand, J. Duerk, and J. Lewin, "The catheter-driven MRI scanner: a new approach to intravascular catheter tracking and imaging-parameter adjustment for interventional MRI," *AJR Am J Roentgenol*, vol. 183, p. 391–5, Aug. 2004.

[5] M. Konings, L. Bartels, H. Smits, and C. Bakker, "Heating around intravascular guidewires by resonating RF waves," *J Magn Reson Imaging*, vol. 12, p. 79–85, July 2000.

[6] M. Ladd and H. Quick, "Reduction of resonant RF heating in intravascular catheters using coaxial chokes," *Magn Reson Med*, vol. 43, p. 615–9, Apr. 2000.

[7] T. Kuehne, S. Weiss, F. Brinkert, J. Weil, S. Yilmaz, B. Schmitt, P. Ewert, P. Lange, and M. Gutberlet, "Catheter visualization with resonant markers at MR imaging-guided deployment of endovascular stents in swine," *Radiology*, vol. 233, p. 774–80, Dec. 2004.

[8] S. Hegde, M. Miquel, R. Boubertakh, D. Gilderdale, V. Muthurangu, S. Keevil, I. Young, D. Hill, and R. Razavi, "Interactive MR imaging and tracking of catheters with multiple tuned fiducial markers," *J Vasc Interv Radiol*, vol. 17, p. 1175–9, July 2006.

[9] M. Burl, G. Coutts, and I. Young, "Tuned fiducial markers to identify body locations with minimal perturbation of tissue magnetization," *Magn Reson Med*, vol. 36, p. 491–3, Sept. 1996.

[10] D. Rubin, A. Ratner, and S. Young, "Magnetic susceptibility effects and their application in the development of new ferromagnetic catheters for magnetic resonance imaging," *Invest Radiol*, vol. 25, p. 1325–32, Dec. 1990.

[11] O. Unal, F. Korosec, R. Frayne, C. Strother, and C. Mistretta, "A rapid 2D time-resolved variable-rate k-space sampling MR technique for passive catheter tracking during endovascular procedures," *Magn Reson Med*, vol. 40, p. 356–62, Sept. 1998.

[12] O. Bieri, S. Patil, H. Quick, and K. Scheffler, "Morphing steady-state free precession," *Magn Reson Med*, vol. 58, p. 1242–8, Dec. 2007.

[13] V. Kochli, G. McKinnon, E. Hofmann, and G. von Schulthess, "Vascular interventions guided by ultrafast MR imaging: evaluation of different materials," *Magn Reson Med*, vol. 31, p. 309–14, Mar. 1994.

[14] C. Bakker, R. Hoogeveen, J. Weber, J. van Vaals, M. Viergever, and W. Mali, "Visualization of dedicated catheters using fast scanning techniques with potential for MR-guided vascular interventions," *Magn Reson Med*, vol. 36, p. 816–20, Dec. 1996.

[15] J. Seppenwoolde, M. Viergever, and C. Bakker, "Passive tracking exploiting local signal conservation: the white marker phenomenon," *Magn Reson Med*, vol. 50, p. 784–90, Oct. 2003.

[16] R. Mekle, E. Hofmann, K. Scheffler, and D. Bilecen, "A polymer-based MR-compatible guidewire: a study to explore new prospects for interventional peripheral magnetic resonance angiography (ipMRA)," *J Magn Reson Imaging*, vol. 23, p. 145–55, Feb. 2006.

[17] J. Seppenwoolde, L. Bartels, R. van der Weide, J. Nijsen, A. van het Schip, and C. Bakker, "Fully MR-guided hepatic artery catheterization for selective drug delivery: a feasibility study in pigs," *J Magn Reson Imaging*, vol. 23, p. 123–9, Feb. 2006.

[18] R. Razavi, D. Hill, S. Keevil, M. Miquel, V. Muthurangu, S. Hegde, K. Rhode, M. Barnett, J. van Vaals, D. Hawkes, and E. Baker, "Cardiac catheterisation guided by MRI in children and adults with congenital heart disease," *Lancet*, vol. 362, p. 1877–82, Dec. 2003.

[19] M. Miquel, S. Hegde, V. Muthurangu, B. Corcoran, S. Keevil, D. Hill, and R. Razavi, "Visualization and tracking of an inflatable balloon catheter using SSFP in a flow phantom and in the heart and great vessels of patients," *Magn Reson Med*, vol. 51, p. 988–95, May 2004.

[20] "ESMRMB 2008 congress, valencia, spain, 2-4 october: EPOSGao posters / Info-RESO," *Magma*, vol. 21 Suppl 1, p. 235–489: p. 395, Sept. 2008.

[21] B. H. EM, *Magnetic resonance imaging: physical principles and sequence design*. New York: Wiley, 1999.

[22] P. L. Roux, "Simplified model and stabilization of SSFP sequences," *J Magn Reson*, vol. 163, p. 23–37, July 2003.

[23] M. Bock, S. Volz, S. Zuhlsdorff, R. Umathum, C. Fink, P. Hallscheidt, and W. Semmler, "MR-guided intravascular procedures: real-time parameter control and automated slice positioning with active tracking coils," *J Magn Reson Imaging*, vol. 19, p. 580–9, May 2004.

[24] A. Chanu, O. Felfoul, G. Beaudoin, and S. Martel, "Adapting the clinical MRI software environment for real-time navigation of an endovascular untethered ferromagnetic bead for future endovascular interventions," *Magn Reson Med*, vol. 59, p. 1287–97, June 2008.

Chapter 5

Highly Miniaturized Micro coils To Track Interventional Devices

The work undertaken here is a part of EU project named Micro MR. This chapter has been partially presented as:

- **S. Patil**, R. Umathum, M. Bock, J. Anders, G. Boero, K. Scheffler, "Highly miniaturized micro coil for tracking of the interventional devices", Proceedings of the 17th Scientific meeting of ISMRM, Hawaii, pp. 2009.
- **S. Patil**, R. Umathum, M. Bock, J. Anders, G. Boero, K. Scheffler, "Highly miniaturised micro coil for tracking of the interventional devices", Proceedings of the 7th Interventional MRI Symposium (Oral Presentation), 2008.

5.1 Overview

Over the recent years, MRI has developed from a purely diagnostic tool to an imaging modality that can also be used to monitor endovascular interventions. For such interventions, a reliable and high-contrast visualization of the interventional devices (for e.g. catheter) in relation to surrounding anatomy by means of active tracking coils is a well-established method since its introduction [1]. The active tracking utilizes locally sensitive transmit/receive solenoid coils for device localization [2, 3]. Localization of the coil is achieved in few milliseconds through acquisition of one dimensional (1D) projections along all three spatial directions (X, Y and Z). Thus, very high frame rates of 50 frames/s can be easily achieved. The positional information is then used to actively align the position of the imaging slice [4, 5]. In addition, velocity of the device has been used to automatically adjust the imaging parameters [6]. Although this method suffers from RF heating issues [7], efforts are being undertaken to mitigate them, see for e.g. [8, 9].

However, the dimensions of state-of-the-art active coils are bulky in nature (typically 2-3 mm in diameter) thereby increasing the size of normal interventional catheters. In addition, the sensitivity of the coil and hence, the spatial resolution is directly proportional to coil dimensions [10]. As compared to x-ray fluoroscopy that offers a device localization resolution in the range of the order of 0.1 mm, the current device dimensions limit the resolution in MRI. In order to overcome these disadvantages, highly miniaturised planar micro coils with built-in amplifier are developed [11]. Typical dimensions of these micro-coils are $0.5 \times 0.5\ mm^2$ including the built-in amplifier. The aim of this chapter is to demonstrate the feasibility of these miniaturized micro-coils to utilize them as the tracking coil on a clinical scanner with an aid of phantom experiments. In the first part of this chapter, we describe the experimental arrangements, difficulties thereof and MR sequence parameters. Next, the description and discussion of results obtained by means of spectroscopic, imaging and 1D projection are presented. Perspectives from the results conclude the chapter.

5.2 Experimental Setup

The coils which have been developed by are designed to operate at 63 MHz corresponding to 1.5 T magnetic field strength. The equivalent circuit of the micro coil setup including connection to the clinical scanner through Flex coil interface is shown in Fig. 5.1. The planar micro coil L tuned to 63 MHz frequency using capacitor C, is connected to a low noise amplifier (LNA) with a gain of 43 dB. The development of micro-coil with built-in pre-amplifier was done using 0.35 μm CMOS technology. The photograph

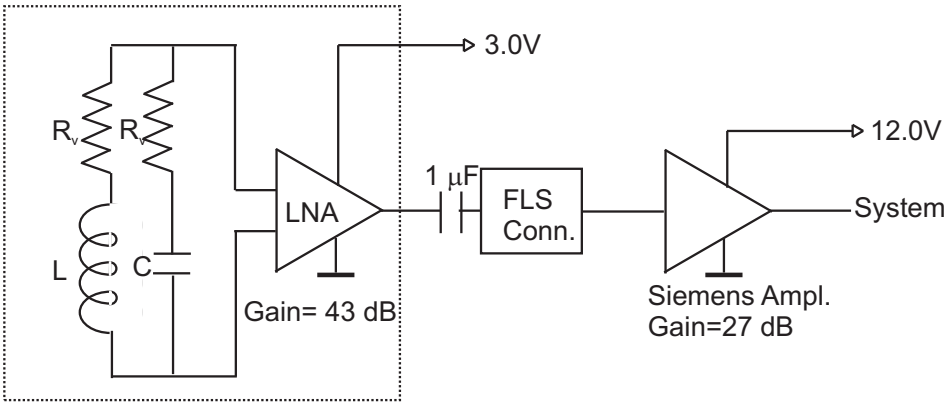

Figure 5.1: Equivalent circuit diagram of the microcoil including connection to clinical scanner through flex coil small interface. Partially Adapted from Anders et.al [11]

of the enlarged planar coil circuitry (dotted area in Fig. 5.1) is shown in Fig. 5.2. The development of the micro-coil was done under the EU grant named MicroMR by Jens Anders and Giovanni Boero at EPFL Lausanne.

The coil was placed in a magnet bore with its plane parallel to the main magnetic field (B_0). This arrangement ensured that B_0 field, applied transmit field (B_1) and plane of the micro-coil were mutually perpendicular to each other. A weakly magnetic battery (3.6 V) was used as a power supply to LNA.

5.2.1 Probe sample

To measure the performance of such a miniaturized micro-coil requires suitbale MR sample. Since the ultimate use of these coils is to use them as a tracking device, water sample would be a best choice. However, placement of liquid sample on such a small coil was difficult. Hence one can use solid samples, for example; rubber material. Solid sample poses additional problem of short T_2 thereby making measrements difficult [10]. In order to overcome these disadvantages, a glycerol nitrate capsule (T_1=135 ms; T_2=90 ms; 5 mm in diameter) was used as a sample for MR measurements and was placed directly above the coil. This capsule contains liquid having suitable relaxation paramaters and was easy to handle. The photograph of the connection setup is been shown in Fig. 5.3. The white arrow indicates the micro-coil position. The glycerol nitrate capsule (red ball) can be clearly seen. Connection to the non-magnetic battery is also seen.

During the initial stages, the coil was connected to Flex coil small interface using long coaxial cable (> 1 m). This long cable lead to have a loading effect on the micro-coil output. This in turn lead to damage of the many micro-coils before realising the problem. Eventually the coaxial cable

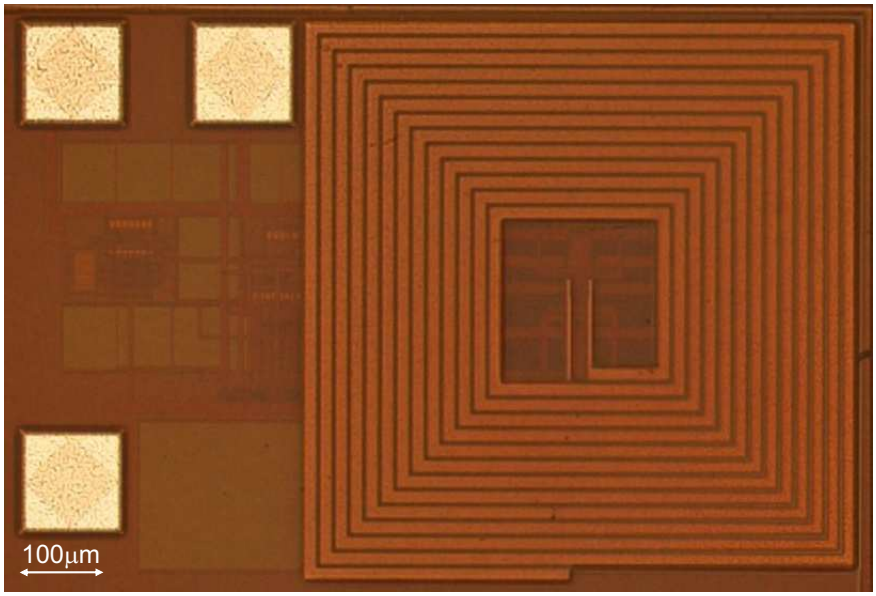

Figure 5.2: The enlarged photograph of the planar coil with built-in preamplfier circuitry (dotted area in Fig. 5.1) Adapted from Anders et.al [11]

length was reduced to around 5-10 cm in length (seen as brown in color in Fig. 5.3) thereby removing the risk of damaging the coil due to loading effect. In addition, bonding connections connecting micro-coil input, output and power supply to the outside world were delicate and were breaking off easily during its handling. To overcome this, bondings were fixated with epoxy material.

5.2.2 Acquisition Details

All the measurements were done on a Siemens Espree 1.5T scanner. The flip angle and frequency adjustments were made using the body coil. Spectroscopic experiments were carried out using following parameters: a hard pulse of duration 0.24 ms, flip angle 90^0 (Amplitude 175 V), TE 0.22 ms, TR 1 s, bandwidth 10 kHz, acquisition duration 204 ms and averages 1. For imaging purpose, transversal 3D FLASH sequence was used with flip angle 15^0, TE/TR 6.6/17.2 ms, Bandwidth/pixel 90 Hz, FOV 20×27 mm^2, Matrix 256×192, slice thickness 0.11 mm, number of slices 128 giving a resolution of 0.1×0.1×0.1 mm^3.

To further verify the susceptibility influence of the on-board components, High resolution images FLASH images (0.31 mm × 0.31 mm; TE/TR 5.12/ 250 ms; Averages 16; flip angle 60^0; slice thickness 8 mm) of two glycerol nitrate capsules; one placed directly over the micro-coil and the other one placed further away from the micro-coil. In addition, PCB board containing

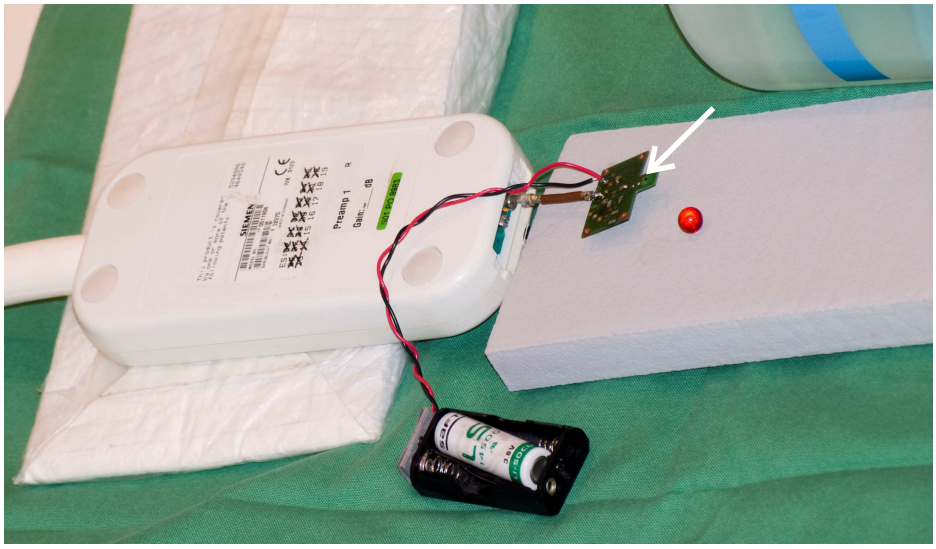

Figure 5.3: Photograph of the connection of the microcoil including connection to clinical scanner through flex coil small interface. The white arrow indicates the position of the micro-coil. The glycerol nitrate capsule (red ball) can be clearly seen.

micro-coil was placed in a water bath and imaging experiments were done using balanced SSFP sequence (0.5 mm $\times$ 0.5 mm; TE/TR 3.19/6.37 ms; flip angle 70^0; slice thickness 3.5 mm). The imaging was done using intergrated spine coils.

Since the sensitivity of the micro-coils is confined to small region, projections obtained should show a peak corresponding to its position. In order to avoid off-resonance effects due to field inhomogeneities, hadamard-encoded four projections are acquired [2]. Hence, in order to demonstrate the tracking performance of the coil, the projections were obtained along X, Y and Z directions with coil acting as a receiver. The acquisition parameters were: a hard pulse (duration 0.5 ms); data points 256; FOV 300 mm; TE/TR 1.55/5.0 ms. In addition, in order to measure the non-linearity of the gradient system the projections were also obtained at different Z positions with an increment of 10 mm.

5.3 Results and Discussions

In this section, we first present the results obtained using basic spectroscopic experiments. The susceptibility influence of the on-board components is described next. Imaging experiments to depict the area of coil sensitivity are followed. Finally to demonstrate that the coil can possibly be used to track interventional device, projection results are described.

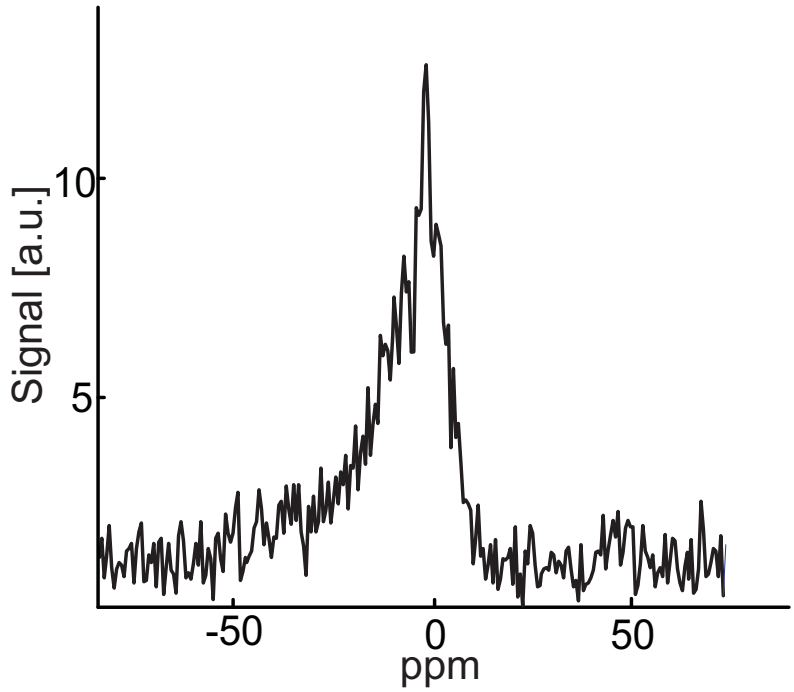

Figure 5.4: The FID spectrum of the MR sample depicting a peak corresponding to its resonance

5.3.1 Spectrum Measurement

Figure 5.4 shows the spectrum obtained after Fourier transformation of the free induction decay (FID) of the glycerol nitrate capsule. The frequency domain SNR of approximately 8.55 was observed. The broadening of the spectrum is clearly visible. The full-width half maximum (FWHM) of 140 Hz was measured corresponding to T_2^* value of 2.3 ms. These values indicated there was an influence of susceptibility effect of the on-board components due to broadening of the spectrum.

5.3.2 Susceptibility Influence

The high-resolution FLASH image depicting two glycerol nitrate capsules are depicted in Fig. 5.5a. The signal from the capsule placed away from the micro-coil can be seen as high contrast circular region, whereas the signal from the capsule placed over the micro-coil (see white arrow) shows black stripes indicating the influence of susceptibility of the surrounding materials. The balanced SSFP image of the PCB board placed in a water bath is shown in Fig 5.5b. The dipole-shaped susceptibility artifacts (black voids) are seen within the close vicinity of the coil, further corroborating the influence of susceptibility artifacts of the on-board components. In general,

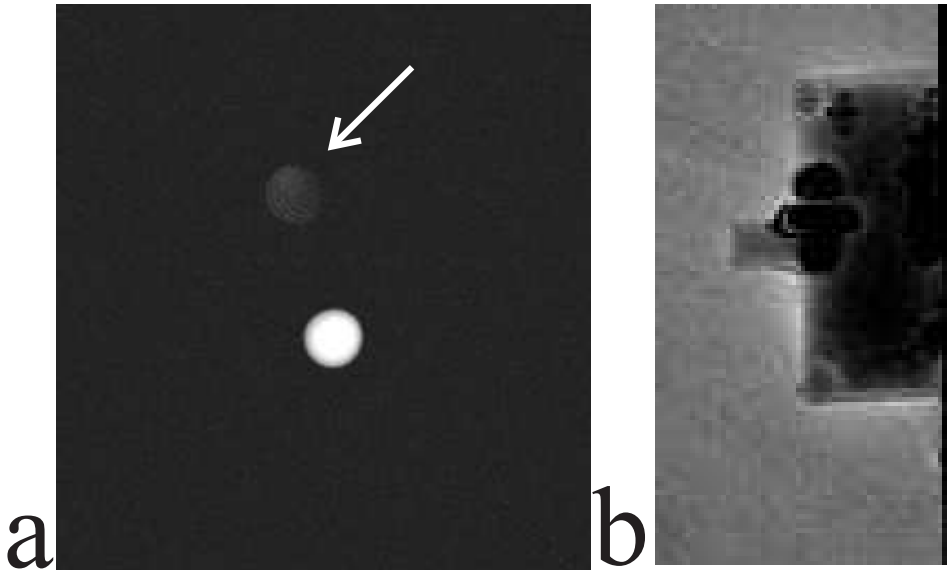

Figure 5.5: The susceptibility influence of the on-board components. a) high-resolution FLASH image depicting two glycerol nitrate capsules. The signal from the capsule placed away from the micro-coil can be seen as high contrast circular region, whereas the signal from the capsule placed over the micro-coil (see white arrow) shows black stripes indicating the influence of susceptibility of the surrounding materials b) balanced SSFP image of the PCB board placed in a water bath. Dipole-shaped susceptibility artifacts (black voids) are seen within the close vicinity of the coil.

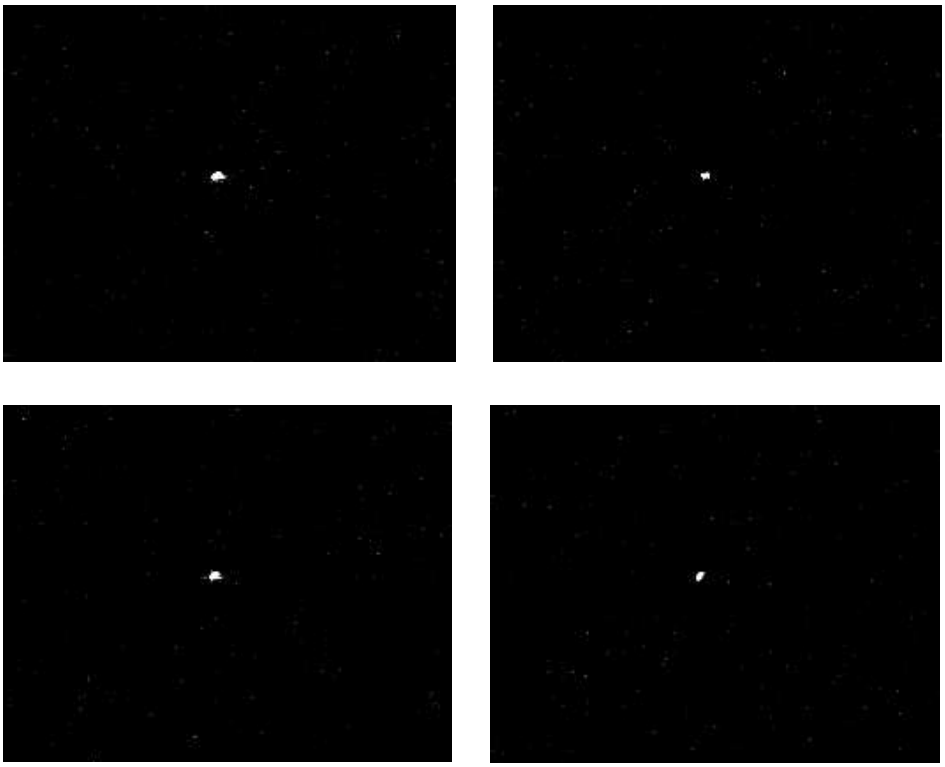

Figure 5.6: Selective consecutive images obtained using micro-coil using glycerol nitrate capsule as a MR sample. The approximate SNR of 44 was observed.

field inhomogeneities lowers the frequency domain SNR of the coil and hence care needs to be taken to avoid suceptibility influences.

5.3.3 Imaging

To access the sensitivity profile of the coil and depiction of the same using imaging exeperiments are presented. Figure 5.6 shows selective four consecutive images depicting bright spot indicating the signal obtained using micro-coil as a receptor. The measured SNR of about 44 was observed. The bright spot region is extended well over 4-5 pixels along all three directions approximately corresponding to coil dimensions. These results indicate that sensitivity profile of the coil corresponds well with its dimensions. It may also be perceived that current miniaturized micro-coil with built-in amplfier can be utilized as micro-imaging tool on a clinical scanner.

5.3.4 Peak Detection

Figure 5.7a, b and c shows the projections obtained along X, Y and Z directions respectively. The peak depiction corresponding to the coil position can be clearly visualised and delineated from the noise signal. The SNR of about 10 was obtained for every projection. Due to limited sensitivity of the highly miniaturized micro-coil, the signal detected is only non-vanishing at its position.

Fig 5.7d shows the graph of the difference $(Z_m - Z_a)$ between actual position and measured position using projection technique against the actual Z-positions (Z_a). It can be seen that the difference $(Z_m - Z_a)$ increases linearly with the increasing distance from the iso-centre, which is consistent with the non-linearity of the gradient system, hence proving the utility of the coil as a RF receiver.

Finally, from the results presented in this chapter, it can be deduced that current miniaturized micro-coil may be utilized as an active tracking coil for interventional purpose by suitably placing it over the device. However, further modifications of the micro-coil are necessary to avoid for e.g. the susceptibility influence of the on-board components. Further experiments should be carried out using flow phantoms to further access the sensitivity profile and detection capability of the coil. Generally well-known heating issues associated with long cables connecting RF coils need to be accessed as well. As described in 'Experimental Section', coaxial cable connecting the micro-coil output to the Flex loop small interface was shortened to avoid the loading effect. However, from the interventional application point of view a work around need to be found out.

5.4 Conclusion

The main aim of this chapter was to introduce and test highly miniaturized micro-coils on a clinical scanner. The results presented in this chapter indicate that the micro coil with typical dimensions of 0.5 mm $\times$ 0.5 mm and built-in amplifier can be used as a RF detector on clinical scanner. The spectroscopic and imaging showed the SNR and sensitivity of the coil. High resolution FLASH and bSSFP imaging experiments indicated heavy influence of susceptibility effect of on-board components. A care need to be taken to strictly use non-ferromagnetic componentns. The SNR of the projections appears moderately sufficient to detect the position of the micro-coil for the sample used in the experiment. Further modifications and experiments are necessary to incorporate the micro coil into an interventional device.

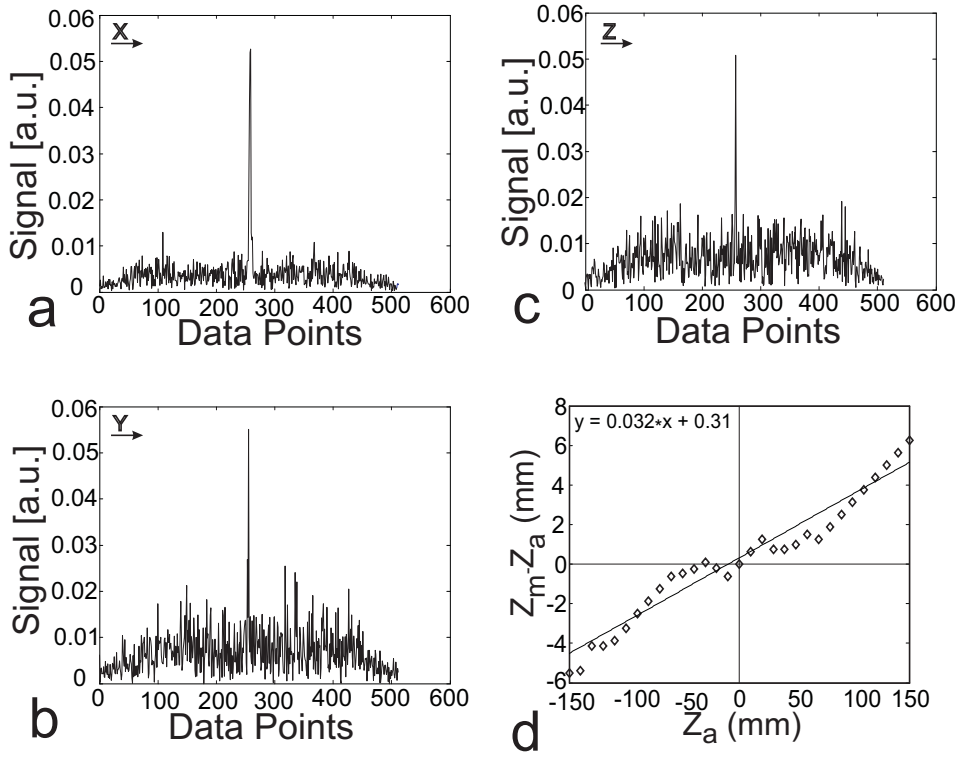

Figure 5.7: Projections obtained using micro-coil as a receiver coil along a) X b) Y c)Z directions. d) Plot of the difference $(Z_m - Z_a)$ between measured and actual coil position as a position along Z-direction

References

[1] J. L. Ackerman, M. C. Offut, R. B. Buxton, and T. J. Brady, "Rapid 3D tracking of small RF coils.," in *Proceedings of the SMRM*, (Montreal), p. 1131, 1986.

[2] C. Dumoulin, S. Souza, and R. Darrow, "Real-time position monitoring of invasive devices using magnetic resonance," *Magn Reson Med*, vol. 29, p. 411–5, Mar. 1993.

[3] O. Ocali and E. Atalar, "Intravascular magnetic resonance imaging using a loopless catheter antenna," *Magn Reson Med*, vol. 37, no. 1, p. 112–8, 1997.

[4] M. Bock, S. Volz, S. Zuhlsdorff, R. Umathum, C. Fink, P. Hallscheidt, and W. Semmler, "MR-guided intravascular procedures: real-time parameter control and automated slice positioning with active tracking coils," *J Magn Reson Imaging*, vol. 19, p. 580–9, May 2004.

[5] M. E. Ladd, G. G. Zimmermann, H. H. Quick, J. F. Debatin, P. Boesiger, G. K. von Schulthess, and G. C. McKinnon, "Active MR visualization of a vascular guidewire in vivo," *Journal of Magnetic Resonance Imaging: JMRI*, vol. 8, pp. 220–225, Feb. 1998. PMID: 9500284.

[6] F. Wacker, D. Elgort, C. Hillenbrand, J. Duerk, and J. Lewin, "The catheter-driven MRI scanner: a new approach to intravascular catheter tracking and imaging-parameter adjustment for interventional MRI," *AJR Am J Roentgenol*, vol. 183, p. 391–5, Aug. 2004.

[7] M. Konings, L. Bartels, H. Smits, and C. Bakker, "Heating around intravascular guidewires by resonating RF waves," *J Magn Reson Imaging*, vol. 12, p. 79–85, July 2000.

[8] M. Ladd and H. Quick, "Reduction of resonant RF heating in intravascular catheters using coaxial chokes," *Magn Reson Med*, vol. 43, p. 615–9, Apr. 2000.

[9] S. Weiss, P. Vernickel, T. Schaeffter, V. Schulz, and B. Gleich, "Transmission line for improved RF safety of interventional devices," *Magnetic Resonance in Medicine: Official Journal of the Society of Magnetic Resonance in Medicine / Society of Magnetic Resonance in Medicine*, vol. 54, pp. 182–189, July 2005. PMID: 15968655.

[10] C. Massin, F. Vincent, A. Homsy, K. Ehrmann, G. Boero, P. Besse, A. Daridon, E. Verpoorte, N. F. de Rooij, and R. S. Popovic, "Planar microcoil-based microfluidic NMR probes," *Journal of Magnetic Resonance (San Diego, Calif.: 1997)*, vol. 164, pp. 242–255, Oct. 2003. PMID: 14511593.

[11] J. Anders, S. Reymond, G. Boero, and K. Scheffler, "A Low-Noise CMOS receiver frontend for NMR-based surgical guidance," in *Proceedings of the International Conference on Biomedical Engineering*, (Singapore), IEEE, 2008.

Chapter 6

Summary And Future Outlook

The major aim of this thesis was to investigate and develop novel strategies to perform localization, visualization and tracking of the interventional devices exploiting magnetic susceptibility artifacts induced by paramagnetic marker material mounted on it. This thesis also introduced highly miniaturized micro-coils to be used for active tracking of the interventional devices. In this final chapter, we summarize the key contributions of this thesis and provide some possible future outlook.

The key contributions of this thesis are:

- In the first part of this thesis, SPSP pulses has been utilized as a way to localize and visualize paramagnetic markers with a positive contrast. It was utilized to visualize interventional guidewire tip. The SPSP pulse, which is both spatially as well as spectrally selective, was used to excite off-resonant tissues within the immediate surrounding of the paramagnetic marker to generate positive contrast. By additionally playing out STIR pre-pulse efficient fat suppression was achieved, whilst retaining the positive contrast. The proximity of the positive contrast to the marker tip was dependent on off-resonance excitation frequency of the SPSP pulse, whereas volume of the positive contrast was dependent on the number of RF sub-pulses within the SPSP pulse.

- Next, a novel concept for the generation of positive contrast from local susceptibilities, termed echo-dephased SSFP was proposed. In principle, echo-dephased SSFP is an unbalanced SSFP type of sequence, in which echoes are dephased prior to readout. We have demonstrated that this echo-dephasing approach ensures excellent cancellation of any background signals. From local gradient compensation hyper-intense signals are formed and thus a positive contrast emanates within the close vicinity of paramagnetic marker materials. Hyper-intense signals are mainly of bSSFP type, which ensures sufficient signal intensity with respect to background. A reliable localization and robust marker detection was demonstrated using the proposed method. The passive guidewire tracking experiments were performed in flow phantoms suggesting suitable applicability of the echo-dephased SSFP for MR-guided interventions such as ipMRA. Finally utilization of echo-dephased SSFP for positive contrast visualization of SPIO-labeled islet cells was demonstrated both in vitro and in vivo.

- A new framework was also presented for passive real-time tracking of interventional guidewires using PRIDE. With PRIDE, 3D localization of the paramagnetic marker is achieved by the acquisition of echo-dephased projections along all three physical axes. Dephasing along each projection can be compensated, by local gradients induced by paramagnetic markers to give rise to peaks signal formation within the close vicinity of the marker. Background signals from tissues such

as blood or fat, remain completely dephased. PRIDE shows excellent robustness against off-resonances (for e.g., main magnetic field inhomogeneities, air/tissue interfaces etc.) as evident from both in vitro as well as in vivo results. In addition, an ASP mechanism was developed by interleaving PRIDE with an imaging sequence to provide a positional update of the slice using a dedicated real-time feedback link. In vitro results suggest the feasibility of such a framework on a clinical scanner.

- Finally, highly miniaturized micro-coils were introduced for active tracking of the interventional devices. The results presented indicate that the micro coil with typical dimensions of 0.5 mm $\times$ 0.5 mm and built-in amplifier can be used as a RF detector on clinical scanner. The SNR of the projections appears moderately sufficient to detect the position of the micro-coil for the sample used in the experiment. It was concluded that, further modifications and experiments are necessary to incorporate the micro coil into an interventional device.

6.1 Future Outlook

Research in the field of MR device tracking is vigorously active and still requires major development before calling it as a clinical reality. The current general research direction in the field of vascular interventions indicate that guidewire tracking may be realized using passive tracking means, whereas active tracking may be suitbale for catheter tracking. Ultimately, the sequences and device interfaces developed in this thesis should be helpful for robust detection of paramagnetic marker detection and find its utility in passive tracking of interventional devices, especially guidewires. Before making them clinically useful, further investigation is necessary. This section summarizes some possible future directions for the work described in this thesis as well as general device development.

- To further verify the efficacy of the marker detection using both positive contrast sequences; SPSP pulse and echo-dephased SSFP, in-vivo studies in a pig model should be very helpful.

- In this thesis, the performance of the passive tracking methods was presented for fixed size paramagnetic marker. However, in the anticipation of availability of the certified guidewires with possibly having different paramagnetic materials, methods presented in this thesis need to be reaccessed for the new guidewires.

- One of the major requirement of positive contrast sequences is to acquire full 2D image, which obviously limits its utilization to track interventional devices. Further studies exploring the incorporation of

fast imaging strategies such as view sharing, fast image reconstruction methods should be very helpful.

- Effect of detection ability using positive contrast sequences at different device speeds, within tortuous and narrow vessels in a pig model would further be needed.
- Another obvious and interesting application of positive contrast sequences is the localization, tracking and quantification of SPIO-labeled cells. Although preliminary studies showed its potential, further in-vitro and in-vivo studies could potentially be done to explore its clinical viability.
- Quantification of SPIO-labeled cells is a challenging problem and studies using positive contrast sequences may further prove its clinical utility.
- Preliminary studies using PRIDE in a pig model demonstrated its efficient marker detection ability. However, further experiments of ASP mechanism are necessary to corroborate the results presented in this thesis.
- One may also adopt a strategy to use the interventional device with three different paramagnetic markers, their detection using PRIDE and use them to adjust not only slice position but also the plane of the following slice.
- Highly miniaturized micro-coils introduced in this thesis may have a potential to be used for catheter tracking. Further studies could include incorporation of the micro-coils onto a prototype catheter, in-vitro and in-vivo studies using the same.
- To further access the SNR and sensitivity profile of the coil, in vitro experiments need to be done using more realistic conditions of vascular interventions such as flow phantom. Enlargement of coil dimensions would be needed if SNR of the coil is found to be insufficient.
- Requirement of small coaxial cable to connect the micro-coil to the scanner may be overcome by incorporating highly miniaturized demodulation system, demodulating high frequency (removal of carrier frequency) signal to the low frequency. Such a low frequency output may also potentially to induce less heating than RF frequency.
- It would be also important to study safety aspects these micro-coils. Instead of using connecting cables one may explore the utility of wireless systems to transfer the MR signal from device tip to the outside world.